UNIVERSITEIT ANTWERPEN
Faculteit Wetenschappen
Departement Fysica

Electronic structure of core-shell nanowires

Elektronische structuur van kern-schil nanodraden

Proefschrift voorgelegd tot het behalen van de graad van doctor in de wetenschappen aan de Universiteit Antwerpen te verdedigen door

V. V. Ravi Kishore

Promotoren
Prof. Dr. F. M. Peeters
Prof. Dr. B. Partoens

Antwerpen
January, 2013

Members of the Jury:

Chairman
Prof. Nick Schryvers, Universiteit Antwerpen, Belgium

Supervisors
Prof. Francois Peeters, Universiteit Antwerpen, Belgium
Prof. Bart Partoens, Universiteit Antwerpen, Belgium

Members
Prof. Wim Magnus, Universiteit Antwerpen, Belgium
Prof. Bart Sorée, IMEC Leuven, Belgium
Prof. Wim Wenseleers, Universiteit Antwerpen, Belgium
Prof. Milan Tadić, University of Belgrade, Serbia

Contact Information

V. V. Ravi Kishore
CGB U. 206
Department Fysica
Universiteit Antwerpen
Groenenborgerlaan 171
2020 Antwerpen
Belgium
ravi.vepakomma@ua.ac.be

Acknowledgements

Working through my PhD has been a wonderful learning experience and it gives me immense pleasure to express my heartfelt gratitude towards all the people who have made this journey possible.

Firstly, I am deeply grateful to Prof. Francois Peeters for giving me an opportunity to work in his prestigious research group. He has been a steady influence throughout my PhD career. His patience, valuable suggestions and prompt comments with high scientific standards has been a great help. I have always admired his organization skills and the ability to pay attention to every student despite each of them working on different topics.

Secondly, I am extremely grateful to Prof. Bart Partoens who has been a significant support during my PhD work. He has always been patient and helped me in times of difficulty. He has provided me with personal attention through discussions and guidance whenever needed. I am highly indebted to him for helping me understand physics better.

Furthermore, I am very thankful to Prof. Milan Tadić who has helped me understand the intricate concepts of the **k.p** theory. His valuable suggestions on this method has enabled us to publish a paper in collaboration with one of his students. He has also extended a great help through his prompt comments on this thesis.

I am also extremely thankful to all the jury members for their insightful comments and priceless suggestions on this thesis. I would specially like to thank Prof. Nick Schryvers, Prof. Bart Sorée, Prof. Wim Magnus and Prof. Wim Wenseleers for checking the intricate experimental details mentioned in the introduction and perfecting this thesis. I would also like to thank Mr. Sam Roelants, Dr. Ortwin Leenaerts and Prof. Bart Partoens for helping me translate the thesis summary into Dutch. I am also thankful to our secretary Ms. Evans Hilde for all her administrative support.

I would like to extend my thanks to all the CMT group members for their friendly and thought provoking discussions in the kitchen. I would specially like to thank Dr. Hemant Dixit for helping me in preparing this thesis.

I would also like to thank all my friends in Belgium for making my stay

a very memorable and joyful experience. Specially, the Indian student community has always made me feel at home. Antwerp being a cosmopolitan city, gave me an opportunity to know different cultures and help me widen my social circle.

I am very thankful to my family back home who have been a constant support emotionally. And finally, I would like to thank my wife for helping me sail through difficult times.

This work was supported by the Flemish Science Foundation (FWO-Vl) and the Belgium Science Policy (IAP).

V. V. Ravi Kishore

Contents

List of abbreviations

NW	Nanowires
ZB	Zincblende
VLS	Vapor-Liquid-Solid technique
MBE	Molecular beam epitaxy
SiNW	Si Nanowire
FET	Field effect transistor
LED	Light emitting diode
KL	Kohn-Luttinger
CB	Conduction band
HH	Heavy hole band
LH	Light hole band
SO	Split-off band
VBO	Valence band offset
CBO	Conduction band offset
PB	Pidgeon and Brown
BP	Bahder and Pryor

Chapter 1

Introduction

Mankind's endeavor has always been to make life simpler and electronics have a major role in achieving this. Ever since the first transistor has been invented, both the science community and the industry have been thriving hard to increase the number of transistors put on a single chip and there by, make electronics more compact. This has given birth to a new topic of research widely known as "Nanotechnology" or technology at the nano meter scale. Nanowires are one of the technology marvels achieved through nanotechnology.

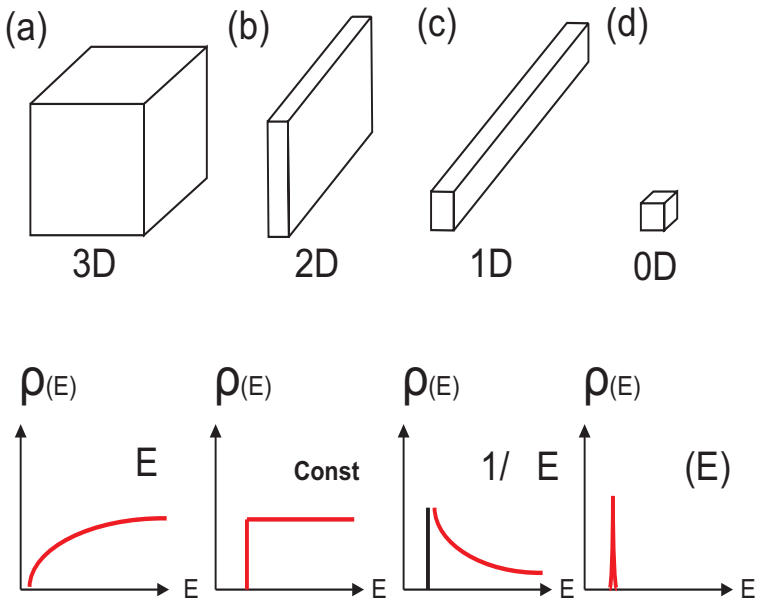

Figure 1.1: Schematic representation and density of states of (a) bulk, (b) quantum wells, (c) quantum wires and (d) quantum dots, respectively.

A nanometer is 10^9 part of a meter and at this scale the classical laws of physics are no more applicable and we need a more advanced quantum physics description. With the availability of modern techniques, it has become possible to confine the movement of charged particles in 1, 2 or 3 dimensions resulting in the formation of quantum wells, quantum wires and quantum dots, respectively. In each case their motion is restricted in the remaining dimensions. These different systems can be distinguished by their density of states $\rho(E)$, which is the number of states per unit volume L^D within the energy range E and $E + \delta E$. Here L is the linear size and D is the number of dimensions of the system. As the dispersion energy is given by $E \propto k^2$, the number of states contained in a D-dimensional sphere in k momentum space is proportional to $(L/2\pi)^D k^D$ and the number per unit volume is therefore proportional to $\propto k^D$ or $\propto E^{D/2}$. Thus, the density of states becomes $\rho(E) \propto E^{\frac{D}{2}-1}$ and hence the density of states of electrons in 1, 2 and 3 dimensional systems are proportional to $E^{\frac{1}{2}}$, E^0 and $E^{-\frac{1}{2}}$ respectively, for quantum wires, quantum wells and bulk (see Figs. 1.1 (a)-(c)). In the case of quantum dots the density of states are just a series of delta functions ($\rho(E) \propto \delta(E - E_{n_x,n_y,n_z})$ where E_{n_x,n_y,n_z} are the confined energies with quantum numbers n_x, n_y, n_z) as the carriers are confined in all the three dimensions (see Fig. 1.1 (d)). Confinement of the charged particles in differ-

ent directions results in the formation of discrete bound states. This effect of having bound states in quantum systems is known as the quantum confinement effect. Fig. 1.2, shows the schematic representation of bands in the bulk and the nanowire forms of a direct band gap semiconductor. Here E_G, Δ, E_P represent the energy gap, split-off energy and the Kane's energy respectively and Γ_6, Γ_8 and Γ_7, represent the symmetry groups. Kane's energy E_P is a measure of electron-hole mixing and will be defined in section 2.3.2. Here CB, HH, LH and SO represent the conduction, the heavy hole, the light hole and the split-off bands respectively. We can see that the quantum confinement results in the formation of the so called subbands.

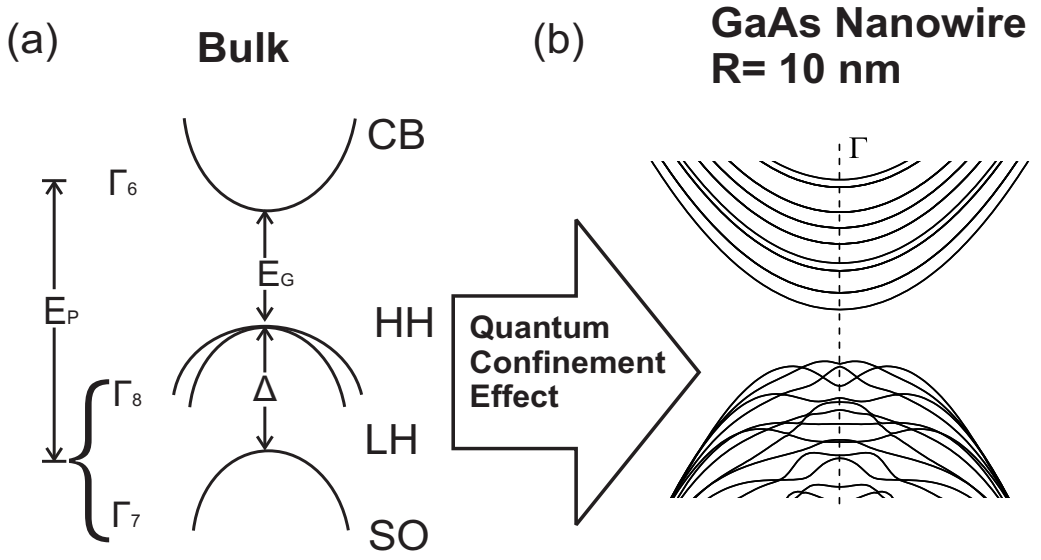

Figure 1.2: Schematic representation of the lowest conduction and valence bands in bulk (a) and nanowire (b) structures.

Among all the three systems, nanowires show some unique properties as they have only one unconfined direction for electron motion. Their unique density of states in the limit of small diameters, can manifest in some electronic and optical properties such as diameter dependent thermal conductivity [1, 2], that are different from their bulk counterparts. Even as they exhibit unique properties they still have local crystal structures closely related to their bulk counter parts, and hence the theoretical predictions of the bulk are still relevant for nanowires. Among insulators, semiconductors and metals, semiconductors show tunable properties and have been explored ex-

tensively. Thus nanowires with semiconducting properties give us an opportunity to have semiconducting behavior with the charged particles restricted to move only in one direction. The above mentioned properties have made semiconductor nanowires very interesting structures for both electronic and optical applications. These unique properties have motivated us to study semiconductor nanowires and henceforth in this thesis nanowires refers to semiconductor nanowires.

Various properties of the single material nanowires have already been studied both theoretically [3, 4] as well as experimentally [5, 6, 7, 8, 9, 10, 11]. In this thesis, we have studied the electronic properties of core-shell nanowires. In this chapter, I first present the various growth techniques, followed by the different properties of nanowires and finally the various applications which have motivated this thesis.

1.1 Nanowire synthesis and growth techniques

"Nanotechnology is manufacturing with atoms"

William Powell

Nanowires of different forms and sizes have been obtained through various growth techniques. These growth techniques can be broadly classified into two categories: the top down approach and the bottom up approach.

1.1.1 Top down approach

The top down approach is a method in which one starts from the bulk material and subsequently reduces its size using techniques such as lithography, etching etc., till the desired size is reached. Lithography is a process of microfabrication where either light (optical lithography [12], X-ray lithography) or electrons (electron beam direct write lithography (EBDW) [13]) is incident across a surface covered with a film (called a resist) to selectively remove either the exposed or the non-exposed regions of the resist. Maskless lithography [14], atomic force microscopic lithography (AFM) [15], extreme ultraviolet lithography (EUV) [16] etc., are some of the other lithographic techniques which are presently used to obtain nanowires of various sizes and forms.

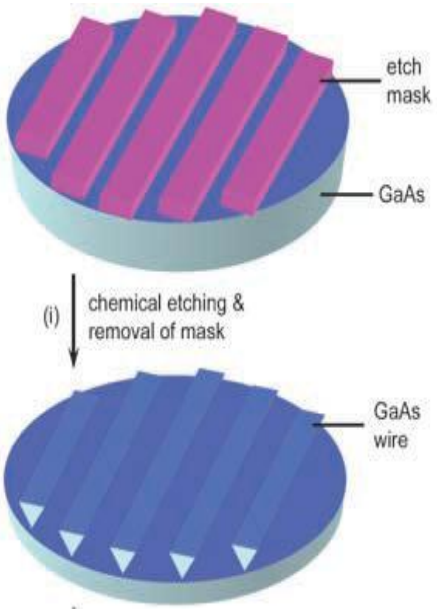

Figure 1.3: Schematic diagram for fabricating GaAs wires with a triangular cross section using chemical etching. Source: Ref. [17]

Fig. 1.3 shows the preparation of GaAs wires with a triangular cross section from a GaAs [100] wafer with mask stripes (SiO_2 or photoresist) along the $[0\overline{1}1]$ direction using chemical etching.

The main advantage of this method is that contacts, connections, control gates etc., can relatively easily be made in order to obtained nanowire circuitry. At present the optical lithography technique uses very short wavelength (193 nm) to produce sub-100 nm patterns. As the device features are pushed to sub-100 nm regime, the conventional methods of lithography used in the present semiconductor industry face both technological and fundamental difficulties [18]. The solution to this problem may lie in using the bottom-up approaches to build specific functional devices whose composition, structure, size and morphology can be controlled during the growth process.

1.1.2 Bottom up approach

In the bottom up approach nanowires are built by putting atoms together one by one, through various physical or chemical processes. Therefore, it can be said that nanowires provide a framework to apply the "bottom-up" approach for the design of nanostructures. Bottom up approaches have taken inspiration from the biological processes occurring in nature. The vapor-liquid-solid

technique is currently a popular process to synthesize semiconductor NWs. Other bottom-up approaches include physical vapor deposition(PVD) [20], chemical vapor deposition (CVD) [21], and metallorganic chemical vapor deposition (MOCVD) [22]. These vapor deposition techniques are capable of preparing smaller diameter ($\leq$ 20 nm) nanowires.

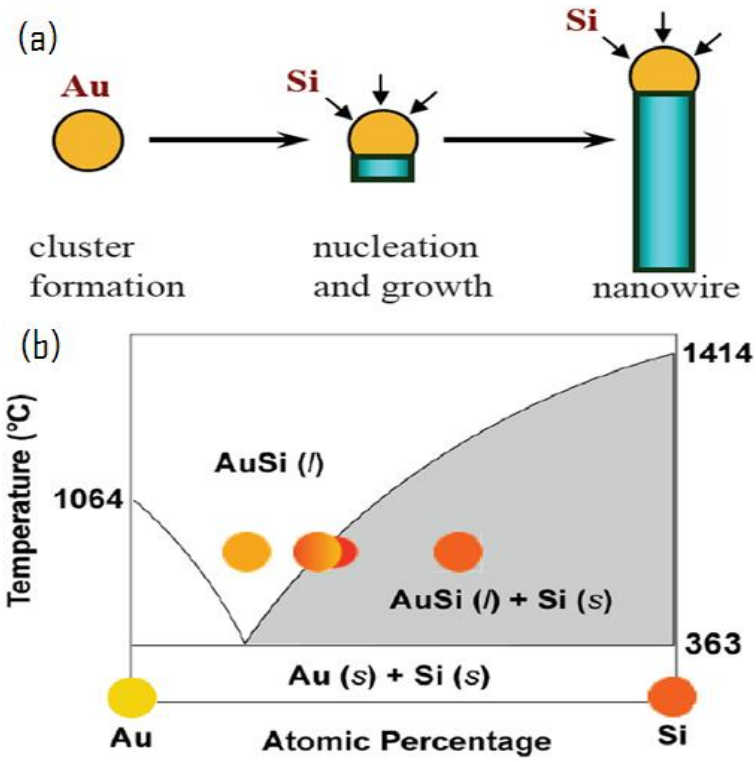

Figure 1.4: Schematic of VLS growth of Si nanowires (SiNWs). (a) Above the eutectic[†]temperature ($363°C$) of Au and Si, a liquid alloy droplet AuSi is first formed . Nucleation and directional nanowire growth is then achieved by continued feeding of Si in the vapor phase into the liquid alloy. (b) Phase diagram for Au and Si illustrating the thermodynamics of VLS growth. Source: Ref. [10]

In recent times, semiconductor nanowires are mostly synthesized using methods based on the vapor-liquid-solid (VLS) technique of crystal growth.

[†]An eutectic system is a mixture of chemical compounds or elements that has a single multiple chemical composition that solidifies at a lower temperature than any other composition made up of the same ingredients. This composition is known as the eutectic composition and the temperature is known as the eutectic temperature.

It was first proposed by Wagner and Ellis [23] in 1964 for the growth of single crystal silicon whiskers from 100 nm to hundreds of microns in diameter. It involves the absorption of a source material in the gas phase into a liquid droplet of a catalyst and after supersaturation of the liquid alloy, a nucleation event generates a solid precipitate of the source material. It is called a seed and can now be used as a preferred site for further deposition of the material at the interface of the liquid droplet and promotes the elongation of the seed into a nanowire or a whisker. As the material is incorporated from the gas phase, it grows anisotropically as a whisker whose diameter is dictated by the diameter of the liquid droplet. This method produces nanowires of high purity (see Fig. 1.4).

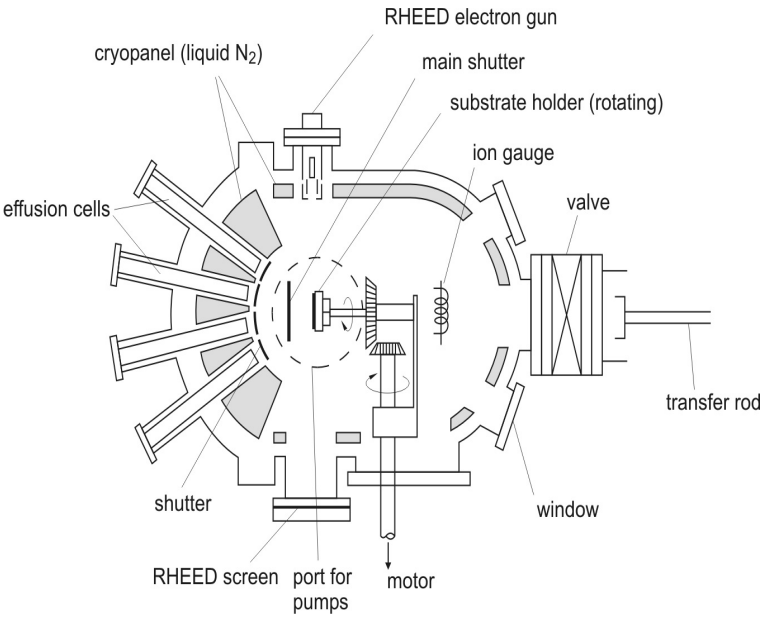

Figure 1.5: Schematic drawing of the MBE growth chamber. Source: Ref. [25]

The molecular beam epitaxy (MBE) technique [24] is based on the VLS technique, where one or more atomic beams obtained by heating solid materials in effusion cells are used to deposit on a heated substrate (see Fig. 1.5). The advantage of this method is that nanowires of many combination of atoms can be obtained, also by varying the ultra high vacuum, different combination of materials can be deposited in both axial direction forming segmented nanowires and radial direction forming core-shell nanowires. The other advantage of this method is that nanowires can be grown without using

the seed material, as in some cases these seed materials (usually *Au* particles) are found to effect the properties of the semiconductor nanowires. Fig. 1.6 shows the schematic representation of MBE-VLS growth mechanism used to grow GaAs nanowires.

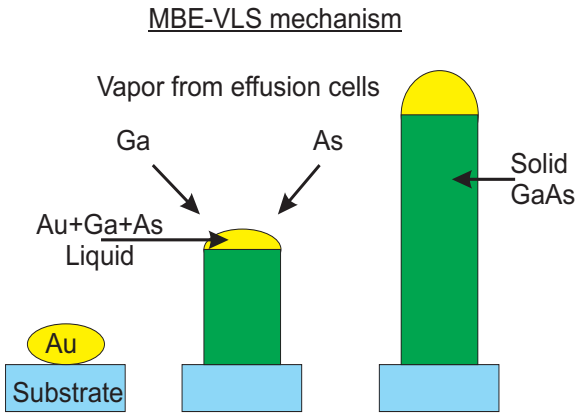

Figure 1.6: Schematic diagram showing the various steps in the MBE-VLS growth of a GaAs NW.

Using these techniques nanowires of group IV semiconductors (Si [26, 27] and Ge [28]) and semiconducting compounds of groups III-V and II-VI (InAs [29], GaAs [30, 31] and CdSe [32]) have been synthesized.

1.1.3 Core-shell nanowire synthesis

As discussed earlier, the VLS technique can be used to grow nanowires with precise dimensions and compositions. Using the MBE technique, nanowires can be grown with various combination of materials. This has led to the preparation of nanowires with the combination of two or more compounds which can form a heterostructure, thus resulting in heterostructure nanowires. Heterostructure nanowires can be further classified into radial or axial (segmented) nanowires depending on how the compounds are grown (see Fig. 1.7). Radial nanowires are more popularly known as core-shell nanowires.

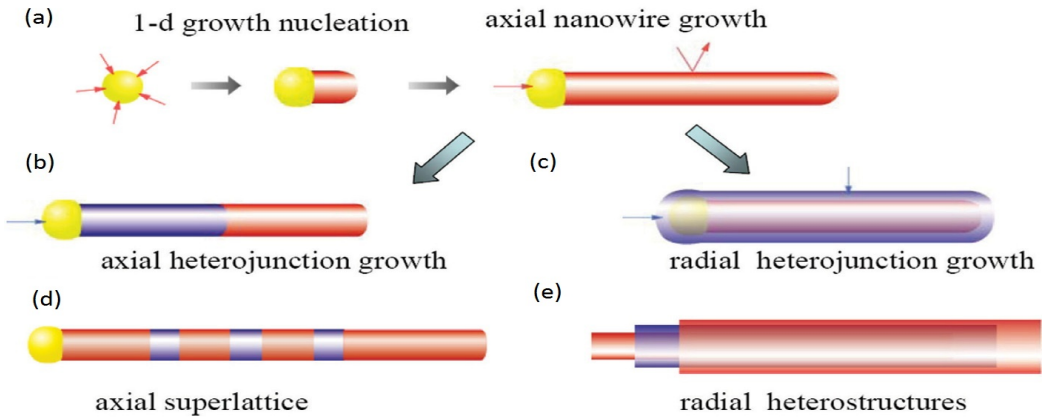

Figure 1.7: Schematic of nanowire and nanowire heterostructure growth. (a) Nanowire synthesis through catalyst-mediated axial growth. (b, d) Switching of the source material results in nanowire axial heterostructures and superlattices. (c, e) Conformal deposition of different materials leads to the formation of core/shell and core/multishell radial nanowire heterostructures. Source: Ref. [8]

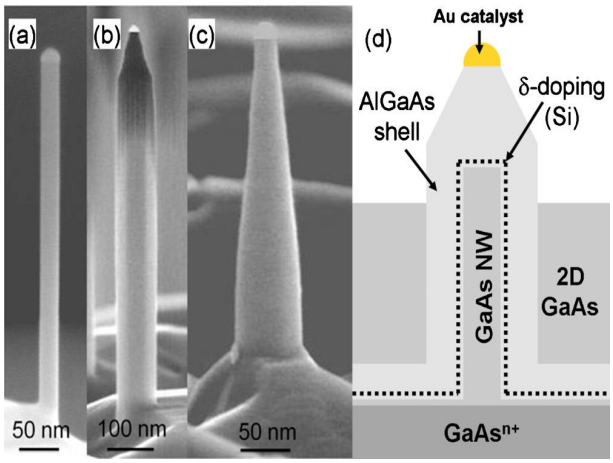

Figure 1.8: Scanning electronic microscope SEM pictures of free standing 25 nm diameter GaAs NWs before (a) and after (b) 40 nm AlGaAs shell growth. (c) Tilted SEM micrograph of the top end of GaAs/AlGaAs core-shell NW after a partial burying in GaAs. (d) Schematic diagram of a GaAs/AlGaAs modulation-doped core-shell NW. Source: Ref. [34]

Both core-shell nanowires and segmented nanowires of various semiconductor compounds such as Si/Ge [33], GaAs/AlGaAs. [34], GaAs/GaSb [35] etc., have already been achieved. Fig. 1.8 shows Scanning electron microscopy pictures of free standing GaAs/AlGaAs core-shell NWs.

Thus, the advance in growth techniques has led to the preparation of high quality NWs of various sizes and also with various combinations of materials.

1.2 Structure and properties of nanowires

Synthesis of nanowires of various sizes and shapes have also resulted in the development of various characterization techniques which can give information on the structure, geometry, defects etc. of these nanowires. Nanowires typically have sizes comparable to the wavelength of visible light, so optical microscopy techniques are limited in characterizing their morphology [36], but at the same time optics could also provide photoluminescence data as shown in Fig. 1.11. On the other hand electron microscopy can give more information as electrons interact more strongly with matter when compared to photons. In practice scanning electron microscopy (SEM), transmission electron microscopy (TEM) (including diffraction techniques) as well as, scanning probe techniques are often used to characterize the nanowires.

1.2.1 Structure and characterization

SEM is usually used to study nanowires of sizes approximately 10 nm diameter and gives information on the structural arrangement, spatial distribution, wire density, and geometry of the nanowire. It is a type of electron microscope which uses a high energy focused electron beam to produce images of a sample. Secondary electrons, back-scattered electrons, and characteristic X-rays are produced when the electrons from the beam interact with the electrons in the sample. The characteristic X-rays thus produced can give information on the sample's composition, whereas the secondary electrons can give information on the sample's surface topography. More detailed geometrical features can be studied using TEM and high resolution transmission electron microscopy (HRTEM). Information on the crystal growth, orientation and the quality of the nanowire can be obtained using TEM. Also, TEM can be combined with other characterization tools such as electron energy loss spectrometry (EELS) or energy dispersive X-ray spectrometry (EDX) within the TEM instrument to probe nanowires with high spatial resolution.

The EELS method provides information on the energy and momentum of the excitations in the nanowire by measuring the energy and momentum of

the incident and the scattered electrons after an inelastic electron scattering process. The EDX technique on the other hand measures the energy and intensity distribution of X-rays generated by the impact of electron beam on the sample. This method is very useful in characterizing the composition of superlattice nanowires due to its ability to determine the elemental composition of the probed area with high precision. Both EELS and EDX methods can give information on the composition of the sample. EELS with a low resolution of 1 eV can be used for light elements, whereas EDX with a resolution of 130 eV can be used for heavy elements.

Apart from the various electron microscopy techniques, there are also several scanning probe techniques such as scanning tunneling electron microscopy (STEM), electric field gradient microscopy (EFM), magnetic field microscopy (MFM), and scanning thermal microscopy along with atomic force microscopy (AFM) which can be used to study structural, electronic, magnetic, and thermal properties of nanowires. STM can reveal information of both the topology as well as the local density of states of the nanowire, when used in the scanning tunneling spectroscopy (STS) mode. Fig. 1.9, shows the EDX linescan data from a GaAs/AlGaAs core-shell nanowire along with its bright field (BF) STEM, dark field (DF) STEM and high angle annular dark field (HAADF) STEM images.

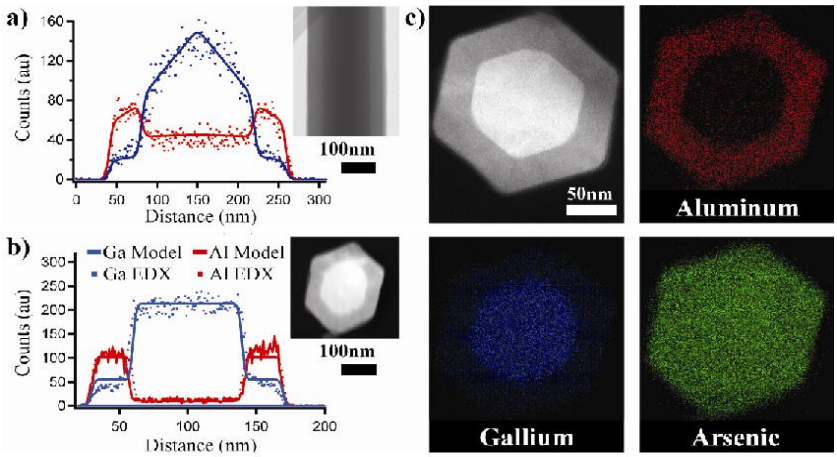

Figure 1.9: a) EDX linescan data from a core-shell nanowire. Inset is BF-STEM image of the nanowire. b) EDX linescan data from a core-shell nanowire collected in cross-section. Inset is DF-STEM image of the nanowire c) HAADF STEM image and corresponding EDX chemical maps. Source: Ref. [37]

Core-shell nanowires: different band alignments

Growth of nanowires with various combination of materials have resulted in core-shell nanowires with different band alignments [38]. These nanowires can be classified into six different types, type I-s, type I-c, type II-s, type II-c, type III-s, and type III-c [38] (see Fig. 1.10), where 'c' and 's' represent the structures with electrons confined in core and shell respectively. These different types have been extensively discussed by Pistol *et. al.* [38].

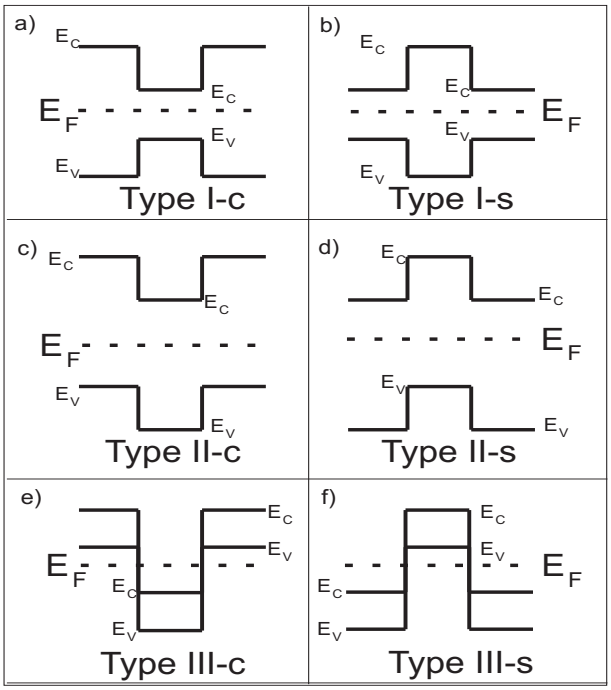

Figure 1.10: Different types of band alignments where E_C is the conduction band, E_V is the valence band and E_F is the Fermi energy.

Type I-s structures have a quantum well in the shell region and are often used in light emitting devices such as lasers where it is advantageous to have a direct bandgap in the well. Type-III and negative bandgap structures can give rise to metallic conductivity even without doping and in some cases simultaneous electron and hole conduction is also possible. In type-II and type-III systems, the electrons and holes can be confined in different regions and are considered to be good candidates for producing excitonic crystals [39]. In this thesis we discuss the electronic and the optical properties of type-I and type-III core-shell nanowires.

1.2.2 Optical properties

Optical properties studied using the various available optical measurements are very sensitive to quantum effects. These measurements do not require any contacts and therefore need minimal sample preparation. Thus they provide easy to setup and highly sensitive tools to study the electronic structure of nanowires. The optical measurements include fluorescence spectroscopy, laser-induced fluorescence, phosphorescence, infra-red absorption, two-photon absorption and X-ray fluorescence.

The above mentioned methods of measurement of transmission and reflection, combined with the Kramer-Kronig relations or the Maxwell's equations can be used to determine the real and the imaginary parts of the dielectric function. Using the dielectric function the plasmon frequency and plasma resonance can be studied. Similarly, the infrared spectra can be used to study plasma frequency, free carrier density and donor impurity as a function of temperature. This is especially useful to study nanowires as Hall effect measurements cannot be made on them.

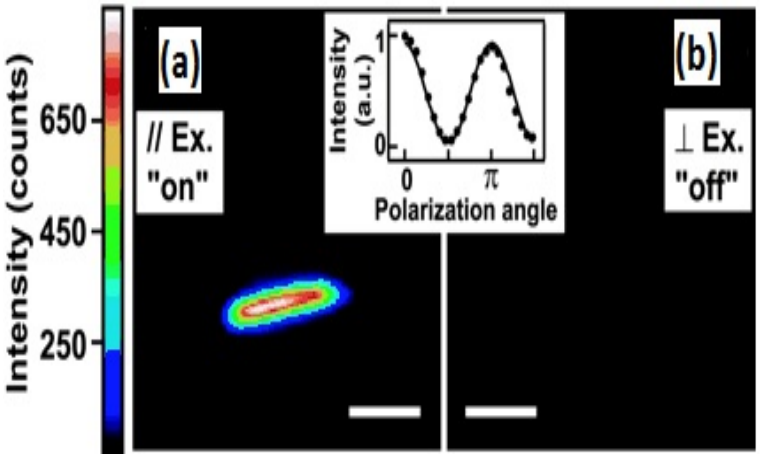

Figure 1.11: (a) PL image of a single 20 nm InP nanowire with the exciting laser polarized along (a) and perpendicular (b) to the wire axis. Scale bar, 3 μm. Inset shows the variation of overall photoluminescence intensity as a function of excitation polarization angle. Source: Ref. [43]

Photo-luminescence or fluorescence spectroscopy is the common method to study nanowires. This method has been used to study properties such as optical-gap behavior, oxygen vacancies in ZnO nanowires [41], strain in Si nanowires [42], and quantum confinement effects in InP nanowires [43] with diameters $\leq$ 20 nm. Wang *et al.* [43] have also shown that InP nanowires

show a giant polarization anisotropy and the PL observed changes from an "on" to "off" state as the polarization of the exciting laser is changed from parallel (see Fig 1.11 (a)) to perpendicular (see Fig 1.11 (a)) to the wire axis which was attributed to the dielectric mismatch between the nanowire and its surroundings. Similar conclusions were made by Zhang *et al.* [44] for GaAs nanowires with smaller diameters.

Magneto-optics along with photo-conductance [45] can be used to study the band parameters such as Fermi surface energy, electron effective masses and the number of subbands to be considered for the nanowires. Non-linear behavior is enhanced in nanowires and has been utilized to study many non-linear optical properties of nanowires such as the measurement of second harmonic generation (SHG) and third harmonic generation (THG) [46].

1.3 Applications

In this section, I present some of the very interesting applications of nanowires. Some of these applications are just mere theoretical predictions and others have been achieved in experimental labs. Industrial realization and mass production of these nanowires is yet to be achieved but it will only be a matter of time before nanowire applications enter the real world.

1.3.1 Electrical and electronic applications

Ever since the invention of the integrated circuit in 1958, the electronics industry has been thriving hard to make electronics more compact and accommodate a higher number of transistors on a single chip. This involved using lithographic techniques to etch the circuit on small substrates of the order of 100 nm in size. The limitations in lithographic techniques to go below 100 nm has led the industry to look for alternative techniques of creating smaller circuits. At this point self-assembly of nanowires appears to be a prospective solution to this problem. Self-assembly of nanowires can eliminate huge costs incurring due to lithographic techniques. Furthermore, the advance in the various growth techniques have resulted in obtaining nanowires with precise dimensions and defect free compositions and thus have increased their prospects of being used in microelectronics.

Semiconductor industry has been dominated by technologies using Si, which obviously has its own limitations. On the other hand nanowires with various combinations of semiconducting materials other than Si have been made possible and thus the various properties of other non-Si semiconductors and their combinations can be utilized in microelectronic devices. It

is observed that junctions of GaAs and GaP show rectifying behavior [47]. Similarly, transistors made from nanowires can have unique advantages due to their morphology. For example, in the case of nanowires the conductor is surrounded by an oxide layer which prevents the formation of the depletion layer formed between source and drain (usually formed in bulk FETs) and hence can reduce the source-drain capacitance in a prospective nanowire field effect transistor (FET). Fig. 1.12 shows a laterally oriented InAs nanowire based FET obtained by Storm *et al.*[49]

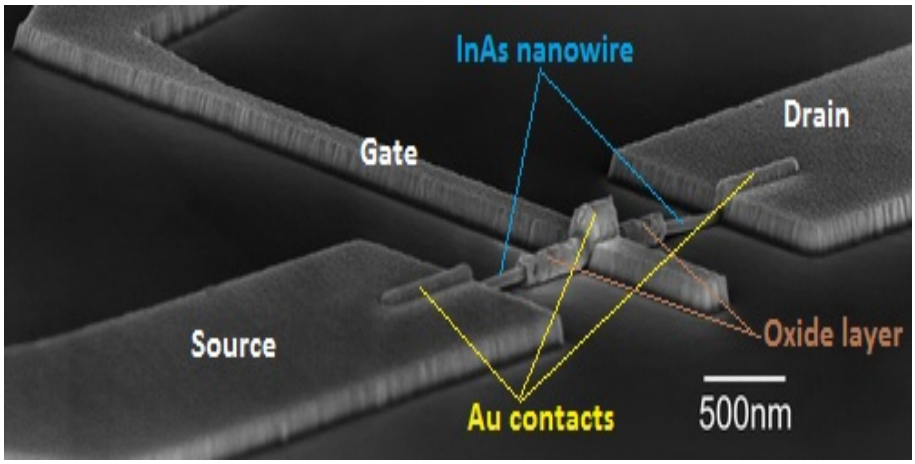

Figure 1.12: Laterally oriented InAs nanowire based field-effect transistors. Source: Ref. [49]

The obvious advantages of nanowires have led many researchers to realize nanowire based technologies of the already established bulk technology counter parts. Some of these technologies such as p-n junction diodes, logic gates, FETs and light emitting diodes (LEDs) based on nanowires have already been achieved. This shows the promise of nanowires to be the building blocks of complex integrated circuits. The two-terminal nanowire devices of p-n junction diodes can be formed at the crossing of two nanowires, or by doping nanowires with various materials. Further, such p-n junction diodes can also be formed in a single nanowire by modulating the composition of the nanowire in either radial direction and thus forming core-shell nanowires, or in axial direction and thus forming segmented nanowires. These p-n junction diodes can be used in the formation of LEDs, nano lasers and photovoltaic devices. Similarly, three terminal devices such as FET's have also been experimentally realized in recent times. Nanowires have also shown promise in being used for thermoelectric applications.

1.3.2 Optical applications

One-dimensional systems of nanowires show singularity in the joint density of states, thus making quantum confinement effects observable even at room temperatures. In the quantum limit the density of states in a nanowire is highly localized in energy. These energy levels are quickly filled with the increase in the intensity of incident light which results in strong optical non-linearities in nanowires. Thus nanowires can yield optical switches with lower switching energies and increased switching speeds [36].

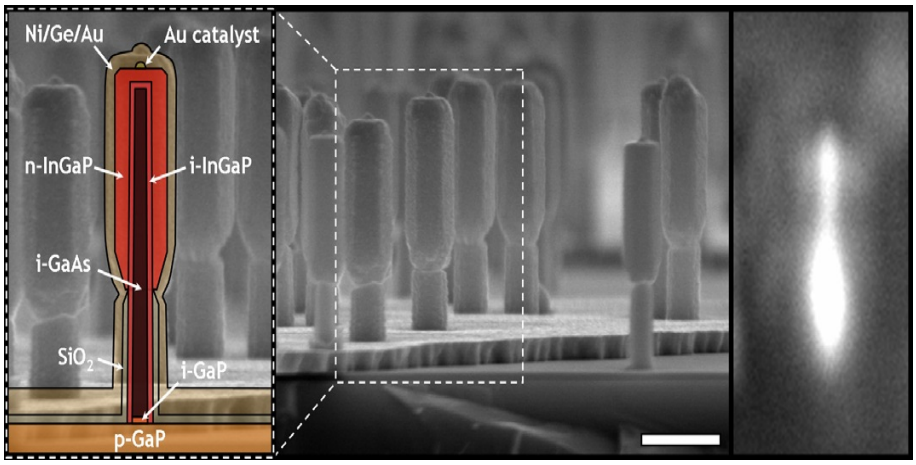

Figure 1.13: Light emitting diodes (LEDs) based on GaAs/InGaP multi-shell nanowires. Source: Ref. [50]

Both photoluminescence (PL) and electroluminescence (EL) can result in light emission in the case of nanowires, where the former involves electron excitation using light and the later using electrons across a p-n junction. LEDs [51] based on electroluminescence have been achieved in junctions between p-type and n-type nanowires or between p-n junctions within core-shell or segmented nanowires. Also light emission is localized in the junction area and is polarized in the case of a superlattice nanowire [47]. Svesson *et al.* [50], have fabricated vertical light emitting diodes (LEDs) based on GaAs/InGaP core/shell nanowires, epitaxially grown on GaP and Si substrates (see Fig. 1.13). They show p-nid-n (nid = non intentionally doped) diode structures in which the Si and GaP substrates function as common p-layers to the devices. Thus the device stack is given as (p-Si or p-GaP substrate)/nid-GaP(NW)/nid-GaAs(NW)/nid-InGaP(cladding)/n-InGaP (cap) where the 60 nm thick nid-GaP segment acts as a nucleation segment for improved growth quality.

Quantum wires with p-n junctions can also be used for laser applications [52, 53] as they exhibit lower excitation thresholds and show decreased temperature sensitivity in their performance. Also, by changing the size and the composition of the nanowire, the emission wavelength can be modified. Hua *et al.* [54] have reported lasing action in single GaAs/GaAsP coaxial coreshell nanowires in the infra-red region. Recently, Gallo *et al.* [55] have reported picosecond response times in GaAs/AlGaAs core-shell nanowire based photodetectors.

1.3.3 Photovoltaic applications

Nanowire based solar cells [9] hold the promise of both reducing the reflection losses [56, 57] and improving the light collection [58] when compared to their thin film counterparts presently available in the market. Nanowires grown at very high growth rate on various cheap [59], flexible and low-weight substrates can result in economically viable solar cell applications. Also, an ultra short absorption length can be implemented in the direct bandgap semiconductors having a core-shell structure. Furthermore, core-shell geometry was predicted to yield an extremely efficient carrier collection [60] as it provides an orthogonalization of charge and light pathways. The above advantages combined with the availability of various growth techniques to obtain p-n junctions by doping, have made core-shell and multi-shell nanowires promising candidates for photovoltaic applications.

MBE grown GaAs p-i-n [61] and p-n radial structures [62] have already been obtained and their photocurrent measurements have resulted in conversion efficiencies of 4.5% [63] and 0.83% [64] respectively. Radial GaAs nanopillar p-n junction solar cells grown via selective area metal-organic vapor epitaxy (MOVPE) have shown a conversion efficiency of 2.54% [65]. And more recently, Gutsche *et al.* [66] have demonstrated conversion efficiencies of 4.7% in n-GaAs/InGaP/p-GaAs core-multishell nanowires.

1.3.4 Sensors

Nanowires can act as sensing probes for chemical and biochemical substances as they can offer smaller, more sensitive, less power consuming, and faster reacting sensors. Nanowire sensor operation involves the reversible change in the conductance of the nano-structure upon absorption of the agent to be detected. As nanowires have large surface to volume ratio and small cross-section available for conduction channels, they show increased sensitivity and faster response time.

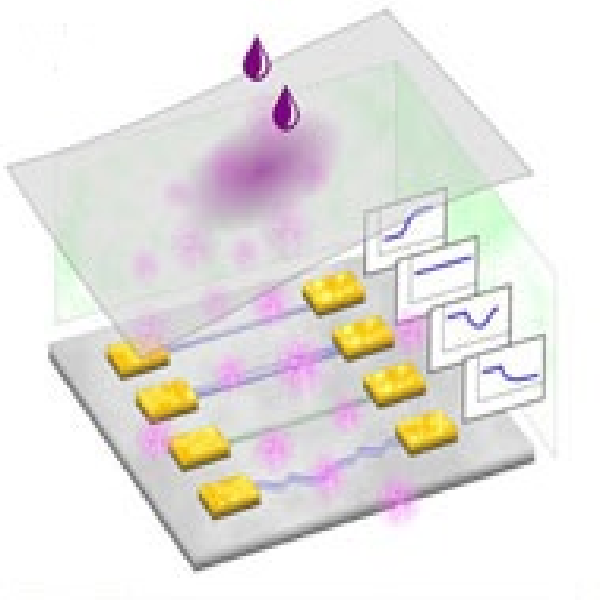

Figure 1.14: Schematic of the experimental set-up where NW FETs are used as sensors. Source: Ref. [67]

Fig. 1.14 shows the schematic of the experimental setup used by Niskanen *et al.* [67] where NW FETs are packaged and connected inside a measurement box with a few-centimeter diameter hole that is covered by a clean paper tissue. These NW FETs are used as nanowire sensor devices. Arrays of nanowire sensor devices of various diameters and different orientations have been used to detect the composition of chemical solvents such as methanol, ethanol and isopropanol. Cui *et al.* [68] have demonstrated a direct readout nanowire pH meter by placing Si NW between two metal electrodes and modifying the silicon oxide coating of the wire with the addition of molecules that are sensitive to the analyte to be detected. Protonation and deprotonation of the NH_2 and SiOH groups on the surface of the nanowire was caused when there are variations in the pH of the solution in which the nanowire was immersed. This leads to the variation in charge densities and the conductance of the nanowire showed a linear dependence on pH in the pH range 2 to 9. This approach can also be used to detect the binding of bio molecules, such as streptavidin using biotin-modified NWs [68]. Thus, various combination of nanowires of different materials can be used to develop fast and efficient sensing devices.

From the above discussed properties and applications of nanowires and core-shell nanowires, it is evident that nanowires can play a very impor-

tant role in the development of future electronic and opto-electronic devices. We are specially interested in semiconductor nanowires of III-V compounds which have a direct bandgap and show interesting electronic and optical properties. In order to have a comprehensive understanding of their various electronic and optical properties, it is essential that we study their electronic structure in detail. This has been the motivation for my thesis.

1.4 Theoretical Methods

In order to understand the electronic and optical properties of nanowires it is essential to understand their band structure. Bandstructure of nanowires can be studied using both ab-initio techniques based on the density functional theory (DFT) and also semi-empirical methods such as the tight binding (TB) method and the **k.p** method.

1.4.1 First principle methods

The first principle methods involve studying the band structure using only the basic physics laws with minimal use of approximations. The density functional theory (DFT) is a modeling technique to study electronic structure of many body systems. The properties of a many electron system can be studied using the electron density. Standard computer packages for DFT study such as ABINIT, VASP, etc. are already available. DFT is very successful in studying the electronic properties of thin nanowires (diameter D=1-2 nm) but for thicker nanowires it is computationally very expensive or even impossible. Very thin Si nanowires and Si/Ge core-shell nanowires have been successfully studied using this method (Ref. [69, 4]).

1.4.2 Empirical tight binding method

The tight binding method uses an approximate set of wave functions based on the superposition of wave functions for isolated atoms located at each atomic site. It is closely related to the linear combination of atomic orbitals (LCAO) method used in chemistry.

TB method has been used to study the zincblende embedded [70] and freestanding nanowires [71, 72, 73, 74, 75, 76, 77]. The main advantages of this method are that it is atomistic and uses full Brillouin zone parameters.

1.4.3 The k.p method

The **k.p** method is a semi-empirical method which is used to study the bandstructure near a particular k point in the Brillouin zone. It was originally introduced by Bardeen and Seitz and later, the Kohn-Luttinger (KL) model [78, 79, 80, 81, 82] was developed where it was used to study the valence bands, i.e. the heavy hole, light hole and the split-off bands. It was initially used only to study the direct band gap materials, but recently it has also been used to study indirect band gap materials. It is a computationally relatively inexpensive method and uses band parameters such as bandgap, effective mass, Luttinger parameters which are determined from experiments or from first principle calculations. Using the envelope function method it was easily modified to describe heterostructures. Pikus and Bir have modified the Hamiltonian to include the effects of strain [83, 84].

The **k.p** method can be used to describe both conduction and valence bands and depending on the number of bands included it can be called 2 band, 4-band, 6-band, 8-band and so on **k.p** theory. The choice of the number of bands included in a **k.p** method depends on the band parameters such as bandgap E_G and split-off energy Δ_{SO}. For large bandgap materials, both conduction band and valence bands can be treated independently. The **k.p** method can also be modified to study the whole Brillouin zone, by including the influence of remote bands [85]. And recently, a 40 band **k.p** method [86] was constructed. This method has been successfully used to study bulk materials of both direct bandgap materials such as GaAs, InAs, GaSb, InSb, etc. and indirect bandgap materials such as Si and Ge. It has also been used to study quantum structures such as quantum dots, quantum wells, quantum wires and superlattice structures. This method is particularly useful in studying the optical properties as it involves the study of bands closer to the zone center. It uses input parameters from experiment or from first principle calculations and hence its accuracy depends largely on the accuracy of these parameters.

I have used different models of the **k.p** method to describe nanowires and a detailed description of this method is given in the second chapter.

1.5 Outline of this thesis

In this thesis we study the freestanding [87] single material and core-shell nanowires of III-V compounds with zincblende structure grown in [001] crystallographic direction. This thesis is organized in the following manner. In chapter 2, I have presented the **k.p** method and its different variants which

I have used throughout my PhD. I have first presented the basic concept of the **k.p** method using the effective mass approximation. Using the effective mass approximation the single band solutions can be obtained for both bulk and nanosystems. Later in the chapter, I have introduced the 4-band and the 6-band Kohn-Luttinger (KL) Hamiltonians to describe the valence band of widegap ($E_G > 1$ eV) semiconductors like GaAs, as the conduction and the valence band states can be studied independent of each other in these cases. But, this is no longer the case for narrow gap semiconductors, where the conduction and valence band states have a considerable influence on each other. In this case an 8-band KL Hamiltonian is used, where the conduction band influence on the valence band and vice versa is taken into consideration using the Kane parameter P. The **k.p** method in this form cannot be applied to the nanostructures where they are usually comprised of heterostructures with one or more combinations of materials. To overcome this difficulty I have used the symmetrized Kohn-Luttinger Hamiltonian. And finally I have explained how the magnetic field terms can be included in the **k.p** method.

In chapter 3, I have presented the electronic and optical properties of widegap semiconductor nanowires. As an example, results for GaAs, $Al_xGa_{1-x}As$ single material and core-shell nanowires were presented. Results for the energy band spectrum, the optical absorption and the density of charge of carriers are presented for these nanowires. For this study we have used both the 4-band and the 6-band KL Hamiltonians to describe the valence band states and the single band KL Hamiltonian to describe the conduction band states. We found that there are observable differences between the valence band ground state spectrum generated through the 4-band and the 6-band Hamiltonians for thin nanowires. These differences were identified and explained. The importance of the presence of the split-off band is explained and emphasized. Finally results for the $GaAs/Al_xGa_{1-x}As$ and $Al_xGa_{1-x}As/GaAs$ core-shell nanowires are presented. We found that the top of the valence band showed a characteristic feature called the camel-back structure. The presence or absence of the camel back structure and its implications on the band structure and optical properties are discussed extensively for both single material and core-shell nanowires of GaAs and $Al_xGa_{1-x}As$. Finally, the density of both holes and electrons in $GaAs/Al_xGa_{1-x}As$ and $Al_xGa_{1-x}As/GaAs$ core-shell nanowires are presented.

Both the 4-band and 6-band models are very useful in studying nanowires of widegap semiconductor materials. But, as stated in chapter 2, for narrow bandgap semiconductors like InAs and InSb where $E_G < 1$ eV and $E_G \simeq \Delta$, a more comprehensive method which includes the influence of the conduction band on the valence band and vice versa is required. So, in chapter 4 we study the valence band properties of GaAs, InAs and InSb, using the 8-band

KL Hamiltonian described in chapter 2. In the case of the 8-band model the Luttinger parameters (γ_j) used in the 4 and 6-band models are replaced with Luttinger-like parameters ($\tilde{\gamma}_j$). In literature there were two suggested methods available to calculate the Luttinger-like parameters one is the Pidgeon and Brown (PB) [88] method the other is the Bahder and Pryor (BP) [89, 90] method. A comparison of the valence band results using the 6-band model, 8-band PB model and 8-band BP model are presented. We decided that the Luttinger-like parameters using the PB model are more accurate and were therefore used in the rest of the study. Further, the Luttinger-like parameters for the split-off band needed to be modified if $E_G \simeq \Delta$, the implications of this treatment have also been presented. In both 8-band models (PB and BP), the influence of the conduction band on the valence band states is introduced using the Kane parameter E_P. So finally, the influence of the value of E_P on the valence band ground state (showing camel-back structure) is discussed for the three different materials GaAs ($E_G \gg \Delta$), InAs ($E_G \simeq \Delta$ and InSb ($E_G \ll \Delta$).

In chapter 3, I have presented the electronic and optical properties of GaAs/$Al_xGa_{1-x}As$ and $Al_xGa_{1-x}As$/GaAs core-shell nanowires which have a type-I band alignment. Depending on the constituent materials in the heterostructure, the band alignments can be classified as type-I, type-II and type-III. In chapter 5, I have presented the electronic properties of InAs/GaSb nanowires which have a type-III band alignment. The specialty of this heterostructure is that electrons and holes confine in different regions of the heterostructure. Here the valence band minimum of GaSb is found to be above the conduction band maximum of InAs. Thus, the lowest conduction band state is found to be in InAs and the highest valence band state is found to be in the GaSb region of the heterostructure. Thus, in the case of InAs/GaSb, the electrons confine in the InAs region and holes confine in the GaSb region. The implications of such a structure is that for certain sizes of InAs and GaSb, mixing occurs between the lowest conduction band state and the highest valence band state. This results in a gap-less configuration, where the highest valence band state occurs above the lowest conduction band state so that the effective band obtained is negative. The properties of such configurations with a negative effective bandgap and how the size of both InAs and GaSb influences these configurations is discussed in this chapter.

Finally, in chapter 6 I study the electronic and optical properties of nanowires with magnetic field applied along the z-direction. I first give a detailed account of the various transformations needed to include the effect of a magnetic field in the 8-band KL Hamiltonian. First, I study the properties of single material nanowires and later in the chapter, I study type-I

core-shell nanowires. As stated in chapter 5, type-I band alignment can be further classified into type-Ic and type-Is band alignments where type-Ic has electrons confined in the core and type-Is in the shell. Thus both single material nanowires and core-shell nanowires with type-Ic band alignment have electrons confined in the core and type-Is has electrons confined in the shell. Core-shell nanowires with type-Is band alignment is similar to a quantum ring system with a finite potential at its inner radius. Thus the study of these nanowires with charges confined in different regions of the nanowire, give us an opportunity to study properties such as the Fock-Darwin states and the Aharonov-Bohm oscillations.

Chapter 2

The k.p method

The electronic structure of nanowires can be studied using the density functional theory, the tight binding method and the effective mass approximation techniques. We use the **k.p** method [78, 79, 80, 81, 82] combined with the effective mass approximation in our calculations, as it is a computationally economical method which can also handle thick quantum wires. In the **k.p** method, perturbation theory is used to study both energy and wavefunctions in the vicinity of the Γ point (zone center). Depending on the number of bands included in the study, different **k.p** models have been proposed. In this method we can easily include both the effects of internal potentials such as strain [83, 84], asymmetry etc., which arise due to the choice of the materials of the core and the shell and the external potentials such as electric and magnetic fields. The **k.p** method is equally successful in describing both zincblende [78, 81, 82] as well as wurtzite [91] crystal structures. In this chapter I give the theoretical description of the different models of the **k.p** method which I have used to study the core-shell nanowires. In the next section we present the **k.p** method for the bulk systems which is later applied to the nanostructures using the envelope function approximation (EFA).

2.1 The basic concept

First I consider a single electron Schrödinger equation Eq.(2.1) which describes the motion of electron in a periodic potential $V(\mathbf{r}) = V(\mathbf{r} + \mathbf{R})$,

$$\left[\frac{p^2}{2m_0} + V(\mathbf{r})\right] \Psi(\mathbf{r}) = E(\mathbf{k})\Psi(\mathbf{r}), \tag{2.1}$$

where m_0 is the free electron mass and $\mathbf{R}$ is the lattice vector. Using the translational symmetry in the lattice vector $\mathbf{r} \rightarrow \mathbf{r} + \mathbf{R}$, the general solution

of Eg.(2.1) can be written as

$$\Psi_{n\mathbf{k}}(\mathbf{r}) = e^{[i\mathbf{k}.\mathbf{r}]}u_{n\mathbf{k}}(\mathbf{r}), \tag{2.2}$$

where $u_{n\mathbf{k}}(\mathbf{r}+\mathbf{R}) = u_{n\mathbf{k}}(\mathbf{r})$ is a periodic function. Energy E is given by $E = E_n(\mathbf{k})$, where n is the electron band index and $\mathbf{k}$ is the wave vector of the electron. This is known as the Bloch theorem and the wavefunction $\Psi_{n\mathbf{k}}(\mathbf{r})$ is known as the Bloch wavefunction.

Now, using this Bloch wavefunction in the Schrödinger equation Eq.(2.1), we get

$$\left[\frac{p^2}{2m_0} + \frac{\hbar}{m_0}\mathbf{k}.\mathbf{p} + V(\mathbf{r})\right] u_{n\mathbf{k}}(\mathbf{r}) = \left[E_n(\mathbf{k}) - \frac{\hbar^2k^2}{2m_0}\right] u_{n\mathbf{k}}(\mathbf{r}). \tag{2.3}$$

At $\mathbf{k} = 0$ which is the zone center, the Hamiltonian can be written as $H_0 = p^2/2m_0 + V(\mathbf{r})$. This Hamiltonian has the following solution

$$\left[\frac{p^2}{2m_0} + V(\mathbf{r})\right] u_{n0}(\mathbf{r}) = E_n(0)u_{n0}(\mathbf{r}). \tag{2.4}$$

Now using the time-independent perturbation theory (see Appendix A), Eq.(2.3) can be solved to obtain the energy given by

$$E_n(\mathbf{k}) = E_n(0) + \frac{\hbar^2k^2}{2m_0} + \frac{\hbar^2}{m_0^2}\sum_{n\neq n'}\frac{|\mathbf{k}.\mathbf{p}_{nn'}|^2}{E_n(0) - E_n'(0)}, \tag{2.5}$$

and the corresponding wavefunction to the first order perturbation is given by

$$u_{n\mathbf{k}}(\mathbf{r}) = u_{n0}(\mathbf{r}) + \frac{\hbar}{m_0}\sum_{n\neq n'}\left[\frac{|\mathbf{k}.\mathbf{p}_{nn'}|}{E_n(0) - E_n'(0)}\right] u_{n0}(\mathbf{r}), \tag{2.6}$$

where the momentum matrix elements are given by

$$\mathbf{p}_{nn'} = \int_{unitcell} u_{n0}^*(\mathbf{r})\mathbf{p}u_{n'0}(\mathbf{r})d\mathbf{r}. \tag{2.7}$$

The above described method is known as the single band **k.p** method and has been used to study the conduction band in the bulk materials. From

Eq.(2.5) it is clear that the effect of the crystal potential on an electron can be approximated by replacing the free electron mass m_0 with an effective mass m^*. Thus,

$$E_n(\mathbf{k}) = E_n(0) + \frac{\hbar^2 k^2}{2m^*}, \tag{2.8}$$

where the effective mass m^* is given by

$$\frac{1}{m^*} = \frac{1}{m_0} + \frac{2}{m_0^2 k^2} \sum_{n \neq n'} \frac{|\mathbf{k}.\mathbf{p}_{nn'}|^2}{E_n(0) - E'_n(0)}. \tag{2.9}$$

The above described equations do not include the spin-orbit interaction (SOI) term. With the inclusion of the spin-orbit interaction term the equations Eq.(2.1) is now modified as,

$$\left[\frac{p^2}{2m_0} + \frac{\hbar}{m_0}\mathbf{k}.\mathbf{p} + \frac{\hbar^2 k^2}{2m_0} + V(\mathbf{r}) + \frac{\hbar}{4m_0^2 c^2}(\boldsymbol{\sigma} \times \nabla V) \cdot \mathbf{p}\right] u_{n\mathbf{k}}(\mathbf{r}) = E(\mathbf{k}) u_{n\mathbf{k}}(\mathbf{r}). \tag{2.10}$$

$$E_n(\mathbf{k}) = E_n(0) + \frac{\hbar^2}{2} \sum_{\alpha\beta} k_\alpha \frac{1}{\mu_n^{\alpha\beta}} k_\beta, \qquad \alpha, \beta = x, y, z, \tag{2.11}$$

where

$$\frac{1}{\mu_n^{\alpha\beta}} = \frac{1}{m_0}\delta_{\alpha\beta} + \frac{2}{m_0^2} \sum_{m \neq n} \frac{\Pi_{mn}^\alpha \Pi_{nm}^\alpha}{E_{n0} - E_{m0}}, \tag{2.12}$$

is the effective mass tensor with the momentum matrix element defined as

$$\mathbf{\Pi} = \mathbf{p} + \frac{\hbar}{4m_0^2 c^2}(\boldsymbol{\sigma} \times \nabla V), \tag{2.13}$$

and

$$\mathbf{\Pi}_{nm} = \int_{unitcell} u_{n0}^*(\mathbf{r}) \mathbf{\Pi} u_{m0}(\mathbf{r}) d\mathbf{r}. \tag{2.14}$$

The **k.p** method described above is applicable only to the conduction band in the bulk systems. But, this is not sufficient to describe the valence band and can be done using the multiband **k.p** models.

2.2 Multiband k.p methods

Kohn-Luttinger model has extended the single band **k.p** method to model the top most valence bands of heavy hole and light hole [79]. Later, even the split-off band study was included for a complete description of the valence band. These models give reasonably accurate results for the wide gap semiconductors where the conduction and the valence bands can be treated independent of each other. But, for smaller bandgap materials, the influence of the conduction band on the valence band and vice-verse is also essential. This is achieved by the so called extended Kane model resulting in constructing an 8-band Hamiltonian.

2.3 Kohn-Luttinger Hamiltonian

The top of the valence bands in III-V semiconductors have a Γ_4 like symmetry apart from the spin. The spatial parts of theses bands at the zone center ($k = 0$) are *p-like*, i.e., they are triply degenerate and transform like the three components of a vector. Including spin this leads to six band edge Bloch functions denoted by $|X\rangle|\sigma\rangle$, $|Y\rangle|\sigma\rangle$ and $|Z\rangle|\sigma\rangle$ with $\sigma = \uparrow, \downarrow$.

It is convenient to introduce a new basis set of p-symmetric atomic Bloch states as a linear combination of the "directed orbital" atomic Bloch states u_{n0} discussed previously. The new basis set will be eigenfunctions of $\mathbf{J}^2$ and J_z where the total angular momentum $\mathbf{J}$ equals the sum of the orbital angular momentum $\mathbf{L}$ and the spin angular momentum $\mathbf{S}$.

This new basis set is denoted by $|jm_j\rangle$ where $j = 1/2\ and\ 3/2$ and $m_j = j, j-1, ...0..., -j$. Thus we have the 6 sub-bands defined as

$$|\frac{3}{2}, \frac{3}{2}\rangle = \frac{1}{\sqrt{2}}|X + iY\rangle|\uparrow\rangle,$$

$$|\frac{3}{2}, \frac{1}{2}\rangle = \frac{1}{\sqrt{6}}|X + iY\rangle|\downarrow\rangle - \sqrt{\frac{2}{3}}|Z\rangle|\uparrow\rangle,$$

$$|\frac{3}{2}, -\frac{1}{2}\rangle = -\frac{1}{\sqrt{6}}|X + iY\rangle|\uparrow\rangle - \sqrt{\frac{2}{3}}|Z\rangle|\downarrow\rangle,$$

$$|\frac{3}{2}, -\frac{3}{2}\rangle = \frac{1}{\sqrt{2}}|X - iY\rangle|\downarrow\rangle,$$

for the $j = 3/2$ quadruplet and

$$|\frac{1}{2}, \frac{1}{2}\rangle = \frac{1}{\sqrt{3}}|X + iY\rangle|\downarrow\rangle + \frac{1}{\sqrt{3}}|Z\rangle|\uparrow\rangle,$$

$$|\frac{1}{2}, -\frac{1}{2}\rangle = -\frac{1}{\sqrt{3}}|X - iY\rangle|\uparrow\rangle + \frac{1}{\sqrt{3}}|Z\rangle|\downarrow\rangle, \tag{2.15}$$

for $j = 1/2$ doublet.

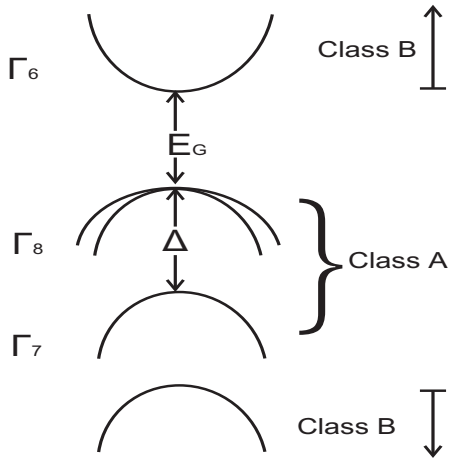

Figure 2.1: Schematic representation of the valence band states.

Here the heavy holes (HH)($m_j = \pm 3/2$) and the light holes (LH)($m_j = \pm 1/2$) have Γ_8 symmetry whereas the doublet split-off (SO) band states have Γ_7 symmetry. Thus in the KL Hamiltonian we are only interested in the top most valence bands (HH, LH and SO). So, we can treat that the above states belong to class **A** and all the other states belong to class **B** and apply Löwdin's perturbation theory (see Fig. 2.1). We can expand the eigenfunctions of this Hamiltonian as

$$u_{\mathbf{k}}(\mathbf{r}) = \sum_{j'}^{A} a_{j'}(\mathbf{k}) u_{j'0}(\mathbf{r}) + \sum_{l}^{B} a_l(\mathbf{k}) u_{l0}(\mathbf{r}), \tag{2.16}$$

where j' is in class **A** and l is in class **B**.
Now using the Löwdin's method we need to solve only the following eigenequation

$$\sum_{j'}^{A} U_{jj'}^{A} - H_{jj'}\delta_{jj'}a_{j'}(\mathbf{k}) = 0, \tag{2.17}$$

instead of

$$\sum_{j'}^{A}(H_{jj'} - E\delta_{jj'})a_{j'}(\mathbf{k}) = 0, \tag{2.18}$$

where

$$U_{jj'}^{A} = H_{jj'} + \sum_{l\neq j,j'}^{B} \frac{H_{jl}H_{lj'}}{(E_0 - E_l)} = H_{jj'} + \sum_{l\neq j,j'}^{B} \frac{H_{jl}^{'}H_{lj'}^{'}}{(E_0 - E_l)}. \tag{2.19}$$

$$H_{jj'} = \langle u_{j0}|H|u_{j'0}\rangle = \left[E_j(0) + \frac{\hbar^2 k^2}{2m_0}\right]\delta_{jj'} \qquad (j, j^{'} \in A). \tag{2.20}$$

$$H_{jl}^{'} = \langle u_{j0}|\frac{\hbar}{m_0}\mathbf{k}\cdot\mathbf{\Pi}|u_{l0}\rangle \cong \sum_{\alpha}\frac{\hbar k_\alpha}{m_0}p_{jl}^{\alpha} \qquad (j \in A, l \notin A, \alpha \in x, y, z), \tag{2.21}$$

where $\Pi_{jj'} = 0$, for $j, j^{'} \in A$, and $\Pi_{jl}^{\alpha} \simeq p_{jl}^{\alpha}$ for $j \in A$ and $l \notin A$. Since $l \neq j$, adding the unperturbed part to the perturbed part in $H_{jl}^{'}$ does not effect the results, i.e., $H_{jj} = H_{jj'}$. We thus obtain

$$U_{jj'}^{A} = \left[E_j(0) + \frac{\hbar^2 k^2}{2m_0}\right]\delta_{jj'} + \frac{\hbar^2}{m_0^2}\sum_{l\neq j,j'}\sum_{\alpha\beta}\frac{k_\alpha k_\beta p_{jl}^{\alpha}p_{lj'}^{\beta}}{E_0 - E_l} \quad (\alpha, \beta \in x, y, z). \tag{2.22}$$

Let $U_{jj'}^{A} \equiv D_{jj'}$. The matrix form of $D_{jj'}$ is given by

$$D_{jj'} = E_j(0)\delta_{jj'} + \sum_{\alpha\beta} D_{jj'}^{\alpha\beta}k_\alpha k_\beta, \tag{2.23}$$

where $D^{\alpha\beta}_{jj'}$ is defined as

$$D^{\alpha\beta}_{jj'} = \frac{\hbar^2}{2m_0}\left[\delta_{jj'}\delta_{\alpha\beta} + \sum_l^B \frac{p^\alpha_{jl}p^\beta_{lj'} + p^\beta_{jl}p^\alpha_{lj'}}{m_0(E_0 - E_l)}\right]. \tag{2.24}$$

The matrix elements $D_{jj'}$ can be explicitly written as

$$D^{xx}_{jj'} = A_0 = \frac{\hbar^2}{2m_0} + \frac{\hbar^2}{m_0^2}\sum_l^B \frac{p^x_{jl}p^x_{lj'}}{E_0 - E_l}. \tag{2.25}$$

$$D^{yy}_{jj'} = B_0 = \frac{\hbar^2}{2m_0} + \frac{\hbar^2}{m_0^2}\sum_l^B \frac{p^y_{jl}p^y_{lj'}}{E_0 - E_l}. \tag{2.26}$$

$$D^{xy}_{jj'} = C_0 = \frac{\hbar^2}{m_0^2}\sum_l^B \frac{p^x_{jl}p^y_{lj'} + p^y_{jl}p^x_{lj'}}{E_0 - E_l}, \tag{2.27}$$

and define the Luttinger parameters γ_1, γ_2 and γ_3 as

$$-\frac{\hbar^2}{2m_0}\gamma_1 = \frac{1}{3}(A_0 + 2B_0). \tag{2.28}$$

$$-\frac{\hbar^2}{2m_0}\gamma_2 = \frac{1}{6}(A_0 - B_0). \tag{2.29}$$

$$-\frac{\hbar^2}{2m_0}\gamma_3 = \frac{C_0}{6}. \tag{2.30}$$

These Luttinger parameters are usually obtained through experiments or first principle calculations.

2.3.1 4 and 6-band Hamiltonian

Using the above formalism the following 4-band Kohn-Luttinger Hamiltonian [78, 81, 82] is obtained and is given by,

$$H^4_{KL} = \frac{-\hbar^2}{2m_0}\begin{pmatrix} P+Q & -S & R & 0 \\ -S^\dagger & P-Q & 0 & R \\ R^\dagger & 0 & P-Q & S \\ 0 & R^\dagger & S^\dagger & P+Q \end{pmatrix}.$$

The 6-band Hamiltonian which includes split-off band states in addition to the heavy hole and light hole bands is given by,

$$H^6_{KL} = \frac{-\hbar^2}{2m_0} \begin{pmatrix} P+Q & -S & R & 0 & -\frac{1}{\sqrt{2}}S & -\sqrt{2}R \\ -S^\dagger & P-Q & 0 & R & -\sqrt{2}Q & -\sqrt{\frac{3}{2}}S \\ R^\dagger & 0 & P-Q & S & \sqrt{\frac{3}{2}}S^\dagger & -\sqrt{2}Q \\ 0 & R^\dagger & S^\dagger & P+Q & -\sqrt{2}R^\dagger & \frac{1}{\sqrt{2}}S \\ -\frac{1}{\sqrt{2}}S & -\sqrt{2}Q^\dagger & \sqrt{\frac{3}{2}}S & -\sqrt{2}R & P+\Delta_{SO} & 0 \\ -\sqrt{2}R^\dagger & \sqrt{\frac{3}{2}}S & -\sqrt{2}Q^\dagger & \frac{1}{\sqrt{2}}S & 0 & P+\Delta_{SO} \end{pmatrix}.$$

The corresponding matrix elements for [001] growth direction are given in Refs. [92, 93] as,

$$\begin{aligned} P &= \gamma_1(k_x^2 + k_y^2 + k_z^2), \\ Q &= \gamma_2(k_x^2 + k_y^2 - 2k_z^2), \\ R &= [-\sqrt{3}\gamma_2(k_x^2 - k_y^2) + i2\sqrt{3}\gamma_3 k_x k_y], \\ S &= [i2\sqrt{3}(k_x - ik_y)k_z], \end{aligned} \tag{2.31}$$

where γ_i are known as the Luttinger parameters which are obtained from the experiments or from the first principle calculations and Δ_{SO} is the split-off band energy (see Fig. 2.1).

2.3.2 8-band Hamiltonian

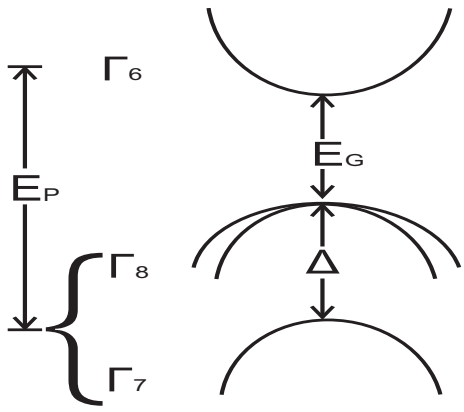

Figure 2.2: Schematic representation of the conduction and the valence band states.

The extended Kane Hamiltonian for an 8-band model [88, 89] is given by

$$H^8_{KL} = \begin{pmatrix} E_{7-} & 0 & -\frac{1}{\sqrt{2}}P^+ & \sqrt{\frac{2}{3}}P^z & \frac{1}{\sqrt{6}}P^- & 0 & \sqrt{\frac{1}{3}}P^z & \sqrt{\frac{1}{3}}P^- \\ 0 & E_{7-} & 0 & -\frac{1}{\sqrt{6}}P^+ & \sqrt{\frac{2}{3}}P^z & \frac{1}{\sqrt{2}}P^- & \sqrt{\frac{1}{3}}P^+ & -\sqrt{\frac{1}{3}}P^z \\ -\frac{1}{\sqrt{2}}P^- & 0 & E^H_{8+} & B & C & 0 & \frac{1}{\sqrt{2}}B_\Delta & \sqrt{2}C_\Delta \\ \sqrt{\frac{2}{3}}P^z & -\frac{1}{\sqrt{6}}P^- & B^\dagger & E^L_{8+} & 0 & C & -\sqrt{2}A_\Delta & -\sqrt{\frac{3}{2}}B_\Delta \\ \frac{1}{\sqrt{6}}P^+ & \sqrt{\frac{2}{3}}P^z & C^\dagger & 0 & E^L_{8+} & -B & -\sqrt{\frac{3}{2}}B^\dagger_\Delta & \sqrt{2}A_\Delta \\ 0 & \frac{1}{\sqrt{2}}P^+ & 0 & C^\dagger & -B^\dagger & E^H_{8+} & -\sqrt{2}C^\dagger_\Delta & \frac{1}{\sqrt{2}}B^\dagger_\Delta \\ \sqrt{\frac{1}{3}}P^z & \frac{1}{\sqrt{3}}P^- & \frac{1}{\sqrt{2}}B^\dagger_\Delta & -\sqrt{2}A^\dagger_\Delta & -\sqrt{\frac{3}{2}}B_\Delta & -\sqrt{2}C_\Delta & E_{7+} & 0 \\ \sqrt{\frac{1}{3}}P^+ & -\frac{1}{\sqrt{3}}P^z & \sqrt{2}C^\dagger_\Delta & -\sqrt{\frac{3}{2}}B^\dagger_\Delta & \sqrt{2}A^\dagger_\Delta & \frac{1}{\sqrt{2}}B_\Delta & 0 & E_{7+} \end{pmatrix}$$

where the terms with operators B and C give the interaction between the various valence band states of the same and the opposite spin respectively and terms with the P operator give the interaction between the valence and the conduction band states.

$$\begin{aligned}
E^H_{7-} &= E_g + \frac{\hbar^2}{2m_0}\{(k_x^2 + k_y^2 + k_z^2)\}, \\
E^H_{8+} &= 0 - \frac{\hbar^2}{2m_0}\{[(k_x^2 + k_y^2)(\tilde{\gamma}_1 + \tilde{\gamma}_2)] + (\tilde{\gamma}_1 - 2\tilde{\gamma}_2)k_z^2\}, \\
E^L_{8+} &= 0 - \frac{\hbar^2}{2m_0}\{[(k_x^2 + k_y^2)(\tilde{\gamma}_1 - \tilde{\gamma}_2)] + (\tilde{\gamma}_1 + 2\tilde{\gamma}_2)k_z^2\}, \\
C &= \frac{\hbar^2}{2m_0}\{\sqrt{3}[\tilde{\gamma}_2(k_x^2 - k_y^2) - 2i\tilde{\gamma}_3 k_x k_y]\}, \\
C_\Delta &= \frac{\hbar^2}{2m_0}\{\sqrt{3}[\tilde{\gamma}_{\Delta 2}(k_x^2 - k_y^2) - 2i\tilde{\gamma}_{\Delta 3} k_x k_y]\}, \\
B &= \frac{\hbar^2}{2m_0}\{2\sqrt{3}[\tilde{\gamma}_3 k_z(k_x - ik_y)]\}, \\
B_\Delta &= \frac{\hbar^2}{2m_0}\{2\sqrt{3}[\tilde{\gamma}_{\Delta 3} k_z(k_x - ik_y)]\}, \\
E^H_{7+} &= \Delta_{SO} - \frac{\hbar^2}{2m_0}\{\tilde{\gamma}_{\Delta 1}(k_x^2 + k_y^2 + k_z^2)\}, \\
A &= \tilde{\gamma}_2[2k_z^2 - (k_x^2 + k_y^2)], \\
A_\Delta &= \tilde{\gamma}_{\Delta 2}[2k_z^2 - (k_x^2 + k_y^2)], \\
P^\pm &= P(k_x \pm ik_y), \\
P^z &= Pk_z, \\
P &= \frac{\hbar}{m_0}\langle S|p_x|iX\rangle, \\
E_P &= (\frac{2m_0}{\hbar^2})P^2,
\end{aligned} \tag{2.32}$$

where where $\tilde{\gamma}_j$ are the Luttinger-like parameters and
$P = \frac{\hbar}{m_e}\langle S|p_x|X\rangle = \frac{\hbar}{m_e}\langle S|p_y|Y\rangle = \frac{\hbar}{m_e}\langle S|p_z|Z\rangle$
are the inter-band matrix elements between the conduction band (Γ_6) and the valence bands (Γ_8 and Γ_7) (see Fig. 2.2).

In order to describe simultaneously the conduction band Γ_6 and the valence bands Γ_8 and Γ_7 in an 8×8 Hamiltonian H^8_{KL} one has to introduce the Luttinger-like parameters $\tilde{\gamma}_j$ as a correction to the Luttinger parameters γ_j. This modification is a result of the Löwdin perturbation which should be employed when the 8-band model is modified to the 6-band **k.p** theory. The essential parameter in this procedure is the energy of the unperturbed states, whose value depends on the range of energies of interest. In the literature, in essence two sets of relations can be found. Pidgeon and Brown [88] used the following relations

$$\begin{aligned}\tilde{\gamma}_1 &= \gamma_1 - \frac{E_P}{3E_G},\\ \tilde{\gamma}_j &= \gamma_j - \frac{E_P}{6E_G}, \quad j = 2,3,\end{aligned} \tag{2.33}$$

which were used both for the Γ_8 and Γ_7 bands. We will refer to these parameters as PB parameters. In papers by Bahder [89] and Pryor [90], the following relations were used

$$\begin{aligned}\tilde{\gamma}_1^{BP} &= \gamma_1 - \frac{E_P}{3(E_G + \Delta/3)},\\ \tilde{\gamma}_j^{BP} &= \gamma_j - \frac{E_P}{6(E_G + \Delta/3)}, \quad j = 2,3,\end{aligned} \tag{2.34}$$

where the energy $E_G + \Delta/3$ is the difference between the energy of the conduction band and the energy of the *center of gravity* of the valence band, as stated in Ref. [94] and will be referred to as BP parameters. Here E_G is the band gap, and Δ is the split-off energy and E_P is the Kane energy.

2.4 Envelope function approximation: the k.p method for nanostructures

The envelope function approximation (EFA) allows one to describe the electron and the hole states in the presence of the slowly varying fields that vary across the length scale of the lattice constant. These fields can be internal such as the fields of crystal defects, or external such as the applied magnetic field. Let us consider the following Schrödinger equation

$$\left[\frac{(-i\hbar\nabla + e\mathbf{A})^2}{2m_0} + V(\mathbf{r}) + \frac{\hbar}{4m_0^2c^2}(-i\hbar\nabla + e\mathbf{A})\cdot\boldsymbol{\sigma}\times(\nabla V) + V_0(\mathbf{r}) + \frac{g}{2}\mu_B\boldsymbol{\sigma}\cdot\mathbf{B}\right]\Psi(r) = E(\mathbf{k})\Psi(\mathbf{r}), \tag{2.35}$$

which is similar to Eq.(2.1) with a microscopic lattice-periodic potential $V(\mathbf{r})$, an additional slowly varying potential $V_0(\mathbf{r})$, and a vector potential $\mathbf{A} = \mathbf{A}(\mathbf{r})$, which gives rise to a magnetic field $\mathbf{B} = \nabla \times \mathbf{A}$. The fifth term in the left side of the equation is the Zeeman term where $\mu_B = \frac{e\hbar}{2m_0}$ is the Bohr magneton and $g = 2$ is the g-factor of a free electron.

We expand the wave function $\Psi(\mathbf{r})$ in terms of the band-edge Bloch functions $u_{l'\mathbf{0}}(\mathbf{r}) \equiv \langle \mathbf{r}|l'\mathbf{0}\rangle$ times the spin states $|\sigma'\rangle$:

$$\Psi(\mathbf{r}) = \sum_{l',\sigma'} \psi_{l'\sigma'}(\mathbf{r}) u_{l'\mathbf{0}}(\mathbf{r})|\sigma'\rangle. \tag{2.36}$$

Here the position-dependent expansion coefficients $\psi_{l'\sigma'}(\mathbf{r})$ modulate the quickly oscillating Bloch functions $u_{l'\mathbf{0}}(\mathbf{r})$. As this modulation is slowly varying on the length scale of the lattice constant, the expansion coefficients $\psi_{l'\sigma'}(\mathbf{r})$ are called *envelope functions* [95, 96]. We insert Eq.(2.36) into Eq.(2.35), multiply from left by $\langle\sigma|u^*_{l\mathbf{0}}(\mathbf{r})$, and integrate over the one unit cell of the lattice. If $V(\mathbf{r})$, $\mathbf{A}(\mathbf{r})$, and $\psi_{l'\sigma'}(\mathbf{r})$ are slowly varying within one unit cell, we can take them out of the integral as constant factors. We then obtain

$$\sum_{l',\sigma'}\left\{\left[E_{l'}(0) + \frac{(-i\hbar\nabla + e\mathbf{A})^2}{2m_0} + V_0(\mathbf{r})\right]\delta_{ll'}\delta_{\sigma\sigma'} + \frac{1}{m_0}(-i\hbar\nabla + e\mathbf{A})\cdot P^{ll'}_{\sigma\sigma'} + \Delta^{ll'}_{\sigma\sigma'} + \frac{g}{2}\mu_B\sigma\cdot B\delta_{ll'}\right]\psi_{l'\sigma'}(\mathbf{r}) = E\psi_{l\sigma}(\mathbf{r}), \tag{2.37}$$

where

$$P^{ll'}_{\sigma\sigma'} = \langle l\sigma|\boldsymbol{\Pi}|l'\sigma'\rangle, \tag{2.38}$$

and

$$\Delta^{ll'}_{\sigma\sigma'} = \frac{\hbar}{4m_0^2c^2}\langle l\sigma|[\mathbf{p}\cdot(\boldsymbol{\sigma}\times\nabla V)]|l'\sigma'\rangle. \tag{2.39}$$

This is the EFA Hamiltonian (Eq.(2.37)) and it is a system of coupled differential equations, the eigenfunctions of which are the multicomponent envelope functions or spinors $\Psi(\mathbf{r}) = \psi_{l'\sigma'}(\mathbf{r})$. By applying the perturbation theory we see that this equation has close similarity to the **k.p** Hamiltonian in Eq.(2.10). Thus it is often argued that the EFA Hamiltonian can be obtained from the **k.p** Hamiltonian by setting $\mathbf{k} = -i\nabla + (e/\hbar)\mathbf{A}$.

This method can be applied to a freestanding nanowire where the potential outside the nanowire can be taken as ∞, as the energy of the work function is very large when compared to the energy of an electron in this system. The total Hamiltonian ($\mathbb{H}$) for a freestanding nanowire of radius R can be written as a sum of the Kohn-Luttinger Hamiltonian H_{KL} and the potential V,

$$\mathbb{H} = H_{KL} + V. \tag{2.40}$$

where

$$V = \begin{cases} 0 & \text{if } \rho < R \\ \infty & \text{if } \rho > R \end{cases}$$

In case of the nanowires (in the absence of a magnetic field) grown in [001] crystallographic direction that are discussed in this thesis, we can apply the EFA by replacing k_α with $-i\frac{\partial}{\partial\alpha}$ where $\alpha \in x, y, z$.

In cylindrical coordinates it is convenient to use $k_+ = k_x + ik_y$ and $k_- = k_x - ik_y$ instead of k_x and k_y such that

$$k_\pm = -ie^{\pm i\varphi}\left(\frac{\partial}{\partial\rho} \pm \frac{i}{\rho}\frac{\partial}{\partial\varphi}\right). \tag{2.41}$$

In the EFA, bulk band parameters are used which vary discontinuously at the interfaces. Thus, the position-dependent band edges act like effective step-like potentials for electrons and holes. The EFA is valid in the materials on either side of the interface but not at the interface. To overcome this difficulty proper boundary conditions have to be introduced to connect solutions over the interface and ensure the continuity of probability flux. Several authors have discussed the validity of EFA and the boundary conditions required in the presence of abrupt interfaces [98, 99, 101, 102, 103, 104, 105, 106]. Boundary conditions that are proposed include ensuring the hermiticity of EFA Hamiltonian operator over the interface [106] and using methods based on the microscopic derivations of the EFA approximation [98, 99, 101, 102].

In this thesis we study core-shell nanowires where the step-like position dependence of the band parameters implies that the pre-factors of differential operators vary discontinuously. To overcome this difficulty we have to use matching conditions at the interfaces for the envelope functions and their first derivatives. This will ensure the hermiticity of the kinetic energy operator and guarantee the continuity of probability flux at the interface. Therefore, we have used the following Hermitian formalism which is popularly used in literature [106, 107, 108, 109, 110, 134].

$$Ak_\alpha k_\beta \longrightarrow \frac{1}{2}[k_\alpha A k_\beta + k_\beta A k_\alpha] \quad \alpha, \beta = x, y, z, \tag{2.42}$$

where $k_\alpha = -i(\frac{\partial}{\partial \alpha})$ are the kinetic operators and A is some position dependent parameter such as the Luttinger parameter (γ_i).

This Hermitian formalism has been successfully used to study various heterostructures [103, 110, 134] and hence we will use this method in our thesis.

Applying the symmetrized form to the matrix elements in Eqs. (2.32) we get,

$$\begin{aligned}
E^H_{7-} &= E_g + \frac{\hbar^2}{2}\{\frac{1}{2}[k_+\frac{1}{m_0}k_- + k_-\frac{1}{m_0}k_+] + k_z\frac{1}{m_0}k_z\},\\
E^H_{8+} &= 0 - \frac{\hbar^2}{2m_0}\{\frac{1}{2}[k_+(\gamma_1+\gamma_2)k_- + k_-(\gamma_1+\gamma_2)k_+] + k_z(\gamma_1-2\gamma_2)k_z\},\\
E^L_{8+} &= 0 - \frac{\hbar^2}{2m_0}\{\frac{1}{2}[k_+(\gamma_1-\gamma_2)k_- + k_-(\gamma_1-\gamma_2)k_+] + k_z(\gamma_1+2\gamma_2)k_z\},
\end{aligned}$$

$$
\begin{aligned}
C &= \frac{\hbar^2}{2m_0}\{\sqrt{3}[k_-\bar{\gamma}k_- + k_+\mu k_+]\},\\
C_\Delta &= \frac{\hbar^2}{2m_0}\{\sqrt{3}[k_-\bar{\gamma_\Delta}k_- + k_+\mu_\Delta k_+]\},\\
B &= \frac{\hbar^2}{2m_0}\{\sqrt{3}[k_-\gamma_3 k_z + k_z\gamma_3 k_-]\},\\
B_\Delta &= \frac{\hbar^2}{2m_0}\{\sqrt{3}[k_-\gamma_{\Delta 3} k_z + k_z\gamma_{\Delta 3} k_-]\},\\
E^H_{7+} &= \Delta_{SO} - \frac{\hbar^2}{2m_0}\{\frac{1}{2}(k_+\gamma_1 k_- + k_-\gamma_1 k_+) + k_z^2\},\\
A &= \frac{\hbar^2}{2m_0}[2\gamma_2 k_z^2 - (\frac{1}{2}(k_+\gamma_2 k_- + k_-\gamma_2 k_+))],\\
A_\Delta &= \frac{\hbar^2}{2m_0}[2\gamma_{\Delta 2} k_z^2 - (\frac{1}{2}(k_+\gamma_{\Delta 2} k_- + k_-\gamma_{\Delta 2} k_+))],
\end{aligned}
\tag{2.43}
$$

where

$k_\pm = k_x \pm ik_y$,
$\bar{\gamma} = (\gamma_3 + \gamma_2)/2, \mu = (\gamma_2 - \gamma_3)/2$,
$\bar{\gamma_\Delta} = (\gamma_{\Delta 3} + \gamma_{\Delta 2})/2, \mu_\Delta = (\gamma_{\Delta 2} - \gamma_{\Delta 3})/2$.

2.4.1 k.p Hamiltonian with magnetic field

Appropriate modifications have to be made to the Hamiltonian to include the effect of the magnetic field. The Hamiltonian can be modified by changing the wave vector. In case of nanowires without magnetic field the wave vector can be written as,

$$k_\alpha = \frac{1}{i}\frac{\partial}{\partial x_\alpha}, \tag{2.44}$$

where the α are x, y and z.

And as, $k_\pm = k_x + ik_y$,

$$\Rightarrow k^0_\pm = -ie^{\pm i\varphi}(\frac{\partial}{\partial\rho} \pm \frac{i}{\rho}\frac{\partial}{\partial\varphi}), \tag{2.45}$$

in cylindrical coordinates.

With the application of magnetic field the wave vector is modified as given below,

$$k_\alpha = \frac{1}{i}\frac{\partial}{\partial x_\alpha} + \frac{e}{\hbar}A_\alpha. \tag{2.46}$$

In the present thesis we consider the magnetic field is along the wire, in the z-direction. Accordingly, we can choose the symmetric gauge in cylindrical coordinates, $\mathbf{A}$=(0,A_φ,0) and A_φ=$\frac{\rho B}{2}$. Now,

$$k_\pm = e^{\pm i\varphi}[-i(\frac{\partial}{\partial\rho} \pm \frac{i}{\rho}\frac{\partial}{\partial\varphi}) \pm i\frac{e}{\hbar}A_\varphi], \tag{2.47}$$

$$k_\pm = k_\pm^0 + k_\pm^B, \tag{2.48}$$

where $k_\pm^B = \pm i\frac{\rho}{2l_B^2}e^{\pm i\varphi}$ with $l_B = (\frac{\hbar}{eB_z})^{\frac{1}{2}}$ (magnetic length).

Thus the total Hamiltonian is given by [96]

$$H_{k_\pm}^B = H_{LK}(k_\pm^0) + H_{LK}(k_\pm^B) + g\mu_B\kappa B, \tag{2.49}$$

where $H_{KL}(k_\pm^0)$ is the Kohn-Luttinger Hamiltonian without magnetic field (see subsection 2.3.2), $H_{KL}(k_\pm^B)$ is the KL Hamiltonian with magnetic field and $g\mu_B\kappa B$ gives the zeeman splitting term (see Appendix C for complete matrix elements). In the zeeman term, $\kappa = \pm$ 1 for electrons, $\kappa = \pm$ 3 for heavy holes, $\kappa = \pm$ 1 for light holes, $\kappa = \pm$ 2 for split-off band and $\pm\sqrt{2}$ for A the coupling term between split-off band and light holes (see Eq. (C.6)).

Landé's g factor κ for conduction band [111]:

$$g_{CB} = 2 - \frac{2}{3}\frac{E_G\Delta}{E_G(E_G+\Delta)}, \tag{2.50}$$

and g for valence band [113, 114]:

$$g_{VB} = \gamma_3 + \frac{2}{3}\gamma_2 - \frac{1}{3}\gamma_1 - \frac{2}{3}. \tag{2.51}$$

In the present thesis we consider zincblende nanowires with diameters $D \geq 30$ $\mathring{A}$ where there is no direct to indirect transition[112] occurring. Hence there is no need to consider the satellite valleys and thus the **k.p** models defined in this chapter are sufficient to study these nanowires. In the following chapters we will use different **k.p** models defined in this chapter to study the electronic and optical properties of these nanowires.

Chapter 3

Electronic and optical properties of wide gap semiconductor nanowires

In this chapter we study the electronic and optical properties of GaAs /$Al_xGa_{1-x}As$ core-shell nanowires*. Electronic properties of core-shell structures have been studied by various authors [92, 93]. It has been claimed that for core-shell nanowires composed of lattice-matched materials (e.g. GaAs and AlAs), the electronic structure is trivial [38]. However, in this chapter it will be shown that the electronic structure of unstrained core-shell wires can differ significantly from the corresponding single material wires.

*V. V. Ravi Kishore, B. Partoens, and F. M. Peeters: Electronic structure and optical absorption of GaAs/$Al_xGa_{1-x}As$ and $Al_xGa_{1-x}As$/GaAs core-shell nanowires, *Phys. Rev. B* **82**, 235425 (2010). Also selected for the December 20, 2010 issue of Virtual Journal of Nanoscale Science and Technology.

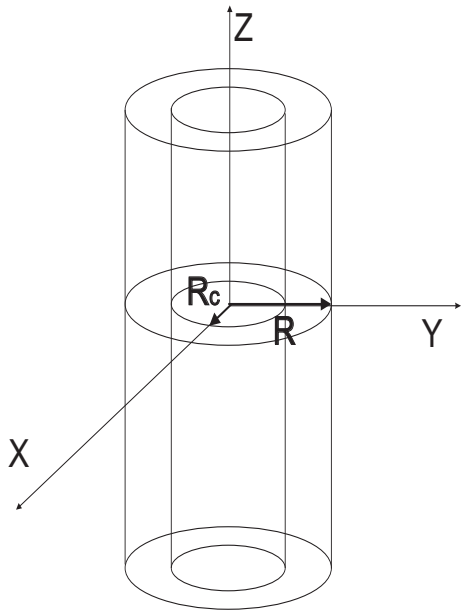

Figure 3.1: Schematic diagram of a core-shell nanowire with core radius R_c and total radius R.

In this chapter, we consider an infinitely long cylindrical core-shell nanowire as schematically shown in Fig. 3.1 and study its electronic properties using the multi-band **k.p** method. We consider wires grown in the [001] direction consisting of GaAs and $Al_xGa_{1-x}As$, taking one material as the core and the other as the shell material. Here we consider very thin nanowires of diameter d=3-12 nm. As in GaAs the Bohr radius is $a_B \simeq 11.5$ nm and the effective Rydberg energy $E_{Ry} \simeq 5.0$ meV, quantum confinement effects are very important in these thin nanowires.

This chapter is organized as follows. In the next section we give the theoretical description of our model. In Sec. III we present our results for the single particle states, starting with a discussion of GaAs and how spin-orbit interaction modifies the valence band-energy dispersion, spinor distribution and density. This is followed by results on $Al_xGa_{1-x}As$ free standing nanowires. And finally we present our results for the core-shell nanowire with GaAs as core and $Al_xGa_{1-x}As$ as shell and vice versa. Our results are summarized in Sec. IV.

In this chapter for the conduction band we consider a parabolic energy spectrum with effective mass m^*. The dispersion of the conduction band is

given by

$$H_{el} = \frac{\hbar^2}{2m^*}(k_x^2 + k_y^2 + k_z^2). \tag{3.1}$$

For the valence band we use the 6×6 Kohn-Luttinger (KL) Hamiltonian [78, 81, 82] which includes the spin-orbit interaction and we do not make any further approximations such as the axial or spherical approximation [115].

This Kohn-Luttinger(KL) Hamiltonian is given by

$$H_{KL} = -\begin{pmatrix} P+Q & -S & R & 0 & -\frac{1}{\sqrt{2}}S & \sqrt{2}R \\ -S^\dagger & P-Q & 0 & R & -\sqrt{2}Q & \sqrt{\frac{3}{2}}S \\ R^\dagger & 0 & P-Q & S & \sqrt{\frac{3}{2}}S^\dagger & \sqrt{2}Q \\ 0 & R^\dagger & S^\dagger & P+Q & -\sqrt{2}R^\dagger & -\frac{1}{\sqrt{2}}S^\dagger \\ -\frac{1}{\sqrt{2}}S^\dagger & -\sqrt{2}Q^\dagger & \sqrt{\frac{3}{2}}S & -\sqrt{2}R & P+\Delta_{SO} & 0 \\ \sqrt{2}R^\dagger & \sqrt{\frac{3}{2}}S^\dagger & \sqrt{2}Q^\dagger & -\frac{1}{\sqrt{2}}S & 0 & P+\Delta_{SO} \end{pmatrix} \tag{3.2}$$

and its matrix elements for the [001] growth direction are

$$P = \frac{\hbar^2}{2m_0}\gamma_1\{k_x^2 + k_y^2 + k_z^2\}, \tag{3.3}$$

$$Q = \frac{\hbar^2}{2m_0}\gamma_2\{k_x^2 + k_y^2 - 2k_z^2\}, \tag{3.4}$$

$$R = \frac{\hbar^2}{2m_0}\{\sqrt{3}[-\gamma_2(k_x^2 - k_y^2) + 2i\gamma_3 k_x k_y]\}, \tag{3.5}$$

$$S = \frac{\hbar^2}{2m_0}\{2\sqrt{3}[\gamma_3(k_x - ik_y)k_z]\}, \tag{3.6}$$

with

$$k_\alpha = -i(\frac{\partial}{\partial\alpha}), \qquad \alpha = (x, y, z). \tag{3.7}$$

For our core-shell heterostructure the effective electron mass and Luttinger parameters can be written as

$$m^* = m_s^* + (m_c^* - m_s^*)[1 - \Theta(\rho - R_c)], \tag{3.8}$$

$$\gamma = \gamma_s + (\gamma_c - \gamma_s)[1 - \Theta(\rho - R_c)], \tag{3.9}$$

with m_s^* and γ_s the values in the shell and m_c^* and γ_c the values in the core. Θ is the heavy side step function. R is the radius of the total wire and R_c

the radius of the core part. Applying the effective mass approach leads to the following electron Hamiltonian

$$H_{el} = \frac{\hbar^2}{2}\{\frac{1}{2}[k_+\frac{1}{m^*}k_- + k_-\frac{1}{m^*}k_+] + k_z\frac{1}{m^*}k_z\}. \tag{3.10}$$

The matrix elements of the KL Hamiltonian for our cylindrical core-shell heterostructure are given by,

$$P + Q = \frac{\hbar^2}{2m_0}\{\frac{1}{2}[k_+(\gamma_1+\gamma_2)k_- + k_-(\gamma_1+\gamma_2)k_+] + k_z(\gamma_1 - 2\gamma_2)k_z\}, \tag{3.11}$$

$$P - Q = \frac{\hbar^2}{2m_0}\{\frac{1}{2}[k_+(\gamma_1-\gamma_2)k_- + k_-(\gamma_1-\gamma_2)k_+] + k_z(\gamma_1 + 2\gamma_2)k_z\}, \tag{3.12}$$

$$R = \frac{-\hbar^2}{2m_0}\{\sqrt{3}[k_-\bar{\gamma}k_- + k_+\mu k_+]\}, \tag{3.13}$$

$$S = \frac{\hbar^2}{2m_0}\{\sqrt{3}[k_-\gamma_3 k_z + k_z\gamma_3 k_-]\}, \tag{3.14}$$

where

$$k_\pm = k_x \pm ik_y = -ie^{\pm i\varphi}(\frac{\partial}{\partial\rho} \pm \frac{i}{\rho}\frac{\partial}{\partial\varphi}), \tag{3.15}$$

$$k_\pm(\gamma_s + (\gamma_c - \gamma_s)[1 - \Theta(\rho - R_c)]) = i(\gamma_c - \gamma_s)\delta(\rho - R_c)e^{\pm i\varphi}, \tag{3.16}$$

and $\bar{\gamma} = (\gamma_3 + \gamma_2)/2$ and $\mu = (\gamma_2 - \gamma_3)/2$.

We assume that in our case the charge is totally localized in the nanowire and it is zero outside. All the band parameters used in this chapter are taken from the work of Vurgaftman[116] and are given in Table 3.1.

	GaAs	$Al_xGa_{1-x}As$
γ_1	6.98	$(0.4398 + 0.217x)/(0.0630 + 0.88x + 0.024x^2)$
γ_2	2.06	$(0.2596 + 0.0269x)/(0.1260 + 1.76x + 0.048x^2)$
γ_3	2.93	$(0.815 + 0.0305x)/(0.2784 + 0.296x + 0.0308x^2)$
m_{lh}	$0.0901m_0$	$0.0901m_0 + (0.0951m_0)x$
m_{hh}	$0.3497m_0$	$0.3497m_0 + (0.122m_0)x$
m^*	$0.067m_0$	$0.067m_0 + (0.083m_0)x$
Δ_{so}	-341 meV	$-341 + 61x$ meV
E_g^Γ	1519 meV	$1519 + 1707x - 1437x^2 + 1310x^3$ meV

Table 3.1: Band parameters of GaAs and $Al_xGa_{1-x}As$ (m_0 is the bare electron mass).

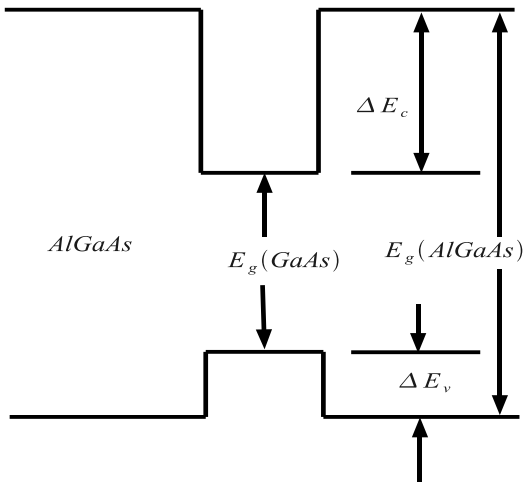

Figure 3.2: Schematic diagram of bandalignment in GaAs/AlGaAs core-shell nanowire.

The core-shell nanowire is a heterostructure and hence inclusion of band offset in the Hamiltonian is essential. We use the following band offset values, corresponding to the sign convention in Fig. 3.2, for the GaAs and $Al_xGa_{1-x}As$ heterostructure [117]: ΔE_v=570x meV and ΔE_c=870x meV. The envelope wave function for the conduction band is expanded in a basis

of eigenfunctions of a cylinder with radius R:

$$\Psi^{\sigma}_{el}(\rho,\phi,z,\sigma) = e^{ik_z}\sum_{m=-M}^{M}\sum_{l=1}^{L} C^{el}_{ml}\frac{e^{im\phi}}{\sqrt{2\pi}}\frac{\sqrt{2}}{RJ_{m+1}(\alpha_{ml})}J_m(\alpha_{ml}\frac{\rho}{R})\eta_{\sigma}, \tag{3.17}$$

where J_m is the Bessel function of the first kind and α_{ml} is the lth zero of the corresponding Bessel function J_m ($m = 0, \pm1, \pm2, \pm3, .. \pm M, l = 1, 2, 3..L$) and R is the radius of the nanowire. Here we have used cylindrical coordinates (ρ, ϕ, z). The coefficients C^{el}_{ml} are determined by diagonalizing the electron Hamiltonian. Only for pure single material nanowires, the chosen basis functions are eigenfunctions of the electron Hamiltonian. Eigen energies form a set of sub-bands numbered by pairs (m, l) and are four fold degenerate with respect to the spin degree of freedom (σ=$\pm$) and the angular momentum ($\pm m$). In Eq.(3.17), the symbol η_{σ} is the spin part of the electron wave function. For the valence band, for each spinor component, we assumed the following trial wave function:

$$\Psi^{\nu}_{h}(\rho,\phi,z,\nu) = e^{ik_z}\sum_{m=-M}^{M}\sum_{l=1}^{L} C^{\nu}_{ml}\frac{e^{im\phi}}{\sqrt{2\pi}}\frac{\sqrt{2}}{RJ_{m+1}(\alpha_{ml})}J_m(\alpha_{ml}\frac{\rho}{R}), \tag{3.18}$$

where C^{ν}_{ml} are determined by diagonalizing the 6×6 Kohn-Luttinger Hamiltonian. We limited the infinite sum to typically M=4 and L=4.

According to the Fermi Golden rule [118] the absorption power of photons with energy E=$\hbar\omega$ is given by

$$P = \frac{\pi e^2}{2\omega}\Sigma_{i,f}(F_i - F_f)|\langle f|\boldsymbol{p}.\boldsymbol{A}|i\rangle|^2\delta[E_f - (E_i + \hbar\omega)], \tag{3.19}$$

where $F_{i/f}$ is the Fermi-Dirac distribution function with initial (i) and final (f) electronic states, respectively. The initial state corresponds to the valence band state $\langle \mathbf{r}|i\rangle = \Sigma_{\mu}\Psi^{\nu}_{h}(\mathbf{r},\mu)\langle \mathbf{r}|\mu\rangle$ and the final state corresponds to the conduction band state $\langle \mathbf{r}|f\rangle = \Psi^{\sigma}_{el}(\mathbf{r})\langle \mathbf{r}|S\rangle$, where $\langle \mathbf{r}|\mu\rangle$ and $\langle \mathbf{r}|S\rangle$ are Bloch states at the Γ point of the Brillouin zone.

Thus from Eq. 3.19 we can see that the absorption power is proportional to $|\langle f|\boldsymbol{p}.\boldsymbol{A}|i\rangle|^2$ which corresponds to the various transitions between the conduction and the valence band states. The vector potential $\boldsymbol{A}$ can be replaced by $A\boldsymbol{e}$ where $\boldsymbol{e}$ is a unit vector parallel to $\boldsymbol{A}$. The amplitude of $\boldsymbol{A}$ can also be written in terms of the amplitude of the incident electric field $E(\boldsymbol{q},\omega)$ which is given as

$$A = -\frac{E}{2q}\exp i(\boldsymbol{q}.\boldsymbol{r} - \omega t) + c.c. \quad , \tag{3.20}$$

where $\mathbf{q}$ is the wavevector, q is the amplitude of wavevector and ω is the frequency.

The Bloch functions (see Eq. (2.2)) for electrons in conduction and the valence bands can be written as,

$$|c\rangle = u_{n_c \boldsymbol{k_c}}(\mathbf{r}) \exp\left[i\boldsymbol{k_c}.\boldsymbol{r}\right], \tag{3.21}$$
$$|v\rangle = u_{n_v \boldsymbol{k_v}}(\mathbf{r}) \exp\left[i\boldsymbol{k_v}.\boldsymbol{r}\right]. \tag{3.22}$$

Thus using vector potential $\boldsymbol{A} = A\boldsymbol{e}$ and Eq. (3.20), the integral $I = |\langle c|\boldsymbol{p}.\boldsymbol{A}|v\rangle|^2$ can be written as

$$\begin{aligned} I &= |\langle c|\boldsymbol{p}.\boldsymbol{A}|v\rangle|^2, \\ &= \frac{|E|^2}{4q^2}|\int u^*_{n_c \mathbf{k}\cdot\mathbf{c}}(\mathbf{r}) \exp\left[i(\mathbf{q}-\boldsymbol{k_c}).\mathbf{r}\right](\boldsymbol{e}.\boldsymbol{p}) u_{n_v \boldsymbol{k_v}}(\mathbf{r}) \exp\left[i\boldsymbol{k_v}.\boldsymbol{r}\right]|^2 d\mathbf{r}, \\ &= \frac{|E|^2}{4q^2}|\int u^*_{n_c \mathbf{k}\cdot\mathbf{c}}(\mathbf{r})(\boldsymbol{e}.\boldsymbol{p}) u_{n_v \boldsymbol{k_v}}(\mathbf{r}) \exp\left[i(\mathbf{q}-\boldsymbol{k_c}+\boldsymbol{k_v}).\mathbf{r}\right]|^2 d\mathbf{r}. \end{aligned} \tag{3.23}$$

For small $\mathbf{q}$, integral I represents the probability of a direct transition ($\mathbf{k} = \boldsymbol{k_c} = \boldsymbol{k_v}$) between conduction and valence band states [118]. The integral $I \propto |\langle c|\boldsymbol{e}.\boldsymbol{p}|v\rangle|^2$ which is a measure of absorption is calculated using Eqs.(2.15), (3.17), (3.18) and (3.23) and the selection rules as follows:

$$\begin{aligned} I_{\sigma^+} \simeq &|\frac{2}{\sqrt{6}}\langle\Psi^{\sigma}_{el,\uparrow}|\Psi^{\nu}_{h,\frac{3}{2},-\frac{1}{2}}\rangle + \frac{2}{\sqrt{2}}\langle\Psi^{\sigma}_{el,\downarrow}|\Psi^{\nu}_{h,\frac{3}{2},-\frac{3}{2}}\rangle \\ &- \frac{2}{\sqrt{3}}\langle\Psi^{\sigma}_{el,\uparrow}|\Psi^{\nu}_{h,\frac{1}{2},-\frac{1}{2}}\rangle|^2, \end{aligned} \tag{3.24}$$

$$\begin{aligned} I_{\sigma^-} \simeq &|\frac{2}{\sqrt{2}}\langle\Psi^{\sigma}_{el,\uparrow}|\Psi^{\nu}_{h,\frac{3}{2},\frac{3}{2}}\rangle + \frac{2}{\sqrt{6}}\langle\Psi^{\sigma}_{el,\downarrow}|\Psi^{\nu}_{h,\frac{3}{2},\frac{1}{2}}\rangle \\ &+ \frac{2}{\sqrt{3}}\langle\Psi^{\sigma}_{el,\downarrow}|\Psi^{\nu}_{h,\frac{1}{2},\frac{1}{2}}\rangle|^2, \end{aligned} \tag{3.25}$$

for circular polarized light ($\Delta m_j = \pm 1$) and

$$\begin{aligned} I_{\pi} \simeq &|\sqrt{\frac{2}{3}}\langle\Psi^{\sigma}_{el,\downarrow}|\Psi^{\nu}_{h,\frac{3}{2},-\frac{1}{2}}\rangle + \sqrt{\frac{2}{3}}\langle\Psi^{\sigma}_{el,\uparrow}|\Psi^{\nu}_{h,\frac{3}{2},\frac{1}{2}}\rangle \\ &+ \sqrt{\frac{1}{3}}\langle\Psi^{\sigma}_{el,\uparrow}|\Psi^{\nu}_{h,\frac{1}{2},\frac{-1}{2}}\rangle + \sqrt{\frac{1}{3}}\langle\Psi^{\sigma}_{el,\downarrow}|\Psi^{\nu}_{h,\frac{1}{2},\frac{1}{2}}\rangle|^2, \end{aligned} \tag{3.26}$$

for linearly polarized light ($\Delta m_j = 0$).

We also define the degree of circular polarization as:

$$\Pi = \frac{I_{\sigma_+} - I_{\sigma_-}}{I_{\sigma_+} + I_{\sigma_-}}. \tag{3.27}$$

We follow the previous work of Redliński and Peeters[119], and calculate first the energy dispersion and spinor distributions for free standing pure GaAs and $Al_xGa_{1-x}As$ nanowires. In all figures we show also the contributions of the hole states $|\frac{3}{2},\frac{3}{2}\rangle$, $|\frac{3}{2},-\frac{3}{2}\rangle$, $|\frac{3}{2},\frac{1}{2}\rangle$ and $|\frac{3}{2},-\frac{1}{2}\rangle$. In addition the electron and hole densities and the absorption spectra for GaAs, $Al_xGa_{1-x}As$ and their core-shell nanowires are reported. The maximum of the valence band of GaAs is taken as the zero of energy in all the energy spectrum plots.

3.1 Single material nanowire

In Ref. [119] a camel back structure in the energy band structure was found for pure GaAs nanowires and they concluded that this was due to the heavy hole-light hole interaction. They reported that this camel back structure decreases with increasing radius of the nanowire.

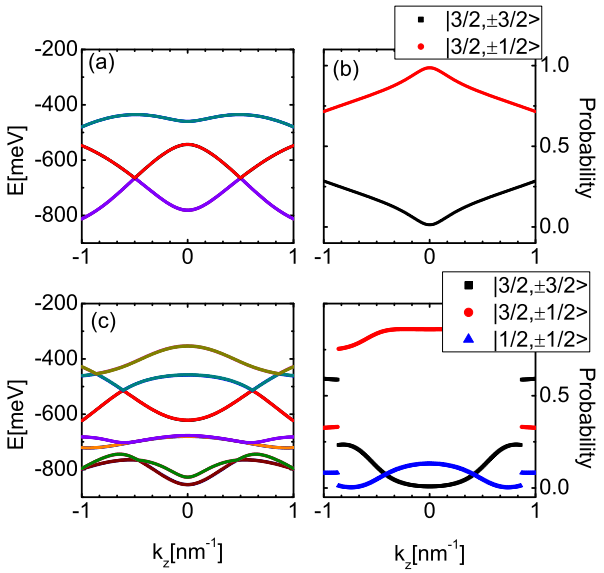

Figure 3.3: Valence band (left figures) and spinor distribution in the top valence band (right figures) of GaAs nanowire of R=1.5 nm with 4×4 KL Hamiltonian((a) and (b)) and 6×6 KL Hamiltonian ((c) and (d)).

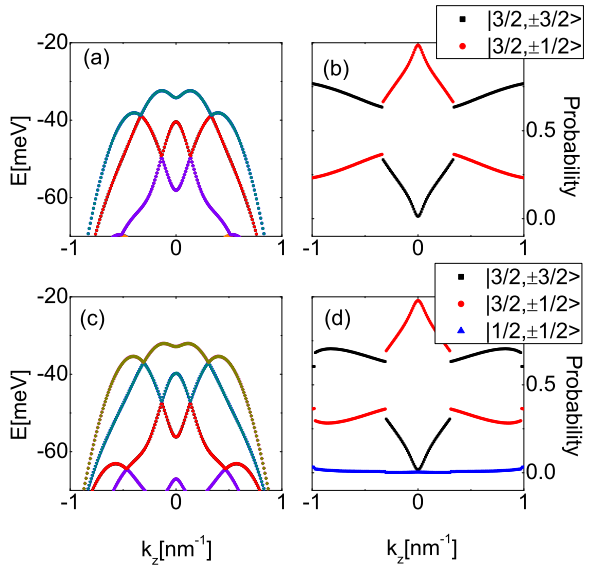

Figure 3.4: The same as Fig. 3.3 but now for a nanowire of radius R=5.5 nm

We extended those results with a special emphasis on the influence of the split-off band and the quantum confinement effects, i.e. we considered an ultra thin pure GaAs nanowire with R=1.5 nm. From Fig. 3.3(a) we find that the 4×4 KL Hamiltonian generates a camel back structure, which is absent in the results obtained from the 6×6 KL Hamiltonian (Fig. 3.3(c)). Figs. 3.3(b) and (d) show the corresponding spinor distributions. Note that the light hole contribution has a different behavior as function of k_z: in case of the result obtained with the 4×4 KL Hamiltonian, and where a camel back structure is observed, the contribution is peaked around k_z=0, while it is much more flat in the result obtained with the 6×6 KL Hamiltonian, where no camel back structure is found. A look at the different spinor contributions to the hole ground state tells us that the split-off band contribution for a nanowire with very small radius is not negligible. This is not the case for a nanowire of radius R=5.5 nm as shown in Fig. 3.4, where the 4×4 and 6×6 KL Hamiltonians lead to practically the same results with a clear camel back structure. Thus we may conclude that quantum confinement enhances strongly the split-off band contribution and that it can even destroy the camel back structure. From now on all results are obtained with the 6×6 KL Hamiltonian.

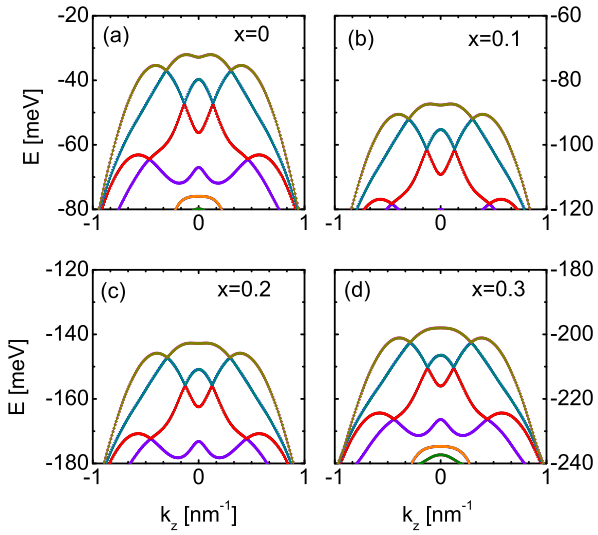

Figure 3.5: Valence band structure with x=0 (a), x=0.1 (b), x=0.2 (c) and x=0.3 (d) with R=5.5 nm $Al_xGa_{1-x}As$ nanowire in [001] growth direction.

Now we investigate the influence of alloying with Al on the camel back structure of the hole band. Fig. 3.5 shows the valence band structure for an $Al_xGa_{1-x}As$ nanowire with radius R=5.5 nm for different Al concentrations. Comparison with the result for the pure GaAs nanowire with the same radius (see Fig. 3.4(d)) learns that the camel back structure slowly vanishes with increasing x.

3.2 Core-shell nanowires

The camel back structure of the lowest valence band is a remarkable feature of the electronic structure in pure GaAs nanowires, and to a lesser extent in pure $Al_xGa_{1-x}As$ nanowires. Now we will investigate how this valence band structure is affected in core-shell nanowires. As shown above, the split-off band can mix strongly with the heavy and light hole bands for thin wires. Therefore, all shown results are obtained with the 6×6 KL Hamiltonian. We have investigated wires with different radii, but a representative example is the core-shell wire with a radius of R=10 nm (see Fig. 3.2).

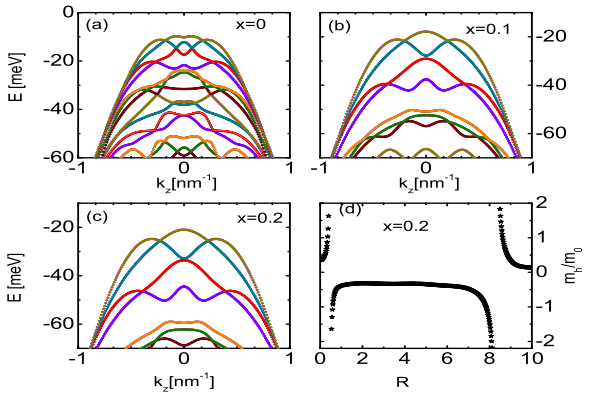

Figure 3.6: Valence band structure with x=0 (a), x=0.1 (b), x=0.2 (c) and effective hole mass at k_z=0 (d) for x=0.2 and R_c=1-10 nm and R=10 nm for a GaAs/$Al_xGa_{1-x}As$ nanowire in [001] growth direction.

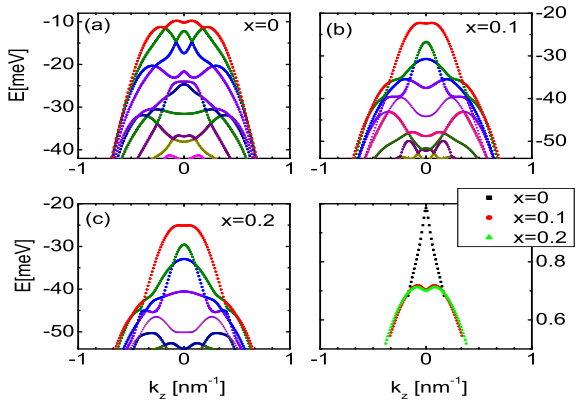

Figure 3.7: Valence band structure with x=0 (a), x=0.1 (b), x=0.2 (c) and light hole spinor distributions for the top hole band (d) with R_c=5 nm and R=10 nm $Al_xGa_{1-x}As$/GaAs nanowire in [001] growth direction.

Let us first consider a nanowire with a core of GaAs with radius R_c=5 nm, and an $Al_xGa_{1-x}As$ shell. Fig. 3.6(a) shows the top of the valence band around k_z=0 for x=0, 0.1 and 0.2. For x=0 a clear camel back structure is found, as this is of course a pure GaAs nanowire. However, when the Al concentration in the shell is increased, we find the remarkable result that

the camel-back structure disappears, even for x=0.1. We summarized the R_c dependence of the camel-back structure by calculating the effective hole mass (m_h) at k_z=0 which we obtained by fitting $E=-\hbar^2 k_z^2/2m_h$ around k_z=0. The results for x=0.2 and R=10 nm are plotted in Fig. 3.6(d). A negative mass corresponds to a camel-back structure which is found in the ranges 0 nm$< R_c <$ 0.6 nm and 8 nm$< R_c <$ 10 nm. The transition point between positive and negative effective mass corresponds to a flat band around k_z=0 where $|m_h|=\infty$.

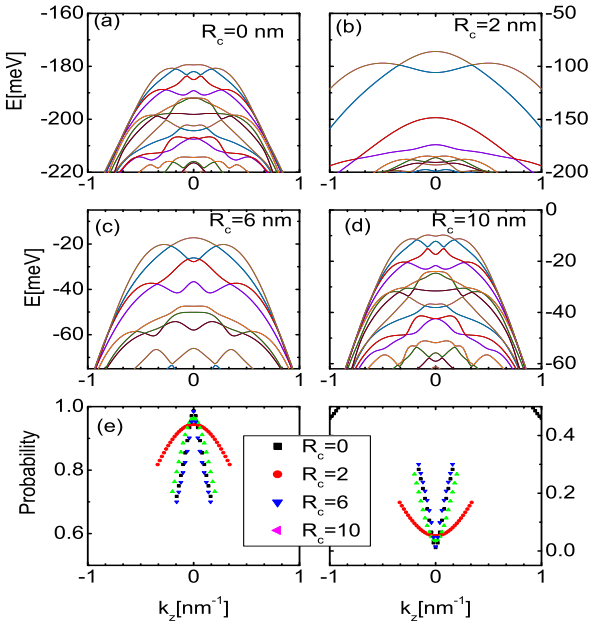

Figure 3.8: Valence band structure of GaAs/$Al_{0.3}Ga_{0.7}As$ nanowires with R_c=0 nm (a), R_c=2 nm (b), R_c=6 nm (c) R_c=10 nm and R=10 nm (d) and light hole (e), heavy hole (f) distribution of the top valence band with R=10 nm.

Similar results are shown in Figs. 3.7(a), (b) and (c) for nanowires with $Al_xGa_{1-x}As$ core and GaAs shell. The light hole distribution is given in Fig. 3.7(d). Notice now that also in this case the camel back structure disappears with increasing Al concentration. Furthermore we observe a local minima in the light-hole distribution around k_z=0 for x=0.1 and x=0.2.

It is also interesting to look at the influence of the core radius on these results. Let us again consider a nanowire with a GaAs core. The Al concentration of the $Al_xGa_{1-x}As$ shell is fixed to x=0.3. Fig. 3.8 shows the evolution of the top of the valence band for R_c=0, 2, 6 and 10 nm. Again we note that the camel back structure, which is present for R_c=0 nm and R_c=10 nm, immediately disappears in case of a core-shell structure. Also note that in Fig. 3.8(b) for R_c=2 nm the bands appear to be unevenly distributed in energy as compared to the other shown band structures. The reason is that for a $GaAs/Al_{0.3}Ga_{0.7}As$ nanowire the hole is more strongly confined within the core region for a core radius R_c=2 nm then for the other core radii, as will be shown in Sec. 3.4. Therefore, the spectrum resembles the spectrum of a thinner wire which has a smaller dispersion.

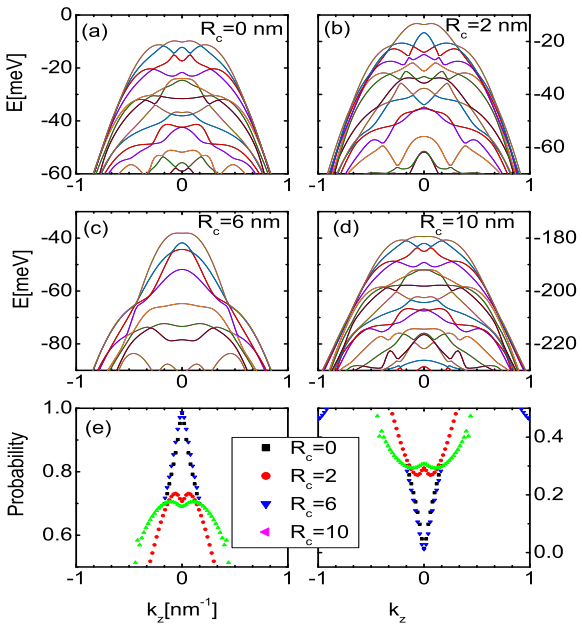

Figure 3.9: Valence band structure of $Al_{0.3}Ga_{0.7}As/GaAs$ nanowires with R_c=0 nm (a), R_c=2 nm (b), R_c=6 nm (c) R_c=10 nm (d) and light hole (e), heavy hole (f) distribution of the top valence band with R=10 nm.

If we interchange the core and the shell materials, thus $Al_xGa_{1-x}As$ in the core and GaAs in the shell, the camel back structure also disappears, however

not as abrupt as in the previous case, as shown in Fig. 3.9 for x=0.3. And again we see a maximum in the light hole distribution and a minimum in the heavy hole distribution when GaAs is in the core, and a minimum in the light hole distribution and a maximum in the heavy hole distribution when $Al_xGa_{1-x}As$ is in the core.

3.3 Optical absorption

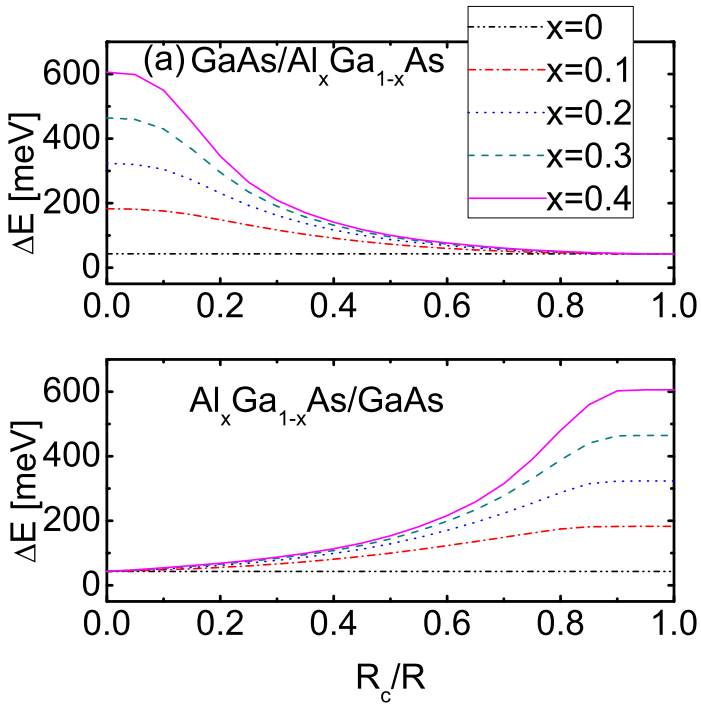

Figure 3.10: Quantum confinement induced energy shift ΔE=E_c + E_v in the electron (E_c) and hole (E_v) ground state for GaAs/$Al_xGa_{1-x}As$ (a) and $Al_xGa_{1-x}As$/GaAs (b) nanowires with R=10 nm in [001] growth direction for different x values.

Now that we have seen that the structure of the top of the valence band can change drastically in a core-shell nanowire in comparison to a single material wire, we will investigate its effect on the absorption spectrum. Again all shown results are for nanowires with a radius of R=10 nm.

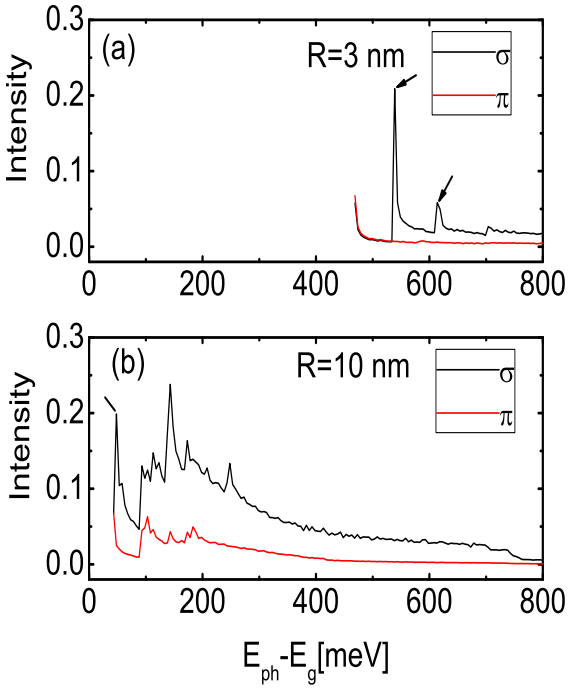

Figure 3.11: Absorption intensity (arbitrary units) for freestanding GaAs nanowire of radius R=3 nm (a) and R=10 nm (b) in [001] growth direction with 6×6 KL.

It is interesting to look at the effect of the radius of the wire on these absorption spectra, as shown in Figs. 3.11. For thin wires the confinement effect is clearly visible as the different absorption peaks are clearly observable, while in thicker wires the different peaks are not distinguishable any more, but they form a broad absorption band.

The onset of the absorption peak is given by the energy difference $\Delta E = E_c + E_v$, where E_c is the lowest energy of the conduction band, E_v is the highest valence band energy (note that E_g, the band gap of GaAs, is not included). This energy difference induced by quantum confinement is shown in Fig. 3.10(a) for GaAs in the core and in Fig. 3.10(b) for $Al_xGa_{1-x}As$ in the core for different Al concentrations, as function of the radius of the core R_c. As $Al_xGa_{1-x}As$ has a larger band gap than GaAs, this onset undergoes a blue-shift when more Al is present in the wire.

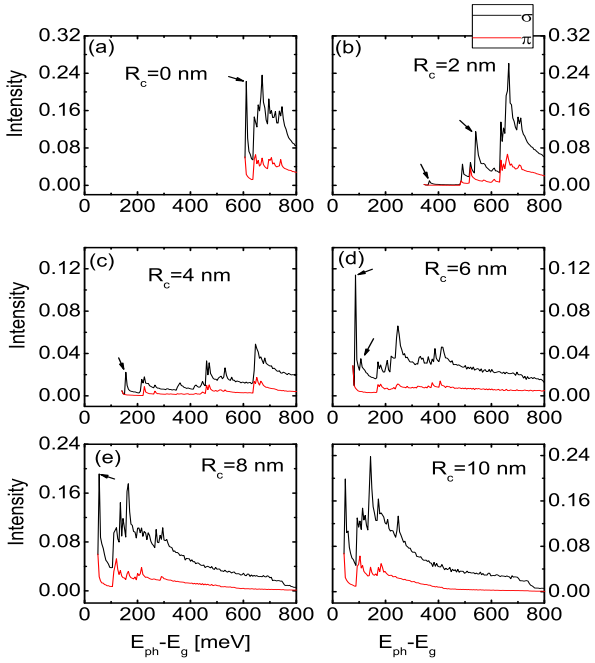

Figure 3.12: Absorption intensity (arbitrary units) for GaAs/$Al_{0.4}Ga_{0.6}As$ nanowire with R_c=0 nm (a), R_c=2 nm (b), R_c=4 nm (c), R_c=6 nm (d), R_c=8 nm (e) and R_c=10 nm (f) and R=10 nm) in [001] growth direction with 6×6 KL.

It is now of interest to investigate the influence of the presence of a camel back structure on the absorption spectrum. Figs. 3.12 and 3.13 show the evolution of the absorption spectra as function of the core radii, for nanowires with a radius of R=10 nm. Fig. 3.12 shows the results for wires with a GaAs core, while Fig. 3.13 shows the results for an $Al_xGa_{1-x}As$ core. The Al concentration is fixed to 0.4. Note that peaks are present for lower energies near the onset of the absorption spectra in Figs. 3.12(a), (e) and (f) and Figs. 3.13(a) and (f). These are due to the camel back structure of the top valence band. The camel back structure causes the conduction band and the valence band to be equidistant around k_z=0, leading to a peak in the absorption spectrum. In case of Fig. 3.12(d) the large peak is due to the camel back structure in the second excited state (see Fig. 3.8(c)).

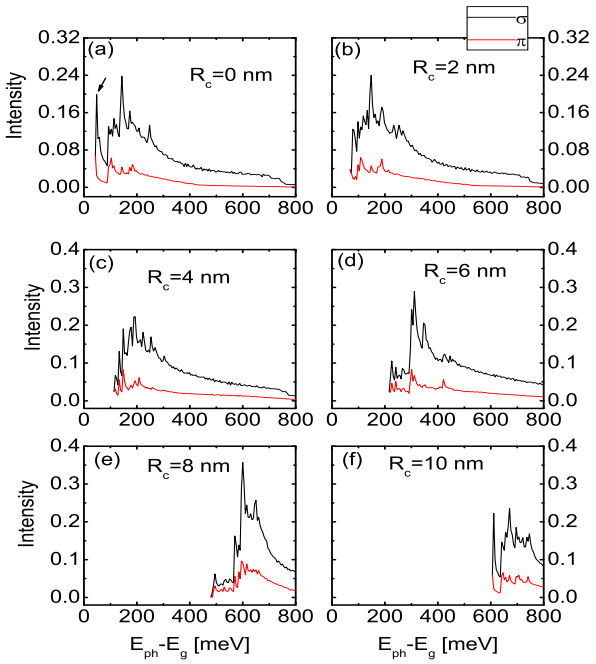

Figure 3.13: Absorption intensity (arbitrary units) for $Al_{0.4}Ga_{0.6}As/GaAs$ nanowire with R_c=0 nm (a), R_c=2 nm (b), R_c=4 nm (c), R_c=6 nm (d), R_c=8 nm (e) and R_c=10 nm (f) and R=10 nm) in [001] growth direction with 6×6 KL.

From the absorption results we can also see that there are certain energies for which the intensity peaks are only found for circularly polarized light (σ) and not for linearly polarized light (π). Examples are marked by arrows in Figs. 3.12 and 3.13. A look at the Eqs. (3.24), (3.25) and (3.26) shows that these must be due to heavy hole → conduction band transitions.

In Fig. 3.14 we give the degree of circular polarization (Π) for $GaAs/Al_xGa_{1-x}As$ nanowire for different x values for a particular case with R_c=2 nm (see Fig. 3.12(b)). Here we see that as x changes from 0.1 to 0.4, the degree of circular polarization (Π) changes from positive to negative values (identified by arrows in Fig. 3.14). This shows that for these values initially, $I_{\sigma_+} \gg I_{\sigma_-}$ and then $I_{\sigma_+} \ll I_{\sigma_-}$. And from Eqs.(3.24), (3.25) and (3.26) we may conclude that for positive Π values electrons with spin $\downarrow$ and for negative Π values electrons with spin $\uparrow$ are preferentially excited in the conduction band. Thus depending on whether left- or right-handed circularly polarized

light is used, at certain energies, spin polarized electrons can be obtained. For example the positive peak in Fig. 3.14(d) (identified by an arrow) shows that left-handed circularly polarized light (σ_+) of energy E=520.67 meV can excite spin $\downarrow$ electrons with higher probability.

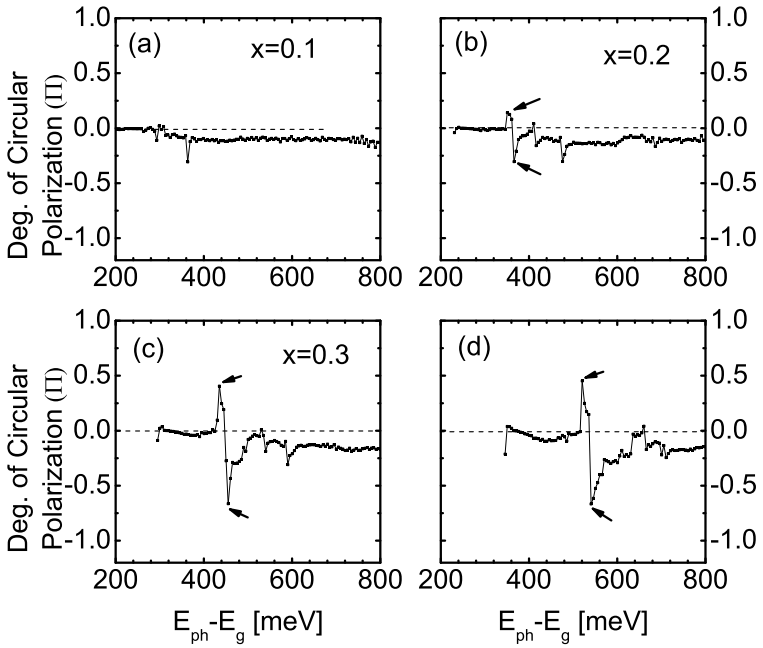

Figure 3.14: Degree of circular polarization (Π) for GaAs/$Al_xGa_{1-x}As$ R_c=2 nm and R=10 nm with x=0.1 (a), x=0.2 (b), x=0.3 (c) and x=0.4 (d).

An interesting aspect of the camel back structure of the top of the valence band is its effect on the lifetime of the exciton: a k-indirect transition would occur with a strongly reduced transition probability giving rise to long recombination times. This suggests that the lifetime of the exciton is larger in pure wires where a camel back structure exists in comparison with core-shell nanowires where there is a smaller or even no camel back structure. In fact, the opposite is the case, as will be shown in the next section where we investigate the radial localization of electron and hole in the nanowire.

3.4 Electron and hole probabilities

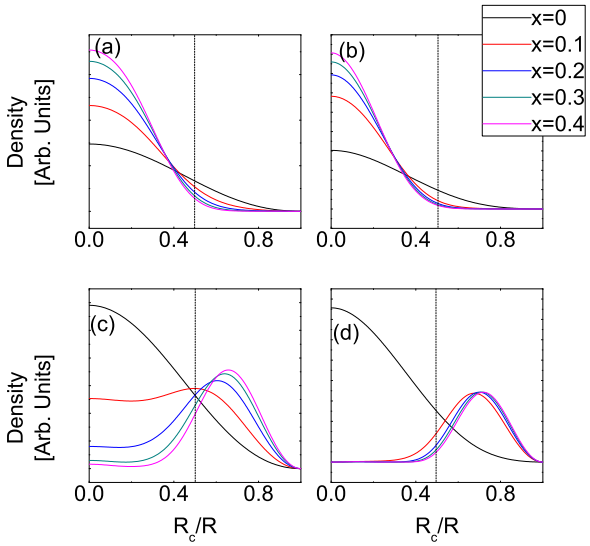

Figure 3.15: Electron ($\Psi^2_{el}(\rho)$) (a), (b) and hole ($\Psi^2_h(\rho)$) (c), (d) densities (of the ground state at k_z=0) for GaAs/$Al_xGa_{1-x}As$ (a), (c) and $Al_xGa_{1-x}As$/GaAs (b), (d) nanowires with R_c=5 nm and R=10 nm in [001] growth direction for different x values.

As an example we focus again on the nanowire with a radius of R=10 nm, and a core radius of R_c=5 nm. Figs. 3.15(a) and (b) show the electron and hole densities, respectively, at k_z=0 for a wire with a GaAs core, and Figs. 3.15 (c) and (d) for a $Al_xGa_{1-x}As$ core, for different Al concentrations. For the wire with a GaAs core, increasing the Al concentration pushes the electron and hole more towards the center of the nanowire. The change in localization is however more pronounced in wires with an $Al_xGa_{1-x}As$ core. Even a small concentration of Al causes the hole to be pushed almost completely into the shell. Also the electron is pushed into the shell, but still penetrates in the core due to its lighter mass in comparison to the holes. This change in localization due to the core-shell structure and the different impact on electrons and holes leads to a reduction of the overlap squared $|\langle\Psi^\sigma_{el}|\Psi^\nu_h\rangle|^2$ between electron and hole states. Figs. 3.16(a), (b), (c) and (d) show the average value of position $\langle\rho\rangle$ ($=\int \rho|\Psi|^2\rho d\rho$) for wires with a GaAs and with a $Al_xGa_{1-x}As$ core, as function of the core radius R_c. Note that

the overlap squared is strongly reduced in the core-shell nanowires when compared to single material nanowires and hence we predict a large increase of the exciton lifetime in them.

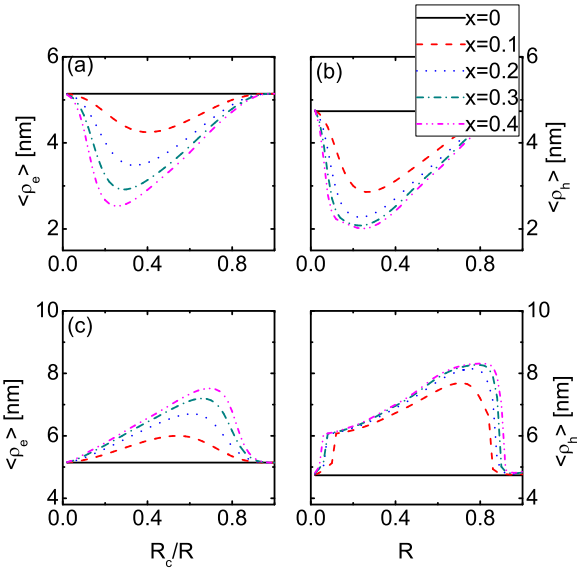

Figure 3.16: Average value of position $\langle\rho\rangle(\int \rho|\Psi|^2\rho d\rho)$ of electrons (a), (c) and holes (b), (d) (of the ground state at $k_z = 0$) for GaAs/$Al_xGa_{1-x}As$ (a), (b) and $Al_xGa_{1-x}As$/GaAs (c), (d) nanowires with R=10 nm and R_c=1 nm to 10 nm in [001] growth direction for different x values.

3.5 Summary and Conclusions

We have investigated the electronic structure of GaAs/$Al_xGa_{1-x}As$ and $Al_xGa_{1-x}As$/GaAs core-shell nanowires grown in the [001] direction using the 6×6 Kohn-Lüttinger **k.p** Hamiltonian. We showed that the 4×4 model breaks down for thin nanowires. It is also shown that the camel back structure of the top of the valence band around k_z=0, which is present in pure GaAs nanowires, slowly disappears with increasing Al concentration. We found that the camel back structure is not always present in core-shell structures. When GaAs is the core material, the evolution of the camel back structure as function of the core radius is almost independent of the Al concentration, while for wires with a GaAs shell, the region in which a camel back structure can be observed is larger for smaller Al concentration.

We also calculated the absorption spectra for different polarized light and found that a change in the effective mass of electrons and holes in the ground state is reflected in the absorption spectra: a camel back structure leads to a peak in the absorption spectrum because the top of the valence band and the bottom of the conduction band are equally aligned in some part of the Brillouin zone. We find a broad absorption spectra for thick wires, but for thin wires many more absorption peaks are observable due to the quantum confinement effect. We predict that spin polarized electrons can be obtained by using circularly polarized light for specific energies.

Wires with a GaAs core localize both the electron and the hole in the core region, while wires with a $Al_xGa_{1-x}As$ core push them to the shell region. In both cases the core-shell structure reduces the overlap of their wave functions, which will lead to an increase of the lifetime of the exciton.

Chapter 4

The k.p model for narrow gap semiconductor nanowires : 6-band vs 8-band k.p modeling

In this chapter we do a comparative study of the 6-band and the 8-band **k.p** models for narrow gap semiconductor nanowires*. The electronic properties of freestanding nanowires [87] made of various materials have been studied. In some of these materials the top valence band exhibits a camel-back structure even in direct band gap semiconductors [119, 120]. This camel-back structure is due to the HH and LH mixing which is enhanced in nanostructures due to confinement, as also shown in Fig. 1.2(b). It results in a peak in the absorption spectrum and an increase in the exciton lifetimes. It has been proposed that tensile-strained multiple quantum-well (MQW) structures with a camel-back shaped first valence subband can exhibit large refractive index changes due to current injection [121].

Properties due to the camel-back structure of the valence band in freestanding core shell nanowires have been studied recently using multiband **k.p** models [119, 120]. It was found that the presence or absence of a camel-back depends on the **k.p** model (4 or 6-band) and this was even more so for thinner wires. However this study was only applicable for large band gap materials, as 4 and 6-band models fail to describe materials with band gaps much smaller than 1 eV, where the influence of the conduction band is large. This motivated us to apply in the present chapter the 6-band and 8-band **k.p** models to zincblende freestanding nanowires with different band gap values and compare the results for the hole states. We also focus on the

*V. V. Ravi Kishore, N. Cukaric, B. Partoens, M. Tadic and F. M. Peeters: Hole subbands in freestanding nanowires: 6-band versus 8-band k.p modelling, *J. Phys.: Condens. Matter* **24**, 135302 (2012).

camel-back structure as it is a particular feature of these nanowires. Furthermore, the effect of the different Luttinger-like parameters in the 8-band model on the hole electronic structure is investigated. We employed both the Pidgeon-Brown [88] and Bahder-Pryor [89, 90] approaches when modifying the Luttinger parameters. The effects of the choice of the Luttinger parameters is illustrated for the case of bulk semiconductors, where we choose GaAs as an example of a large band-gap semiconductor, and InAs and GaSb, which are low band-gap semiconductors. The choice of the appropriate set of the modified Luttinger parameters is an important issue in the case of nanostructures. In addition to bulk related terms in the Hamiltonian which determine the expectation value of the kinetic energy, the electron and hole eigenenergies depend on the confinement potential.

In freestanding nanowires, confinement breaks the condition of transversal symmetry, which leads to splitting of the energy levels. Furthermore, the boundary conditions for the electron and hole wave function are such that both the electron and hole are localized, therefore mixing between them increases, which may lead to interesting effects in the band structure, like anti-crossings between the hole levels and a negative effective mass of the hole ground state (camel-back structure). When the band gap is small, the effects of band mixing could also be large in the valence band, and therefore application of the 8-band **k.p** approach is required, especially for low-band gap semiconductors, like InAs and InSb. We analyze differences between the hole states obtained by using different Luttinger parameters. Furthermore, we analyze how the choice of the Kane parameter, which describes the coupling between the conduction (Γ_6) and valence (Γ_8 and Γ_7) bands, affects the electronic structure.

Our aim is to resolve whether important details are found in the 8-band model which are however missing in the 6-band approach. We especially consider the conditions under which the camel-back features which are present in the ground valence subband according to 6-band calculations, as previously found in [119, 120], are removed in the 8-band model. In order to resolve how different terms of the multiband Hamiltonian affect the hole dispersion relations, we compute the expectation values of a few dominant matrix elements in the multiband Hamiltonians. Special emphasis is put in a comparison of the contributions, of the diagonal terms and the terms that mix the heavy and light hole states of the hole subband to the energy.

4.1 Luttinger and Luttinger-like parameters

Luttinger introduced the so-called Luttinger parameters $\gamma_1, \gamma_2, \gamma_3$ to describe the Γ_8 band in a 4×4 Hamiltonian $\mathbb{H}_4$. Later, not only the $\mathbb{H}_4$ Hamiltonian but also the 6×6 Hamiltonian was written with the same γ_j's. However, strictly speaking, the parameters that describe the Γ_7 band in the $\mathbb{H}_6$ Hamiltonian, say $\gamma_{\Delta j}$, are equal to γ_j only for zero spin-orbit splitting. Boujdaria et al. [94] showed that to describe the bulk band structure of GaAs,$\gamma_{\Delta j} \approx \gamma_j$ is a good approximation, while for InAs, for example, $\gamma_{\Delta 1}$ is 74 % smaller than γ_1, and for InSb γ_1 is almost four times larger than $\gamma_{\Delta 1}$.

In order to describe simultaneously the conduction band Γ_6 and the valence bands Γ_8 and Γ_7 in an 8×8 Hamiltonian $\mathbb{H}_8$ one has to introduce the Luttinger-like parameters $\tilde{\gamma}_j$ as a correction to the Luttinger parameters. This modification is a result of the Löwdin perturbation which should be employed when the 8-band model is modified to the 6-band **k.p** theory. The essential parameter in this procedure is the energy of the unperturbed states, whose value depends on the range of energies of interest. In the literature, in essence two sets of relations can be found. Pidgeon and Brown [88] used the following relations

$$\begin{aligned} \tilde{\gamma}_1 &= \gamma_1 - \frac{E_P}{3E_G}, \\ \tilde{\gamma}_j &= \gamma_j - \frac{E_P}{6E_G}, \quad j = 2, 3, \end{aligned} \tag{4.1}$$

which were used both for the Γ_8 and Γ_7 bands. We will refer to these parameters as PB parameters. In papers by Bahder [89] and Pryor [90], the following relations were used

$$\begin{aligned} \tilde{\gamma}_1^{BP} &= \gamma_1 - \frac{E_P}{3(E_G + \Delta/3)}, \\ \tilde{\gamma}_j^{BP} &= \gamma_j - \frac{E_P}{6(E_G + \Delta/3)}, \quad j = 2, 3, \end{aligned} \tag{4.2}$$

where the energy $E_G + \Delta/3$ is the difference between the energy of the conduction band and the energy of the *center of gravity* of the valence band, as stated in Ref. [94] and will be referred to as BP parameters. Here E_G is the band gap, Δ is the split-off energy, and E_P is the Kane energy defined as

$$E_P = \frac{2m_0}{\hbar^2} P^2, \tag{4.3}$$

Table 4.1: Band parameters, and Luttinger and Luttinger-like parameters for GaAs, InAs and InSb.

	GaAs [86]	InAs [86]	InSb [116]
E_G (eV)	1.519	0.417	0.25
E_P (eV)	23.81	21.5	24.08
Δ (eV)	0.341	0.39	0.82
γ_1	7.05	20	34.8
γ_2	2.35	8.5	15.5
γ_3	3	9.2	16.5
$\tilde{\gamma}_1$	1.8251	2.8137	2.6933
$\tilde{\gamma}_2$	-0.2625	-0.0931	-0.5533
$\tilde{\gamma}_3$	0.3875	0.6069	0.4467
$\tilde{\gamma}_1^B$	2.1888	6.8982	19.4624
$\tilde{\gamma}_2^B$	-0.2411	1.9491	7.8312
$\tilde{\gamma}_3^B$	0.5694	2.6491	8.8312
$\gamma_{\Delta 1}$	5.8967	11.2505	9.603
$\gamma_{\Delta 2}$	2.1516	6.4953	9.4425
$\gamma_{\Delta 3}$	2.7194	7.0519	10.2549
$\tilde{\gamma}_{\Delta 1}$	1.6297	2.3699	2.1014
$\tilde{\gamma}_{\Delta 2}$	-0.2214	0.011	-0.4199
$\tilde{\gamma}_{\Delta 3}$	0.3465	0.5027	0.3132

where $P = \frac{\hbar}{m_0}\langle S|p_x|X\rangle = \frac{\hbar}{m_0}\langle S|p_y|Y\rangle = \frac{\hbar}{m_0}\langle S|p_z|Z\rangle$ are the inter-band matrix elements between the conduction band (Γ_6) and the valence bands (Γ_8 and Γ_7). The different relations lead to large differences in the values for the $\tilde{\gamma}$'s as was shown in [94]: the ratio$\tilde{\gamma}_1^{BP}/\tilde{\gamma}_1$ for GaAs is 1.19, for InAs 2.45, and for InSb even 16.06. However, it was convincingly shown in [94] that the correct expressions are the PB parameters.

In the next section, we investigate the influence of the different relations PB and BP on the energy structure of a nanowire. We also address the question under what conditions a 6-band model is sufficient and when an 8-band model has to be used and we investigate the effect of the approximations $\gamma_j \approx \gamma_{\Delta j}$ and $\tilde{\gamma}_j \approx \tilde{\gamma}_{\Delta j}$ for a nanowire. Thus where in [94] the bulk band structure was considered, here we focus on the influence on the energy structure of a nanowire with a special emphasis on the camel-back structure.

4.2 Bulk band structure

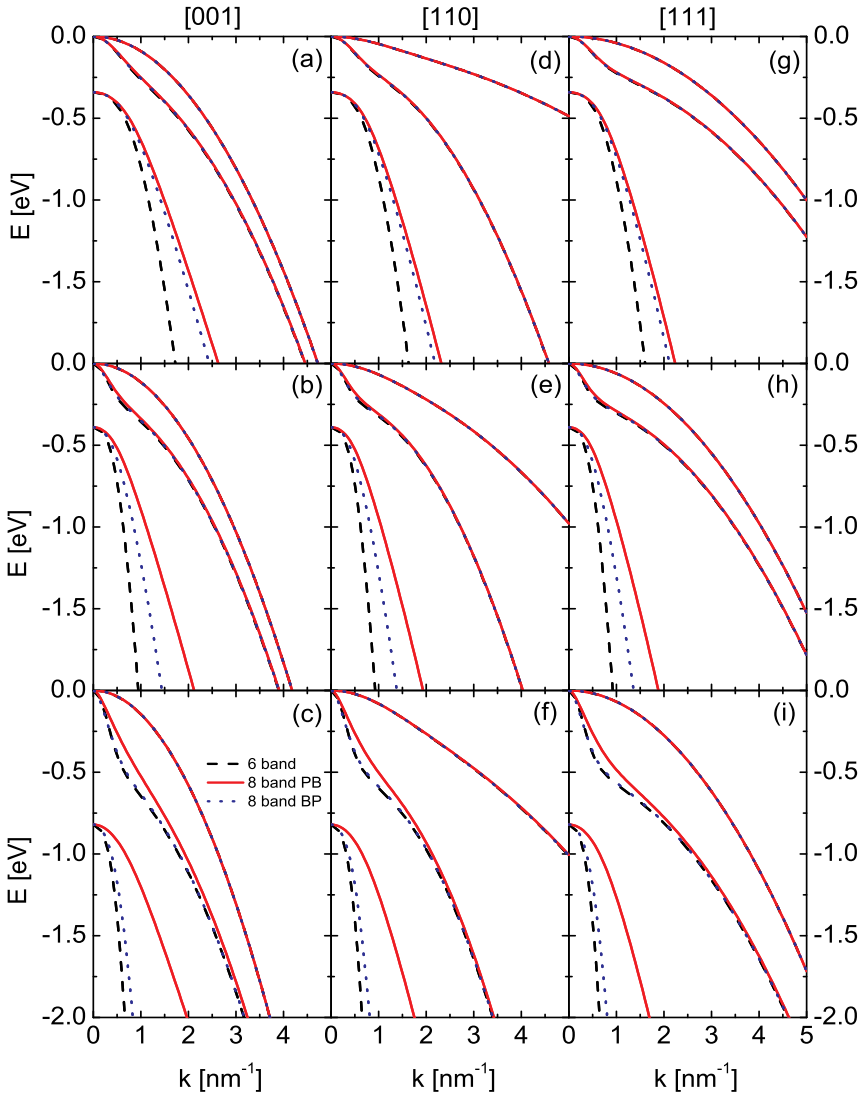

Figure 4.1: (Colour online) Bulk band diagrams for (a, d, g) GaAs , (b, e, h) InAs and (c, f, i) InSb along the [001], [110] and [111] directions. Results are shown for 6-band (dashed lines), 8-band using PB parameters (solid lines) and 8-band using BP parameters (dotted lines).

In this chapter we concentrate on three zincblende III-V semiconductors: GaAs, InAs and InSb. The used Luttinger, Luttinger-like parameters, band

gap E_G and spin-orbit splitting Δ for those materials are summarized in Table 4.1. For GaAs $E_G \gg \Delta$, for InAs $E_G \approx \Delta$, and for InSb $E_G \ll \Delta$. Before discussing the effects of the different relations PB and BP on the electronic structure of the nanowire, we first show the bulk valence band structure for these three semiconductors in Fig. 4.1 given by $\mathbb{H}_6$ (with the Luttinger parameters) and $\mathbb{H}_8$ (both with the Luttinger-like parameters from the relations PB and BP). Here the approximations $\gamma_j \approx \gamma_{\Delta j}$ and $\tilde{\gamma}_j \approx \tilde{\gamma}_{\Delta j}$ were made, thus only three Luttinger and Luttinger-like parameters were used. The bulk band structure is calculated for the different directions [001], [110] and [111]. In the appendix the explicit expression of the used Hamiltonian is given.

From Fig. 4.1 we see that for bulk GaAs we can see that the $\mathbb{H}_6$ Hamiltonian is sufficient to describe the bulk valence band structure. The results obtained with the $\mathbb{H}_8$ model with both sets of Luttinger-like parameters are also very similar, because $E_G \gg \Delta$. For bulk InAs, the light-hole band obtained from $\mathbb{H}_6$ starts to deviate from the most accurate result obtained with $\mathbb{H}_8$ and the Luttinger-like parameters PB. This deviation is even more pronounced for InSb. Note that the light-hole band obtained with $\mathbb{H}_8$ and the Luttinger-like parameters BP is almost identical to the one obtained with $\mathbb{H}_6$. This shows that the Luttinger-like parameters BP underestimate the coupling between conduction and valence bands. So we can conclude that to describe the bulk band structure the 6-band model ($\mathbb{H}_6$) works well for GaAs, but for InAs and InSb one should use the 8-band model ($\mathbb{H}_8$). In the next section we investigate whether the same conclusions are valid for freestanding nanowires made of these materials.

4.3 Bandstructure of Nanowires

Let us now investigate if the same models also describe correctly the valence band structure of a nanowire. As we are interested in the effects of band mixing due to the confinement effect, we consider thin GaAs, InAs, and InSb cylindrical nanowires grown in the [001] crystallographic direction with a radius of 10 nm. This choice of radius R=10 nm is made to properly illustrate the camel back feature of the top valence band. Fig. 4.2 shows the energy difference between the ground state energy and the first four excited states at Γ, as a function of the radius. The energy difference between the ground and the excited states decreases as we increase the radius of the wire, thus making R=10 nm the ideal choice where the camel-back feature might be prominent. Furthermore, nanowires with such diameters have already been synthesized [44]. The valence band structures obtained with the same three Hamiltonians are shown in Fig. 4.3. As stated in Reference [94], the PB rela-

tions (Eq.(4.1)) are the most accurate Luttinger-like parameters. Therefore we consider the solid curves in Fig. 4.3 as the most accurate ones.

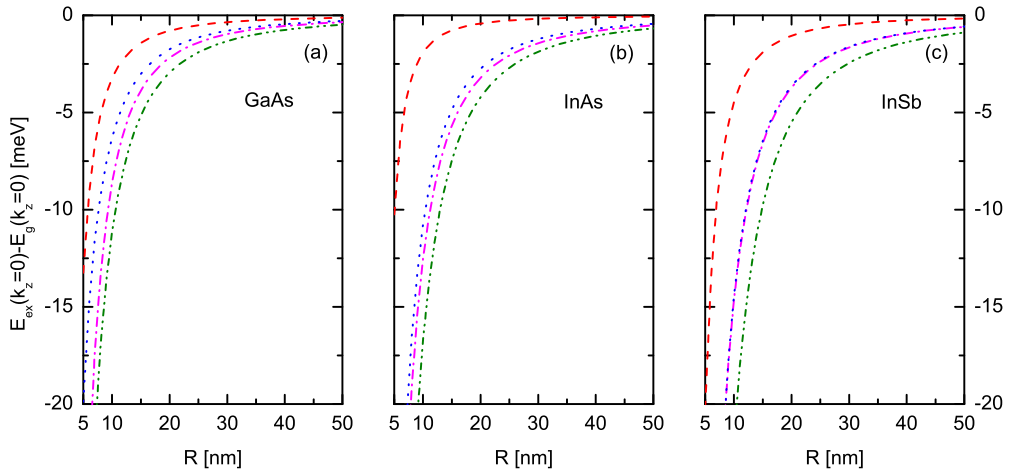

Figure 4.2: (Colour online) Energies of the first four excited states with reference to the ground state energy at k_z=0 for different radii (R=5 to 50 nm) using PB relations (Eq.(4.1)), for GaAs (a), InAs (b) and InSb (c) nanowires, respectively.

From the previous bulk results on GaAs it is expected that for small k values the 6-band model is sufficient to describe the valence band electronic structure. However, note that in Fig. 4.3(a) a camel-back structure is observed in the top of the valence band in the 6-band model, while it is absent in both 8-band models. This shows that, although GaAs nanostructures are often treated in the literature within a 6-band model, an 8-band model might be necessary for a correct description of the valence band structure. The general idea that the size of the band gap with respect to the spin-orbit splitting [94] is the crucial factor that determines if a 6-band model is sufficient, or that an 8-band model is necessary, is thus not correct. The reason is that the value of E_P is another important factor. E_P couples the conduction band Γ_6 with the valence bands Γ_7, Γ_8 and is proportional to the square of the matrix element $\langle S|p_x|X\rangle$, which is independent of the band gap E_G.

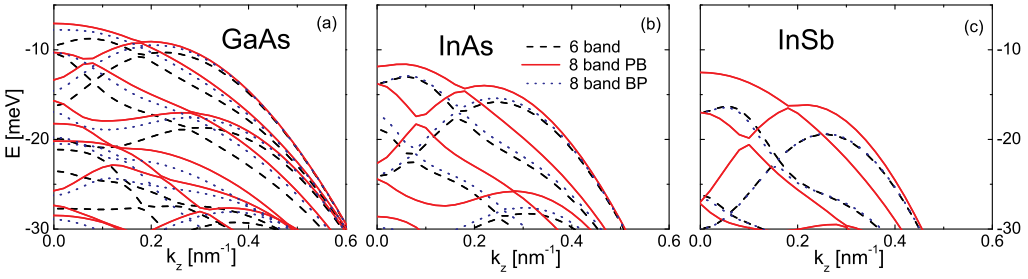

Figure 4.3: (Colour online) Valence subbands of (a) GaAs, (b) InAs and (c) InSb nanowires with radius R=10 nm grown in [001] direction obtained using 3 different models.

Let us now consider the case of an InAs nanowire as shown in Fig. 4.3(b). Because $E_G \approx \Delta$, it is expected that an 8-band model is necessary to describe the electronic structure correctly. Here, the 6-band model shows a camel-back structure, but it also appears in both 8-band models (see Fig. 4.3(b)). However, in the case of InSb nanowires there is no camel-back structure in the 8-band using PB relations (Eq.(4.1)), but there is one in the other two cases. For both InAs and InSb nanowires, the 6-band model is not accurate, as can be expected from their small gap values in comparison with the spin-orbit splitting. But also note that the 8-band model with the Luttinger-like parameters BP differs significantly from the 8-band model with the correct Luttinger-like parameters PB. The results of the former 8-band model coincides almost with the results from the 6-band model, showing again an underestimation of the coupling between valence and conduction bands. Thus, we will use the Luttinger-like parameters PB in the rest of the chapter. Also it is important to note that the camel-back structure observed in the 6-band results is not always present in the 8-band model (see Fig. 4.3), therefore we explore the properties of the camel-back structure further in the next section.

But first we illustrate the effect of the approximations $\gamma_j \approx \gamma_{\Delta j}$ and $\tilde{\gamma}_j \approx \tilde{\gamma}_{\Delta j}$ on the nanowire valence band. As stated in [94], for large E_G or small Δ, the approximations $\gamma_j \approx \gamma_{\Delta j}$ and $\tilde{\gamma}_j \approx \tilde{\gamma}_{\Delta j}$ are valid. Fig. 4.4 shows the valence band structure again for the same GaAs, InAs and InSb nanowires, obtained within the 8-band model with both the 3-parameter (8-band PB3) and the 6-parameter (8-band PB6) model (see Appendix for detailed expressions). From these results it is very clear that the approximations $\gamma_j \approx \gamma_{\Delta j}$ and $\tilde{\gamma}_j \approx \tilde{\gamma}_{\Delta j}$ are valid for GaAs nanowires. In case of InAs and InSb there are some small differences for the excited hole states but still the approximation appears to be reasonably accurate. Thus we will make

the approximation $\gamma_j \approx \gamma_{\Delta j}$ and $\tilde{\gamma}_j \approx \tilde{\gamma}_{\Delta j}$ in the rest of the chapter.

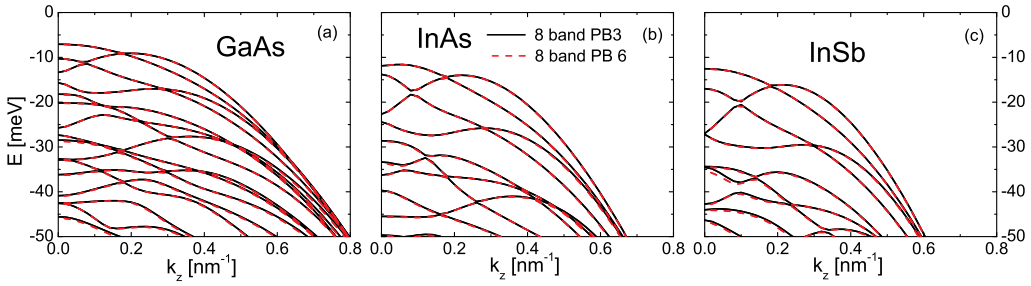

Figure 4.4: (Colour online) Valence subbands of (a) GaAs, (b) InAs and (c) InSb nanowires with radius R=10 nm as obtained using the 3-parameter (solid curves) and the 6-parameter (dashed curves) models.

4.4 Camel-back structure and its properties

The camel-back structure which was observed in the ground state valence subband dispersion relation is a very interesting feature as the effective mass in this region is negative, which is opposite to the bulk effective mass of the holes. This results in an increase in the number of equal energy transitions between the ground state valence band and the conduction bands. In [119, 120], the authors have studied the camel-back structure in both freestanding nanowires and core-shell nanowires. They have shown that this camel-back structure can result in a peak in the absorption spectra which should be experimentally observable. In the present chapter we discuss the properties of the camel-back structure in freestanding nanowires using an 8-band **k.p** model.

Let us now discuss the camel-back structure in more detail. In Fig. 4.3 it is very clear that except for InAs the camel-back structure is only seen in the 6-band model. However, different E_P values can be found in the literature for InAs, E_P = 21.5 eV in [116] and E_P = 22.2 eV in [122] . In order to show the importance of E_P, Fig. 4.5(b) gives the valence band structure for the same InAs nanowire, where the valence band structures for both values are given. Here E_P=21.5 eV [116] gives a small camel-back as mentioned before, but a slightly larger value of 22.2 eV [122] removes this effect. We do a similar study for the GaAs nanowire (see Fig. 4.5(a)), where we use E_P = 15 eV (unrealistic value) and E_P = 23.81 eV [86] for the 8-band model, which confirms that a smaller value of E_P gives results closer to the 6-band model.

And similar results are obtained for the InSb nanowire using different E_P values, $E_P = 23.3$ eV [116] and $E_P = 24.08$ eV [86] (see Fig. 4.5(c)). Note that in case of GaAs, a value of $E_P = 21$ eV which is obtained from the theoretical relation [123]

$$E_P = 3(\frac{m_0}{m_e^*} - 2)(\frac{2}{E_G} + \frac{2}{E_G + \Delta_0})^{-1}, \tag{4.4}$$

which is often suggested to remove spurious solutions, also produces a small camel-back. This shows clearly that the band structure is very sensitive to the E_P value.

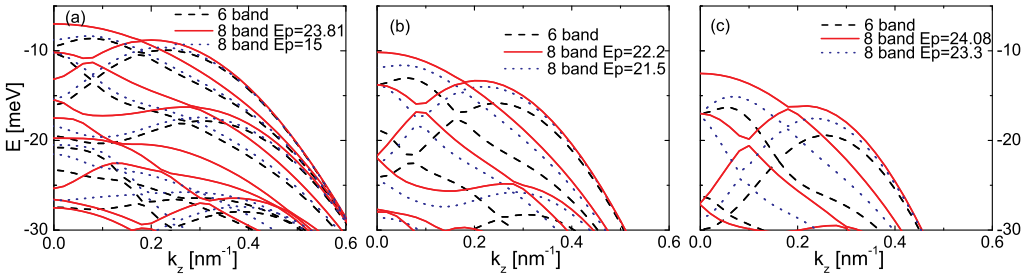

Figure 4.5: (Colour online) Valence subbands of (a) GaAs, (b) InAs and (c) InSb nanowires with radius R=10 nm obtained using the PB parameters with different E_P values.

As Fig. 4.5 shows, the camel-back feature occurs if the 6-band model is adopted and is missing in the 8-band model for large E_P values. In order to get more insight into the existence of the camel-back structure, we resolve the contributions of the Hamiltonian matrix elements to the hole ground subband energy. If we denote the normalized ground state wave function in the 8-band model by

$$|\Phi\rangle \equiv |\phi_1\phi_2\phi_3\phi_4\phi_5\phi_6\phi_7\phi_8\rangle \equiv |\varphi^{\frac{1}{2}}_{e,\frac{1}{2}}, \varphi^{-\frac{1}{2}}_{e,\frac{1}{2}}, \varphi^{\frac{3}{2}}_{hh,\frac{3}{2}}, \varphi^{\frac{1}{2}}_{lh,\frac{3}{2}}, \varphi^{-\frac{1}{2}}_{lh,\frac{3}{2}}, \varphi^{-\frac{3}{2}}_{hh,\frac{3}{2}}, \varphi^{\frac{1}{2}}_{so,\frac{1}{2}}, \varphi^{-\frac{1}{2}}_{so,\frac{1}{2}}\rangle,$$

where $\varphi^m_{x,j}$ $(x\epsilon\{e, hh, lh, so\})$ are the envelope wave functions corresponding to the Bloch function $|jm\rangle$, the energy of the ground state is expressed as the sum of the expectation values of its matrix elements:

$$\langle\Phi|\mathbb{H}_8|\Phi\rangle = \sum_{i=1}^{8}\sum_{j=1}^{8}\langle\phi_i|H_{ij}|\phi_j\rangle.$$

We note that because of the symmetry of the confining potential, the hole subbands in a nanowire are double Kramers degenerate. Furthermore, because of the Hermitian character of the Hamiltonian, the expectation values of the matrix elements H_{ij} and H_{ji} are complex conjugate of each other, therefore their joint contribution to the valence subband energy amounts to $2Re(\langle\phi_i|H_{ij}|\phi_j\rangle)$. As a matter of fact, the valence-band energy can be resolved in the following contributions of the zone-center states: (1) the electron zone-center states $EL = \langle\phi_1|H_{11}|\phi_1\rangle + \langle\phi_2|H_{22}|\phi_2\rangle$, (2) the heavy-hole zone-center states $HH = \langle\phi_3|H_{33}|\phi_3\rangle + \langle\phi_6|H_{66}|\phi_6\rangle$, (3) the light-hole zone-center states $LH = \langle\phi_4|H_{44}|\phi_4\rangle + \langle\phi_5|H_{55}|\phi_5\rangle$, (4) the split-off zone-center states $SO = \langle\phi_7|H_{77}|\phi_7\rangle + \langle\phi_8|H_{88}|\phi_8\rangle$, (5) the mixing term B between the heavy and light holes $B = 2Re(\langle\phi_3|H_{34}|\phi_4\rangle)$, and (6) the contribution of the mixing term C between the light and heavy holes $C = 2Re(\langle\phi_3|H_{35}|\phi_5\rangle)$. It turns out that the contribution of SO and the terms which mix the electron and hole zone-center states (P terms, see Appendix) are much smaller than the ones due to mixing between the heavy and light-hole zone-center states. Therefore, we do not include them in our discussion below. The total energy of the hole (valence-band) state is denoted by VB in all diagrams. The calculation is performed for nanowires made of the same three materials as before, which have a different ratio between the band gap and the split-off energy: (1) GaAs, where $E_G \gg \Delta$, (2) InAs, where $E_G \approx \Delta$, and (3) InSb, where $E_G \ll \Delta$. The results are given for nanowires with a radius R=10 nm. Qualitatively, the same results were found for other radii.

4.4.1 GaAs Nanowire ($E_G \gg \Delta$)

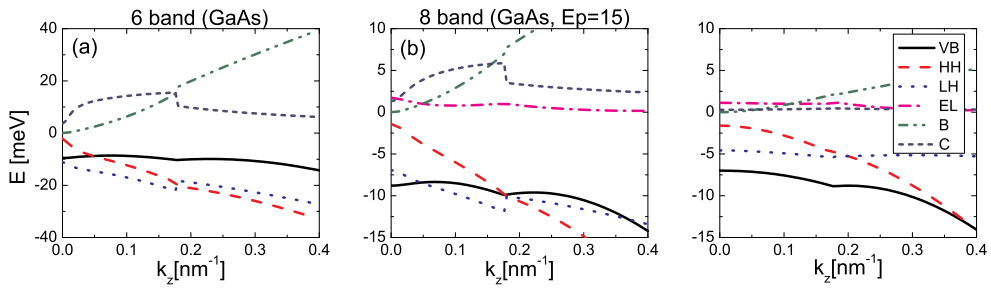

Figure 4.6: (Colour online) Valence ground state and important contributions to it, for a GaAs nanowire with radius R=10 nm obtained using the PB parameters for (a) the 6-band model, (b) the 8-band model with E_P=15 eV, and (c) the 8-band model with E_P=23.81 eV.

In Fig. 4.6 we present the valence band ground state energy (VB) and the most important contributions to its energy for a GaAs nanowire of radius R=10 nm. Results obtained by using three different models are shown: the 6-band model which is shown in Fig. 4.6(a), the 8-band model with $E_P = 15$ eV in Fig. 4.6(b) and $E_P = 23.81$ eV in Fig. 4.6(c). The diagonal heavy (HH) and light hole (LH) contributions decrease as function of k_z. However, the contribution from the interaction between the heavy and light holes (B and C) increases in the 6-band model, which appears to be the origin of the camel-back structure. In the results of the 8-band model (see Fig. 4.6(c)), this increase is much smaller, especially the contribution from the interaction between the heavy and light holes with opposite spin (C), which leads to the disappearance of the camel-back structure. This change in coupling between heavy and light holes can only be caused by the extra coupling of both bands with the conduction band, whose strength is given by the value of E_P, which can be seen from the contributions in Fig. 4.6(b), where $E_P = 15$ eV. In general we see that the diagonal terms HH and LH increase with increasing E_P. However, the coupling terms, B and C decrease with increasing E_P. The different contributions in Fig. 4.6 show discontinuities which are due to the ground state transitions as a function of k_z visible in the band diagram of Fig. 4.5.

4.4.2 InAs Nanowire ($E_G \approx \Delta$)

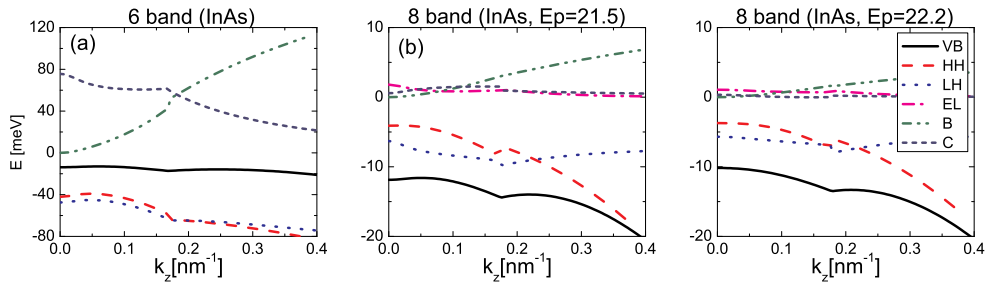

Figure 4.7: (Colour online) Valence ground state and important contributions to it, for a InAs nanowire with radius R=10 nm obtained using the PB parameters for (a) the 6-band model, (b) the 8-band model with E_P=21.5 eV, and (c) the 8-band model with E_P=22.2 eV.

In case of the InAs nanowire, we present results for two sets of E_P values, $E_P = 22.2$ eV and $E_P = 21.5$ eV for R= 10 nm (see Fig. 4.7). The diagonal

terms HH and LH in the 6-band model have a camel-back shape. But here we see that the coupling between light and heavy holes of opposite spin (C) decreases with k_z for the 6-band model, whereas this was opposite in the case of GaAs . In the case of the 8-band model the camel-back shape of HH and LH terms vanishes, but C behaves just as in the 6-band GaAs case. The coupling term B is always increasing in both GaAs and InAs, since it is proportional to k_z. Also it is worth noting that the energy of the heavy hole (HH) term is not effected by changing the E_P value (see Figs. 4.7(b) and 4.7(c)).

4.4.3 InSb Nanowire ($E_G \ll \Delta$)

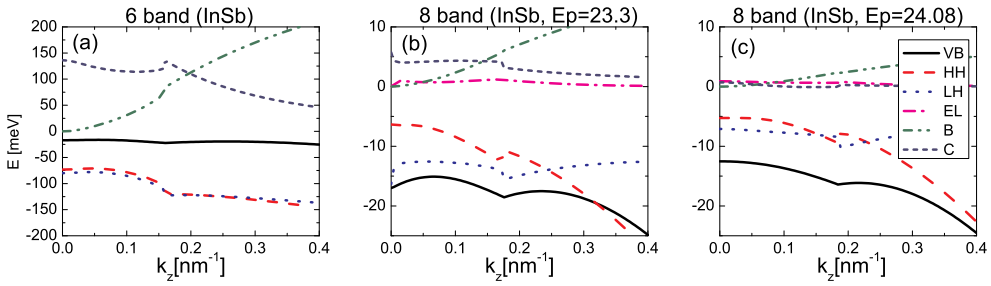

Figure 4.8: (Colour online) Valence ground state and important contributions to it, for a InSb nanowire with radius R=10 nm radius obtained using the PB parameters for (a) the 6-band model, (b) the 8-band model with E_P=23.3 eV, and (c) the 8-band model with E_P=24.08 eV.

Finally we look at the InSb nanowire results. Here we take two sets of E_P values, E_P = 24.08 and E_P = 23.3 for R= 10 nm (see Fig. 4.8). Here also the diagonal terms decrease with increasing k_z, and the coupling terms B and C show similar behavior as in the case of InAs. An increase in E_P value decreases the contribution of the coupling terms B and C and thus reduces the camel-back feature.

4.4.4 Discussion

From the above results it is evident that in the case of wide gap materials like GaAs one needs a large change in the E_P value in order to restore the camel-back structure in the 8-band model. This is not the case with small band gap materials like InAs and InSb, where even a small change in the

E_P value brings back the camel-back in the 8-band model. These results are consistent with the PB relations (Eq.(4.1)), where we can see that the ratio E_P/E_G is an important factor. If we compare the Luttinger and the Luttinger-like parameters (see Table. 4.1), it becomes clear that the direct HH-LH coupling, through B and C, is overestimated in the 6-band model. Comparison of the expected values of B and C in the 6-band and the 8-band models leads to the same conclusion. Also it is important to note that, in case of InAs $\tilde{\gamma}_2 + \tilde{\gamma}_3$, which appears in the coupling term C (see Appendix) is large ($\approx$0.5) when compared to the values for GaAs and InSb ($\approx$0.1) (see Table. 4.1). This different value of $\tilde{\gamma}_2 + \tilde{\gamma}_3$ is responsible for the smaller contribution of the C term which in turn is responsible for the presence of the camel-back in the InAs 8-band results (see Fig. 4.7). From the 8-band model results, which show a camel-back structure, i.e., in GaAs with E_P=15 eV(Fig. 4.6(b)), in InAs with E_P=21.5 eV (Fig. 4.7(b)) and in InSb with E_P=23.3 eV (Fig. 4.8(b)), it is clear that the camel-back feature for the ground state hole subband is observed only when the light hole behavior is opposite to the behavior of the coupling term C.

4.5 Summary and Conclusions

We have made a comparative study of the valence band structure as obtained within the 6-band and the 8-band **k.p** models. Also we compared the results as obtained with different relations for the Luttinger-like parameters in the $\mathbb{H}_8$ Hamiltonian that can be found in the literature. We find that in case of nanowires, an 8-band description is necessary to obtain the correct valence band structure for GaAs, despite its large band gap. This is due to the large E_P value that gives the strength of the coupling between valence and conduction bands. For InAs and InSb nanowires, an 8-band model is also necessary for a more complete description of the valence band structure, as expected based on their small band gap values. Thus it is very clear that the choice of the model to describe a particular material depends on the band gap E_G, the split-off energy Δ and the Kane's energy E_P values. The Luttinger-like parameters presented in [89] underestimate the coupling between valence and conduction bands, and it is important to rely on the correct Luttinger-like parameters as given in [88] to describe the valence band structure of nanowires with a small band gap. The camel-back structure which is observed in the 6-band model for all the materials is not always observed in the case of the 8-band model. It can result in a peak in the absorption spectra as calculated in [119, 120] and also increase the exciton recombination lifetimes [124]. We found that the mixing between the light and heavy hole bands give the largest

contribution to the camel-back structure. This mixing is overestimated in wires treated within the 6-band model. These mixing terms are affected by variations of the Kane's inter-band energy E_P, in particular for narrow gap materials. In conclusion our theoretical results show that the possible presence of a camel-back structure in the hole ground subband dispersion is very sensitive to the choice of the E_P value.

Chapter 5

Electronic structure of type-III semiconductor nanowires

In this chapter we study the electronic structure of InAs/GaSb core-shell nanowires*. Nanowires with their one-dimensional quantum confinement effect have gathered a lot of attention in the recent past. Growth of single material freestanding nanowires of various materials has been achieved through methods such as molecular beam epitaxy [24] (MBE) and vapour liquid solid [23] (VLS) method. Apart from single material nanowires, core-shell nanowires of different combination of materials have also been realized. The latter have resulted in interesting structures, due to their different band alignments [38]. These structures can be classified into six different types, type I-s, type I-c, type II-s, type II-c, type III-s, and type III-c [38] (see Fig. 1.10 in the introduction), where 'c' and 's' represent the structures with electrons confined in core and shell respectively. These different types have been extensively discussed by Pistol *et. al.* [38]. It was shown that a shell of GaSb around an InAs nanowire core forms a type-III structure, with the GaSb valence band donating electrons to the conduction band of InAs.

In the present chapter, we perform a deeper analysis of such type-III nanowires, where the conduction band minimum of one material is below the valence band maximum of the other and vice-versa. Type-III heterostructures have recently gathered a lot of attention due to their enhanced transport properties. They are expected to have large electron densities at high temperatures [125], and thus can be used for quantum devices operating at high temperatures. Also heterostructures with antimonide materials have shown interesting electronic properties due to their high mobility [126]. They can

*V. V. Ravi Kishore, B. Partoens, and F. M. Peeters : Electronic structure of InAs/GaSb core-shell nanowires, *Phys. Rev. B* **86**, 165439 (2012).

be operated in the THz regime because of their tunable band structure [127, 128, 129]. Furthermore, they can be used in infra-red lasers and detectors [130, 131, 132]. InAs/GaSb superlattices have been studied extensively theoretically [133, 134, 135] as well as experimentally [136, 137, 138, 139, 140]. For example, InAs/GaSb superlattice photodiodes [141, 142, 143, 144] have been reported recently. The electronic [145] and optical properties [146] of InAs/GaSb quantum well systems were studied previously and their behavior in both electric [147] and magnetic fields [148] has given important information on spin polarization and the semiconductor-semimetal transition.

In InAs/GaSb quantum wells it was found that for certain thicknesses of InAs and GaSb, hybridization [134, 145, 149] occurs between electron and hole states which results in semi-metallic behavior. It was also shown theoretically that a small hybridization gap opens up and the presence of this hybridization gap was later verified experimentally [150, 151]. It is clear that up to now most attention was given to the electronic properties of InAs/GaSb quantum wells and superlattice structures.

The above properties of InAs/GaSb structures combined with the one dimensional nature of nanowires, can be used in the development of novel electronic devices. Recently, GaSb-InAs(Sb) heterostructure nanowires were studied for tunnel transistor applications [152, 153, 154]. Very recently, also GaSb/InAs(Sb) core-shell nanowires were experimentally realized [155]. It was shown how the carrier concentrations and the transport properties could be tuned from p-type to n-type by changing the shell thickness. Also, ambipolar transport was demonstrated for intermediate shell thickness. To get a better insight into these results, it is essential to understand the electronic and optical properties of these type-III core-shell nanowires, and in the present work we concentrate on the most promising InAs/GaSb core-shell nanowires.

We use the **k**.**p** method, which is computationally inexpensive and gives accurate results near the Γ point. As the InAs/GaSb core-shell nanowire has a type-III band alignment and as both InAs and GaSb have narrow band gaps, an 8-band **k**.**p** method with Pidgeon and Brown Luttinger-like parameters [88] is used to calculate the band structure and the optical properties.

In the next section we discuss the theoretical approach used in this chapter. In section 5.2 results of the band structure, the probability density of the valence and the conduction band ground states at k_z=0 and the absorption spectra for nanowires made of InAs, GaSb and their core-shell combinations are given. We introduce the hybrid states in these nanowires and study their properties.

5.1 Theory

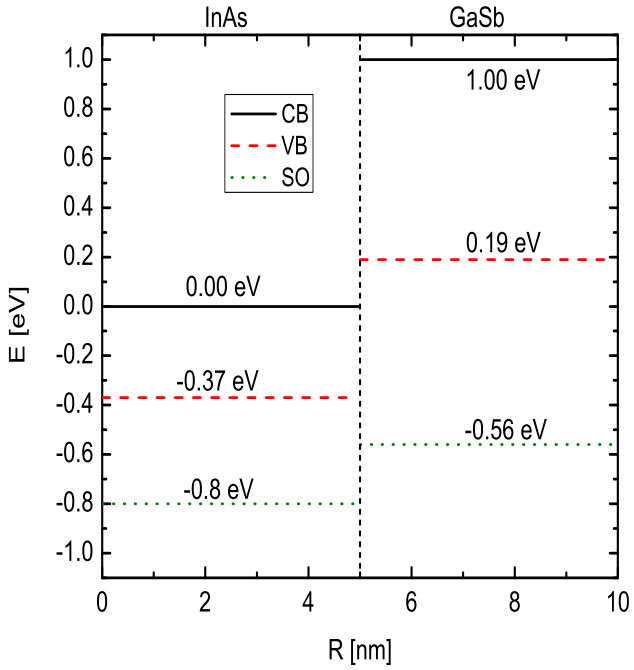

Figure 5.1: (Color online) Band alignment of InAs/GaSb core-shell nanowires with core radius R_c=5 nm and total wire radius R =10 nm.

In this chapter we consider cylindrical nanowires of InAs, GaSb and their core-shell nanowires grown in the [001] crystallographic direction. As both InAs and GaSb are narrow band gap materials where $E_G \approx \Delta_{SO}$ [156], we use an 8-band **k.p** model, which simultaneously describes both the conduction and the valence bands. Both InAs and GaSb have a lattice constant of 6.1 $\AA$ [137, 140] and can thus be grown epitaxially, which is the reason why it is a reasonable approximation to neglect strain effects. The band parameters used in this chapter are given in Table 5.1. The valence band offset of the InAs/GaSb heterostructure is taken as $VBO = 0.56$ eV [157, 158, 159]. Together with the band gap values of Table 5.1, this leads to the band alignment of InAs/GaSb core-shell nanowires as shown in Fig. 5.1. In this diagram, as well as in our calculations, the zero of energy is taken at the conduction band minimum of InAs. The InAs conduction band minimum appears below the valence band maximum of GaSb. This implies that electrons will

Table 5.1: Band parameters, and Luttinger and Luttinger-like parameters for InAs and GaSb.

	InAs	GaSb
E_G (eV)	0.37	0.81
E_{GC} (eV)	2.98	2.54
E_P (eV)	19.33	20
Δ (eV)	0.43	0.75
γ_1	19.81	11.8
γ_2	8.46	4.03
γ_3	9.34	5.26
$\tilde{\gamma}_1$	2.3956	3.5695
$\tilde{\gamma}_2$	-0.2472	-0.0852
$\tilde{\gamma}_3$	0.6328	1.1448

move from GaSb to InAs, while free holes will appear in GaSb. The effect of confinement on this charge transfer and thus the band alignment is the topic of this chapter. Due to this broken band gap, which results in electron and hole confinement in different regions of the heterostructure, it becomes essential to use at least an 8-band model which includes the effect of both the conduction and the valence band states.

The Kohn-Luttinger (KL) Hamiltonian [156] ($\mathbb{H}_8$) is constructed to include the conduction band, the valence band and the band offset (VBO and CBO).

$$\mathbb{H}_8 = H^8_{k.p} + VBO + CBO.$$

The effective electron mass (m^*) and Luttinger-like (γ^L's) parameters in the core-shell heterostructure can be written as $m^* = m^*_s + (m^*_c - m^*_s)[1 - \Theta(\rho - R_c)]$ and $\gamma^L = \gamma^L_s + (\gamma^L_c - \gamma^L_s)[1 - \Theta(\rho - R_c)]$, where m^*_s and γ_s are the values in the shell and m^*_c and γ_c the values in the core, Θ is the Heaviside step function, ρ is the radial coordinate, R is the radius of the total wire and R_c is the radius of the core of the core-shell quantum wire.

The envelope wave function for both conduction and valence bands is expanded in a basis of eigenfunctions of a cylinder with radius R:

$$\Psi^\sigma_\zeta(\rho, \phi, z, \sigma) = e^{ik_z} \sum_{m=-M}^{M} \sum_{l=1}^{L} C^\zeta_{ml} \frac{e^{im\phi}}{\sqrt{2\pi}} \frac{\sqrt{2}}{R J_{m+1}(\alpha_{ml})} J_m(\alpha_{ml} \frac{\rho}{R}) \eta_\sigma, \tag{5.1}$$

where J_m is the Bessel function of the first kind and α_{ml} is the lth zero of the corresponding Bessel function J_m ($m = 0, \pm1, \pm2, \pm3, .. \pm M, l = 1, 2, 3..L$), ζ represents different bands in the 8-band model i.e., $\zeta \epsilon \{el\uparrow, el\downarrow, hh\uparrow, lh\uparrow, lh\downarrow, hh\downarrow, so\uparrow, so\downarrow\}$ and R is the radius of the nanowire. Here we have used cylindrical coordinates (ρ, ϕ, z). The coefficients C_{ml} are determined by diagonalizing the $\mathbb{H}_8$ Hamiltonian. The eigen energies form a set of sub-bands numbered by pairs (m, l) and are four fold degenerate with respect to the spin degree of freedom (σ=$\pm$) and the angular momentum ($\pm m$). In Eq.(5.1), the symbol η_σ is the spin part of the wave function. We limited the infinite sum to typically M=4 and L=10, and we checked that this was sufficient for convergence.

Apart from the band structure obtained by diagonalizing the $\mathbb{H}_8$ Hamiltonian, we also calculated the absorption intensity of circular (I_σ) and linear (I_π) polarized light using the Fermi Golden rule [118, 120]. For three different polarizations of light, the integral $I = |\langle f|\vec{p}.\vec{A}|i\rangle|^2$ is calculated as follows:

$$\begin{aligned} I_{\sigma^+} \simeq & |\frac{2}{\sqrt{6}}\langle\Psi^{\sigma}_{el,\uparrow}|\Psi^{\nu}_{h,\frac{3}{2},-\frac{1}{2}}\rangle + \frac{2}{\sqrt{2}}\langle\Psi^{\sigma}_{el,\downarrow}|\Psi^{\nu}_{h,\frac{3}{2},-\frac{3}{2}}\rangle \\ & - \frac{2}{\sqrt{3}}\langle\Psi^{\sigma}_{el,\uparrow}|\Psi^{\nu}_{h,\frac{1}{2},-\frac{1}{2}}\rangle|^2, \end{aligned} \tag{5.2}$$

$$\begin{aligned} I_{\sigma^-} \simeq & |\frac{2}{\sqrt{2}}\langle\Psi^{\sigma}_{el,\uparrow}|\Psi^{\nu}_{h,\frac{3}{2},\frac{3}{2}}\rangle + \frac{2}{\sqrt{6}}\langle\Psi^{\sigma}_{el,\downarrow}|\Psi^{\nu}_{h,\frac{3}{2},\frac{1}{2}}\rangle \\ & + \frac{2}{\sqrt{3}}\langle\Psi^{\sigma}_{el,\downarrow}|\Psi^{\nu}_{h,\frac{1}{2},\frac{1}{2}}\rangle|^2, \end{aligned} \tag{5.3}$$

for circular polarized light and

$$\begin{aligned} I_{\pi} \simeq & |\sqrt{\frac{2}{3}}\langle\Psi^{\sigma}_{el,\downarrow}|\Psi^{\nu}_{h,\frac{3}{2},-\frac{1}{2}}\rangle + \sqrt{\frac{2}{3}}\langle\Psi^{\sigma}_{el,\uparrow}|\Psi^{\nu}_{h,\frac{3}{2},\frac{1}{2}}\rangle \\ & + \sqrt{\frac{1}{3}}\langle\Psi^{\sigma}_{el,\uparrow}|\Psi^{\nu}_{h,\frac{1}{2},\frac{-1}{2}}\rangle + \sqrt{\frac{1}{3}}\langle\Psi^{\sigma}_{el,\downarrow}|\Psi^{\nu}_{h,\frac{1}{2},\frac{1}{2}}\rangle|^2, \end{aligned} \tag{5.4}$$

for linearly polarized light.

We also study the probability density of conduction and valence band ground states $|\Psi(\rho)|^2$ which is given by,

$$\begin{aligned} |\Psi(\rho)|^2 = & |\Psi^{\uparrow}_{EL}(\rho)|^2 + |\Psi^{\downarrow}_{EL}(\rho)|^2 + |\Psi^{\uparrow}_{HH}(\rho)|^2 + |\Psi^{\uparrow}_{LH}(\rho)|^2 \\ & + |\Psi^{\downarrow}_{LH}(\rho)|^2 + |\Psi^{\downarrow}_{HH}(\rho)|^2 + |\Psi^{\uparrow}_{SO}(\rho)|^2 + |\Psi^{\downarrow}_{SO}(\rho)|^2. \end{aligned} \tag{5.5}$$

From the above relations it is clear that the density of a particular state in the 8-band model will have contributions from both electrons and holes,

and depending on the band structure these contributions can be small or large. For example, in the case of large band gap materials like GaAs, the conduction band ground state will mainly consist of the contribution from the electron states, and similarly the valence band ground state will mainly have hole contributions. This will no longer be true for small band gap materials like InAs. We discuss in the next section, the above mentioned properties for type-III core-shell nanowires.

5.2 Results

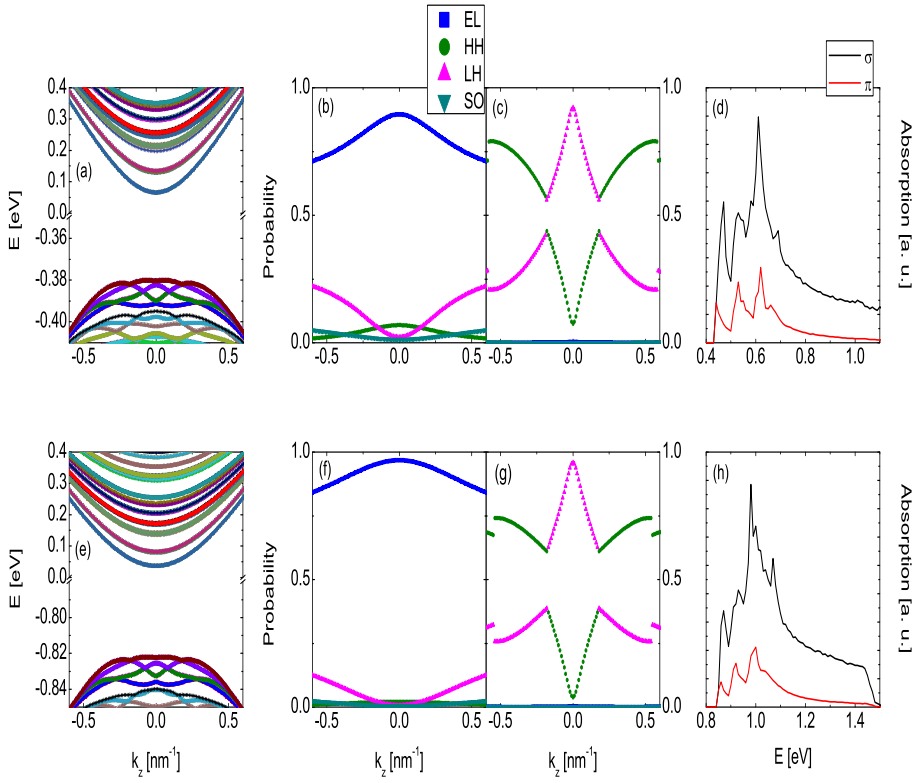

Figure 5.2: (Color online) Band structure ((a) and (e)), the spinor distribution of conduction ((b) and (f)) and valence band ground states ((c) and (g)) and the optical absorption spectra ((d) and (h)) for InAs and GaSb single material nanowires, respectively with radius R=10 nm.

In this section, we present our results for InAs/GaSb nanowires which have a type-III band alignment. The electronic band structure, the density of conduction and valence band ground states at the Γ point and the absorption spectra of the electrons and the holes are presented for each case. We first discuss our results for nanowires consisting of a single material which will be followed by our results for the core-shell nanowires.

The single material nanowires discussed in this chapter have radius $R =$ 10 nm and the core-shell nanowires have a core radius $R_c = 5$ nm and total radius $R = 10$ nm.

Fig. 5.2 gives the band structure, the spinor distribution of both the conduction and the valence band ground states and the absorption spectra for InAs and GaSb nanowires, respectively. Here the zero of energy is taken at the conduction band minimum of InAs. The results for the valence band structure are shown in Figs. 5.2(a) and (e). Notice that the ground state has a camel back structure for both InAs and GaSb, which results in a peak in the onset of the absorption spectrum. The discontinuities in the spinor distribution of the valence band ground state in Figs. 5.2(c) and (g) are due to the crossings in the corresponding valence band ground state (see Figs. 5.2(a) and (e)). Notice that linear polarized light has always a lower intensity as compared to circular polarized light. This could be understood from the spinor distribution of the valence band ground state and the relations for calculating the absorption intensity (Eqs. (5.3) and (5.4)).

The spinor distribution of the valence band ground state shows that the light hole (LH) has the maximum contribution close to the zone center, and decreases as we move away from it, whereas the heavy hole (HH) contribution slowly increases as we move away from the zone center. A look at the absorption intensity relations (Eqs. (5.3) and (5.4)) show that the intensity due to circular polarized light ($I_\sigma = I_{\sigma+} + I_{\sigma-}$), results from the transitions HH→El, LH→El and SO→El, while, for linear polarized light (I_π) only the transitions LH→El and SO→El contribute. Thus I_σ includes the extra transition HH→El. Furthermore, the lower energy transitions are dominated by LH→El, while the higher energy transitions, which are away from the zone center, are dominated by HH→El. Hence for higher energies there appear many more peaks in I_σ, that are absent in I_π.

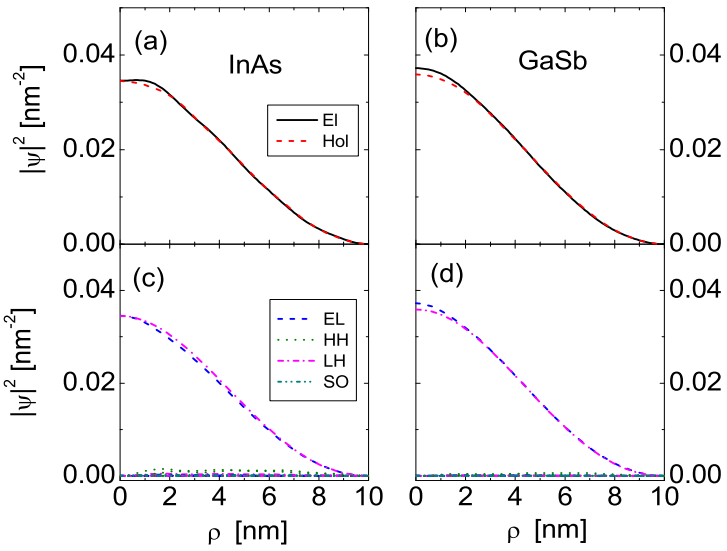

Figure 5.3: (Color online) Density of conduction band ground state (black solid lines) and valence band ground state (red solid lines) at k_z=0 along with the contribution from various states, electrons (dashed), heavy holes (dotted), light holes (dash dot) and split-off (dash dot dot)) for the ground state of InAs ((a) and (b)) and GaSb ((c) and (d)) nanowires with radius R=10 nm.

The spinor distribution of the valence band ground state (Figs. 5.2(c) and (g)) shows that at k_z=0, the light hole gives the largest contribution for both InAs and GaSb. But the spinor distribution of the conduction band ground state (Figs. 5.2(b) and (f)) shows that at k_z=0, the heavy hole contributes significantly in the case of InAs which is absent for the larger band gap material GaSb. This can also be seen in the density of the conduction and the valence band ground states in Fig. 5.3, where the density of the conduction band ground state of InAs (see Fig. 5.3(a)) shows a small dip near ρ=0. A look at the individual components of this density (see Fig. 5.3(c)) shows that this is due to the contribution of the heavy holes. This increased influence of holes in the conduction band is attributed to the small band gap of InAs, which is 370 meV.

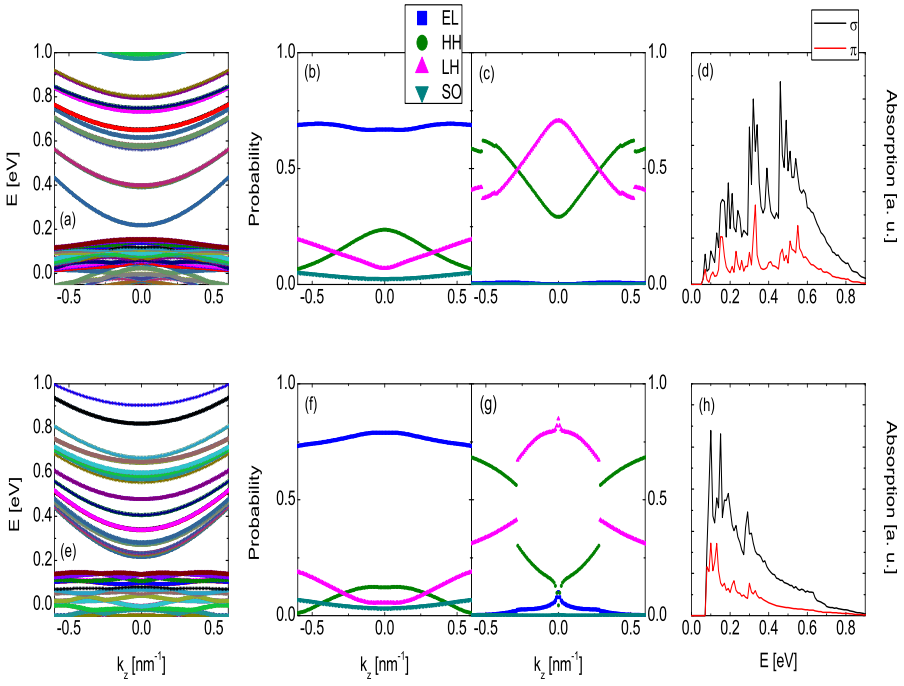

Figure 5.4: (Color online) Band structure ((a) and (e)), the spinor distribution of conduction ((b) and (f)) and valence band ground states ((c) and (g)) and the optical absorption spectra ((d) and (h)) for InAs/GaSb and GaSb/InAs core-shell nanowires, respectively with core radius R_c=5 nm and total wire radius R=10 nm.

We now present our results for the InAs/GaSb core-shell nanowires. As a first example we consider a nanowire with core radius R_c=5 nm and total radius R=10 nm. Here the zero of energy is taken at the conduction band minimum of InAs. The band structure of these core-shell nanowires with InAs in the core and GaSb in the core are shown in Figs. 5.4(a) and (e), respectively. Despite the band overlap of the bulk materials, the band structure of both these InAs/GaSb and GaSb/InAs core-shell nanowires show an effective band gap of 65 meV and 78 meV, respectively. The spinor distribution of the conduction band ground states in both cases show an increase in the heavy hole contribution at k_z=0, when compared to the results for the pure wires. Also, the spinor distribution of the valence band shows a small contribution of the electron states for nanowires with GaSb in the core.

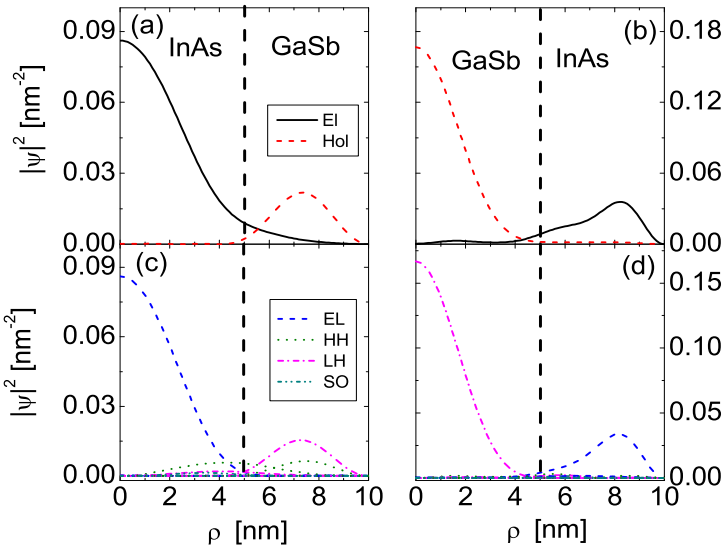

Figure 5.5: (Color online) Density of conduction band ground state (black solid lines) and valence band ground state (red solid lines) at k_z=0 along with the contribution from various states (electron (dashed), heavy holes (dotted), light holes (dash dot) and split-off (dash dot dot)) for the ground state of InAs/GaSb ((a) and (b)) and GaSb/InAs ((c) and (d)) core-shell nanowires with radius R_c=5 nm and R=10 nm.

For the absorption spectra, the reduced effective band gaps result in absorption at low energies (Figs. 5.4(d) and (h)). Absorption peak intensities in the case of nanowires with InAs in the core are reduced because the conduction band state has an increased hole contribution. But at the same time, nanowires with GaSb in the core show an increase in the absorption peak intensity. The reason for this is that the valence band states in this case are spread over large k_z values which results in an increase of equal energy transitions. Finally, we show the probability density of the conduction and the valence band ground states for the core-shell nanowires (Figs. 5.5(a) and (b)) along with their individual components (Figs. 5.5(c) and (d)). The conduction and the valence band ground state densities are respectively confined in the InAs and GaSb regions, which is due to the particular band alignment

(see Fig. 5.1) in these heterostructures. Although there is an increase in the influence of the hole states in the conduction band density (see Fig. 5.5(c)), the electron states are still the major contributors and hence we can still label this density as electron density. Similarly, the valence band ground state density can also be labeled as the hole density.

5.2.1 Electron-hole hybridization

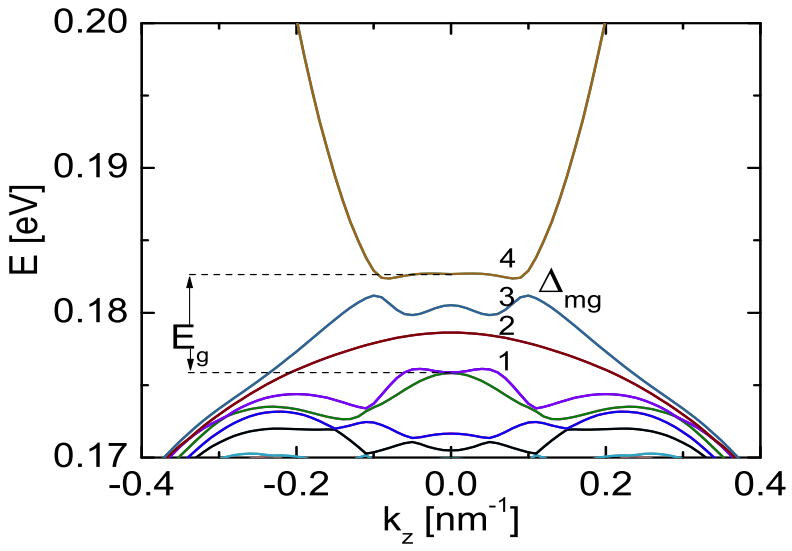

Figure 5.6: (Color online) Band structure of InAs/GaSb core-shell nanowire with R_c=6.2 nm and R=18 nm.

The effective band gaps can be varied by changing the relative size of the InAs and GaSb regions. Even a negative band gap can be obtained, i.e., when the lowest conduction band state is below the highest valence band state. In this configuration a hybridization between the conduction band states and the valence band states will occur leading to a semi-metallic behavior [160]. To illustrate this hybridization, we present the band structure of one such hybrid system obtained from an InAs/GaSb core-shell nanowire with core radius R_c=6.2 nm and total radius R=18 nm (see Fig. 5.6). We have labeled the different states involved in the hybridization from 1 to 4, where '1' is the lowest energy state with a large electron contribution, i.e. the conduction band minimum and '4' is the conduction band state which

has a hole-like character, i.e. the valence band maximum. Thus we have a negative band gap of E_g=-6.8 meV. The negative band gap can result in ambipolar transport as was recently observed in Ref. [155] and in a quantum spin Hall (QSH) insulator phase previously observed in HgTe/CdTe [161, 162] and InAs/GaSb [163] quantum wells. But Fig. 5.6 also shows that a new hybridization gap (or minigap) Δ_{mg}=1.3 meV opens up for $k_z \neq 0$. Thus we now have a new gap opening in a semi-metallic band dispersion, which results in a bulk insulating behavior for the system.

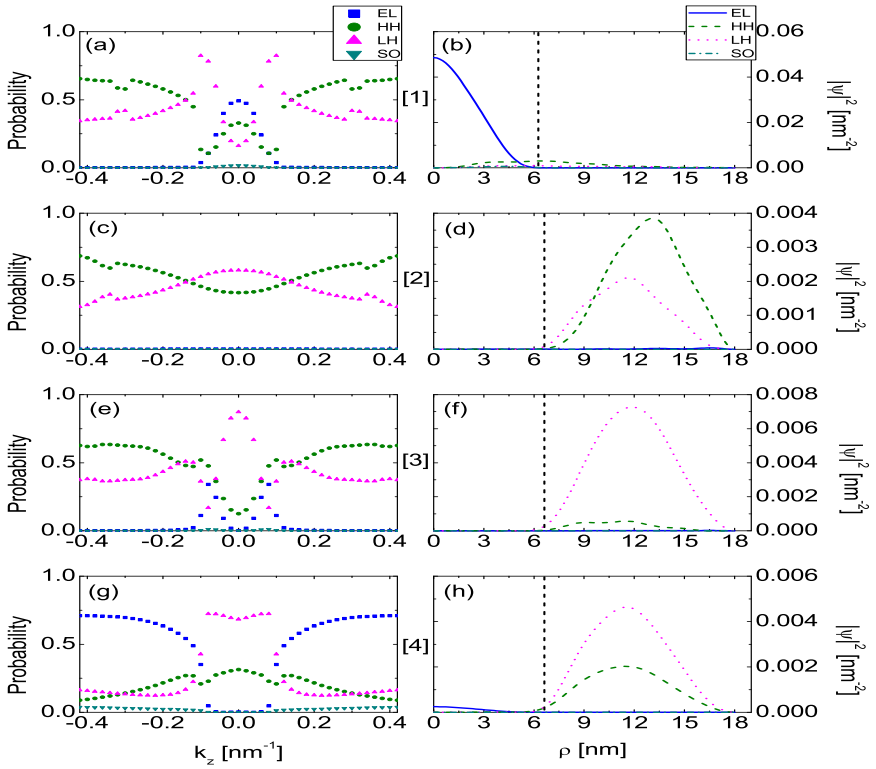

Figure 5.7: (Color online) Spinor distribution and particle probability at k_z=0 of states 1, 2, 3 and 4 shown in Fig. 5.6 for InAs/GaSb core-shell nanowire with R_c=6.2 nm and R=18 nm.

In Fig. 5.7, we give the spinor distribution ((a), (c), (e) and (g)) along with the particle probability density at k_z=0 ((b), (d), (f) and (h)) of the

states 1 to 4. The spinor distribution shows the contribution of the different components at different k_z values. It shows that the state '1' exhibits a maximum electron contribution, while state '4' has a maximum hole contribution at $k_z = 0$. Thus state '4' behaves as a hole-like state for $0 < k_z < 0.1$ nm^{-1} and as an electron-like state for $k_z > 0.1$ nm^{-1}. Similarly, state '4' behaves as an electron-like state for $0 < k_z < 0.05$ nm^{-1} and as a hole-like state for $k_z > 0.05$ nm^{-1}. This can also be observed from the corresponding probability densities in Figs. 5.7(b), (d), (f) and (h). The intermediate states '2' and '3' have maximum hole contribution around k_z=0. Also, it can be seen that the state '4' (Fig. 5.7(g)) which is the valence band maximum and state '3' (Fig. 5.7(e)) anti-cross at $k_z \simeq 0.1$ nm^{-1}. This anti-crossing is the origin of the minigap Δ_{mg}. From the spinor distribution in Figs. 5.7(e) and (g) one can see that the electron and hole contributions are equal at this anti-crossing.

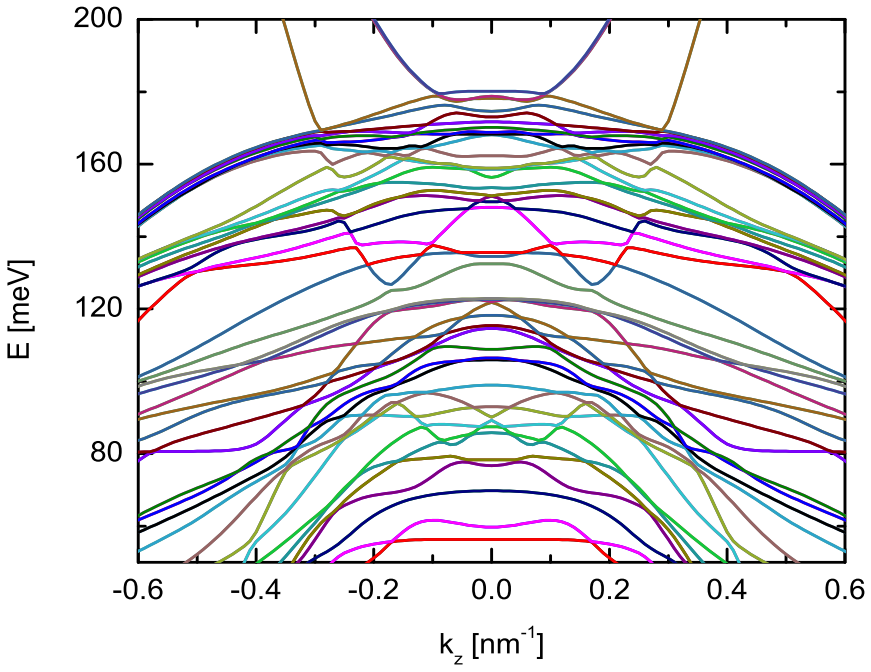

Figure 5.8: (Color online) Band structure of an InAs/GaSb core-shell nanowire with R_c=10 nm and R=20 nm.

A minigap is not always present in case of a band overlap as illustrated in Fig. 5.8 where we show the band structure of an InAs/GaSb core-shell

nanowire with R_c=10 nm and R=20 nm. Here we can see that multiple conduction bands penetrate into the valence band states. In this case there will be multiple hybridization gaps opening at $k_z \neq 0$, but not at the same energy values. So, no real minigap Δ_{mg} is present in the system. Thus, a real minigap is only present when a single conduction band overlaps with the valence band states at k_z=0.

In summary for $E_g > 0$, the InAs/GaSb core-shell nanowire behaves as a semiconductor and for $E_g < 0$, it behaves as a semi-metal. But for $E_g \lesssim 0$, the conductivity of the nanowire depends on both the effective bandgap E_g and the minigap Δ_{mg} values [164].

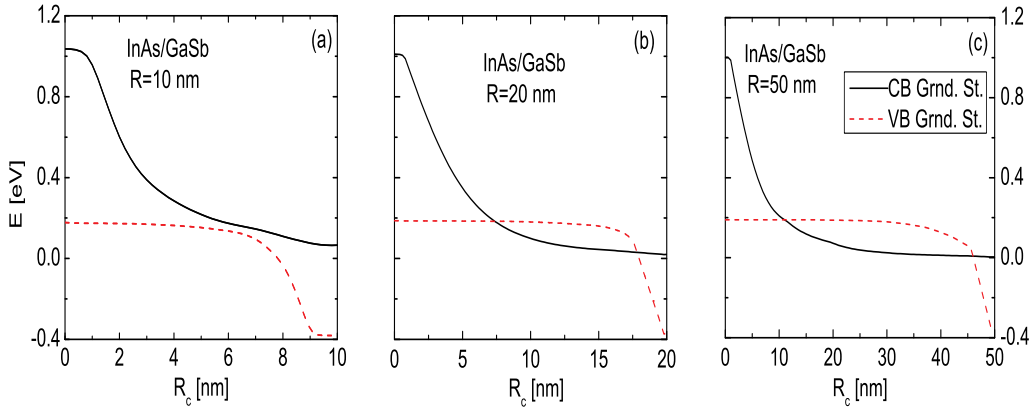

Figure 5.9: (Color online) Conduction band minimum and valence band maximum at k_z=0 for InAs/GaSb core-shell wire as function of the core radius R_c with fixed total radius R=10 nm (a), R=20 nm (b) and R=50 nm (c).

Let us now study the ground state of the conduction and the valence bands for InAs/GaSb core-shell nanowires by varying the core radius R_c and the total radius R. Fig. 5.9 shows the energy of the valence and the conduction band ground states at k_z=0 for the InAs/GaSb core-shell nanowires as a function of the core radius R_c, for fixed total radius R=10 nm, R=20 nm and R=50 nm. Here the conduction band ground state (solid black line) and valence band ground state (dashed red line) are shown, for the three different nanowires. In the case of nanowires with R=10 nm (see Fig. 5.9(a)) the effective band gap is always positive and hence there are no hybrid states. This is due to the quantum confinement effect which increases the effective band gap as the size is reduced (i.e., for small R). Note that there is hybridization

for nanowires with radius R=20 nm when 6 nm < R_c <16 nm and R=50 nm when 10 nm < R_c <45 nm (see Figs. 5.9(b) and (c)). In this region of hybridization the effective band gap is negative. Thus the negative gap (E_g) increases with an increase in R_c and reaches a maximum and then decreases, as we increase the size of InAs in these InAs/GaSb core-shell nanowires. Also it is important to highlight that there is a minigap Δ_{mg}, when $E_g \lesssim 0$, where only a single conduction band penetrates into the valence band. This occurs just at the crossing of the conduction and the valence band ground states in Figs. 5.9(b) and (c).

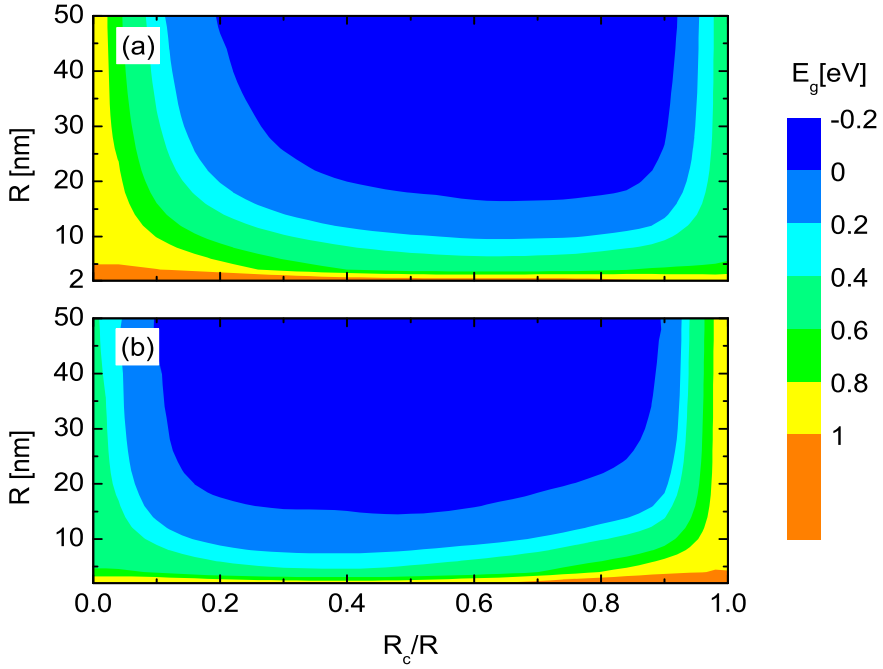

Figure 5.10: (Color online) Contour plot of the effective band gap E_g at k_z=0 for (a) InAs/GaSb and (b) GaSb/InAs core-shell wires in the core radius R_c/R and total radius R plane.

These results can be summarized in a phase diagram in Fig. 5.10, showing the effective band gap E_g as a function of total radius R and R_c/R for InAs/GaSb and GaSb/InAs core-shell nanowires. We found that a positive band gap is always obtained for $R < 14$ nm, both for the InAs/GaSb as well as the GaSb/InAs core-shell nanowires, irrespective of the core radius R_c.

For $R > 14$ nm, a minigap and a negative effective bandgap can be obtained. Thus by varying the radial size of the InAs/GaSb nanowires we can modify the effective band gap E_g and also open a minigap Δ_{mg}.

As cited in the beginning of this chapter, in Ref. [155] ambipolar transport was demonstrated in GaSb/InAs(Sb) core-shell nanowires, starting from a threshold thickness of about 5 nm of the InAs(Sb) shell. We expect the occurrence of ambipolar transport when $E_g = 0$. For a wire with a GaSb core radius of $R_c = 25$ nm and InAs shell thickness of 5 nm, we find $E_g \simeq -0.05$ eV. This onset of the closure of the bandgap is indeed in good agreement with the experimental observation in Ref. [155].

5.3 Summary and conclusions

In this chapter we have assumed that the interface between InAs and GaSb is abrupt and have given a quantitative description of the various electronic and optical properties of these type-III systems. A qualitative description however should include band bending due to charge transfer at the interface, nevertheless our model has successfully identified some of the unique properties of these type-III nanowires.

In this chapter we have presented different properties of the InAs/GaSb type-III nanowires. Due to the broken bandgap observed in these structures, the electrons and the holes confine in different regions. Apart from this we have also obtained hybridization of the electron and the hole states, by varying the radius of the total wire (R) and the core region (R_c) of the core-shell nanowires. As the conduction band minimum lies below the valence band maximum, a negative effective bandgap $E_g < 0$ is observed in these systems. Thus, these hybridized systems have a semi-metallic behavior, which could be used in developing novel electronic devices. We have also observed a small minigap Δ_{mg} opening away from the zone center. This minigap can be observed only when a single conduction band overlaps with the valence band states which will influence the conductivity of the system.

Chapter 6

Electronic structure of semiconductor nanowires in a magnetic field

In this chapter we study the electronic and the optical properties of single material and core-shell nanowires under the influence of a uniform magnetic field directed parallel to the wire axis. Results for single material GaAs, $Al_xGa_{1-x}As$ and $(Al_xGa_{1-x})_{0.51}In_{0.49}P$ and for core-shell nanowires with GaAs as one of the materials are presented in this chapter. These core-shell nanowires have a type-I band alignment. Here we use the 8-band **k.p** model [88] which includes the effect of both the conduction and the valence band states and modify the Hamiltonian to include the effect of a magnetic field.

This chapter is organized in the following manner: in the next section we give the theory used in this chapter, which is followed by our results for both single material and core-shell nanowires and finally we present our summary and conclusions.

6.1 Theory

In this chapter we use the 8-band **k.p** method [88, 156] to describe the electronic structure of core-shell nanowires. We have to make appropriate modifications to the Hamiltonian to include the effect of the magnetic field.

The Hamiltonian can be modified by changing the wave vector. The wave vector in the absence of a magnetic field can be written as,

$$k_\alpha = \frac{1}{i}\frac{\partial}{\partial x_\alpha}, \tag{6.1}$$

where the index α stands for x, y and z. Also,

$$k_\pm = k_x + ik_y, \tag{6.2}$$

and thus

$$k_\pm^0 = -ie^{\pm i\varphi}(\frac{\partial}{\partial\rho} \pm \frac{i}{\rho}\frac{\partial}{\partial\varphi}), \tag{6.3}$$

in cylindrical coordinates.

When a magnetic field is applied, the wave vector is modified as follows,

$$k_\alpha = \frac{1}{i}\frac{\partial}{\partial x_\alpha} + \frac{e}{\hbar}A_\alpha. \tag{6.4}$$

In the present chapter we consider the magnetic field along the wire, i.e. in the z-direction. Accordingly, we can choose the symmetric gauge in cylindrical coordinates so that the vector potential is given by $\mathbf{A}$=(0,A_φ,0) and A_φ=$\frac{\rho B}{2}$. Thus,

$$k_\pm = e^{\pm i\varphi}[-i(\frac{\partial}{\partial\rho} \pm \frac{i}{\rho}\frac{\partial}{\partial\varphi}) \pm i\frac{e}{\hbar}A_\varphi], \tag{6.5}$$

$$k_\pm = k_\pm^0 + k_\pm^B, \tag{6.6}$$

where

$$k_\pm^B = \pm i\frac{\rho}{2l_B^2}e^{\pm i\varphi}, \tag{6.7}$$

with $l_B = (\frac{\hbar}{eB_z})^{\frac{1}{2}}$ the magnetic length.

Thus the total Hamiltonian is given by [96],

$$H_{k_\pm}^B = H(k_\pm^0) + H(k_\pm^B) + g\mu_B\kappa B, \tag{6.8}$$

where $H(k_\pm^0)$ is the 8-band Kohn-Luttinger Hamiltonian (see subsection 2.3.2), $H(k_\pm^B)$ is the magnetic field term and $g\mu_B\kappa B$ gives the zeeman splitting term.

Here $\kappa = \pm 1$ for electrons, $\kappa = \pm 3$ for heavy holes, $\kappa = \pm 1$ for light holes, $\kappa = \pm 2$ for split-off band and $\pm\sqrt{2}$ for A the coupling term between split-off band and light holes (see Eq. (C.6)) and μ_B is the Bohr magneton.
Landé's g factor for the conduction band [111] is

$$g_{CB} = 2 - \frac{2}{3}\frac{E_G\Delta}{E_G(E_G+\Delta)}, \tag{6.9}$$

and for the valence band [113, 114]:

$$g_{VB} = \gamma_3 + \frac{2}{3}\gamma_2 - \frac{1}{3}\gamma_1 - \frac{2}{3}. \tag{6.10}$$

The envelope wave function for both conduction and valence bands is expanded in a basis of eigenfunctions of a cylinder with radius R in the absence of magnetic field (i.e. $B = 0$):

$$\Psi(\rho,\phi,z) = e^{ik_z z}\sum_{m=-M}^{M}\sum_{l=1}^{L} C_{ml}\frac{e^{im\phi}}{\sqrt{2\pi}}\frac{\sqrt{2}}{RJ_{m+1}(\alpha_{ml})}J_m(\alpha_{ml}\frac{\rho}{R}), \tag{6.11}$$

where J_m is the Bessel function of the first kind and α_{ml} is the lth zero of the corresponding Bessel function J_m ($m = 0, \pm1, \pm2, \pm3, .. \pm M, l = 1, 2, 3..L$) and R is the radius of the nanowire. The coefficients C_{ml} are determined by diagonalizing the $H^B_{k_\pm}$ Hamiltonian. We can approximately use the above defined envelope function even under the influence of a non-zero magnetic field.

Using the above defined envelope function and the Hamiltonian in Eq.(6.8) (see Appendix C for complete matrix elements), the energy of a state has the following functional form,

$$E = \frac{\hbar^2}{2m_0}[\beta_1(\frac{\alpha_{ml}}{R})^2 + \beta_2 k_z^2 + \beta_3(\frac{\alpha_{ml}}{R})B + \beta_4 B^2] + g\mu_B\kappa B, \tag{6.12}$$

where m_0 is the bare electron mass, β_1 corresponds to the energy in the absence of magnetic field due to the confinement potential of the wire, while β_3 and β_4 are the paramagnetic and diamagnetic contributions to the energy. This energy has contributions from all the eight bands that are included in the Hamiltonian $H^B_{k_\pm}$.

In the next section we present our results for both single material and core-shell nanowires.

Table 6.1: Band parameters, Luttinger and Luttinger-like parameters for GaAs, $Al_{0.4}Ga_{0.6}As$ (AlGaAs), $Al_{0.51}In_{0.49}P$ (AlInP), $Ga_{0.51}In_{0.49}P$ (GaInP) and $(Al_{0.5}Ga_{0.5})_{0.51}In_{0.49}P$ (AlGaInP) (m_0 is the bare electron mass).

	GaAs [86]	AlGaAs [86]	AlInP [116]	GaInP [116]	AlGaInP [116]
E_G (eV)	1.519	2.1634	2.6671	1.9971	2.3321
E_P (eV)	23.81	22.726	12.2679	15.9335	14.1007
Δ (eV)	0.341	0.3166	0.1322	0.0898	0.111
γ_1	7.05	5.1217	4.2592	4.6296	4.4296
γ_2	2.35	1.4347	1.1203	1.0562	1.0945
γ_3	3	2.0971	1.7281	1.9997	1.933
$\tilde{\gamma}_1$	1.8251	1.6201	2.7259	1.9701	2.4141
$\tilde{\gamma}_2$	-0.2625	-0.3161	0.3536	-0.2736	0.0868
$\tilde{\gamma}_3$	0.3875	0.3463	0.9615	0.67	0.9252
κ_{CB}	0.0842	1.106	1.8552	1.7711	1.8169
κ_{VB}	-1.0625	-1.0711	-0.3781	-0.8358	-0.4883
$\frac{m_e}{m_0}$	0.067	0.1002	0.0962	0.0925	0.0943

6.2 Results

In this section we present our results for nanowires with a uniform magnetic field applied along the growth direction, which in our case is the [001] crystallographic direction. The potential outside the nanowire is assumed to be infinite, hence the charge carriers are confined completely inside the wire. The maximum applied magnetic field is taken as $B = 25$ Tesla, which is within the practical magnetic field limits attainable in most of the physical laboratories. The radius of single-material nanowires is chosen to be $R = 20$ nm and for the core-shell nanowires the core radius and total radius are chosen as $R_c = 10$ nm and $R = 20$ nm respectively. The choice of radii are made to depict the influence of the quantum confinement effects in these systems.

The band parameters of various materials used in this chapter are given in Table. 6.1 and the band offset values for different core-shell nanowires with type-I band alignment are given in Table. 6.2. We first present the electronic structure results for the single material nanowires followed by the results for the core-shell nanowires.

Table 6.2: Heterostructure band off-set parameters.

Heterostructure	CBO [eV]	VBO [eV]
GaAs/$Al_xGa_{1-x}As$ [86]	$0.870x$	$0.570x$
GaAs/$Al_{0.4}Ga_{0.6}As$	0.348	0.228
GaAs/$(Al_xGa_{1-x})_{0.51}In_{0.49}P$ [116]	$0.4303x + 0.1698$	$0.2397x + 0.3083$
GaAs/$Ga_{0.51}In_{0.49}P$	0.1698	0.3083
GaAs/$(Al_{0.5}Ga_{0.5})_{0.51}In_{0.49}P$	0.385	0.4282
GaAs/$Al_{0.51}In_{0.49}P$	0.6001	0.548

6.3 Single material nanowires in magnetic field

From Eq.(6.12) it is clear that the energy of any particular state in the magnetic field depends on various factors. Among these factors, the quantum confinement energy, the paramagnetic and the diamagnetic terms have the major contribution. Also as we are using an 8-band model, each energy level is doubly degenerate in the absence of a magnetic field ($B = 0$) and every energy level has contributions from all the 8 components (EL↑, EL↓, HH↑, LH↑, LH↓, HH↓, SO↑, SO↓). In the absence of a magnetic field the conduction band ground state energy is degenerate with major contributions from EL↑ and EL↓. This degeneracy will be lifted with the application of a magnetic field. In chapter 4, we have already shown that in the absence of any magnetic field, the various contributions to the valence band ground state depend on the bandgap (E_G), the split-off energy (Δ) and the Kane's energy (E_P) values. Thus we expect that the values of these parameters would also influence the various energy levels in the presence of a magnetic field. So, let us first understand how these factors influence the conduction and the valence band energies in a single material nanowire at the Γ point under the influence of a uniform magnetic field.

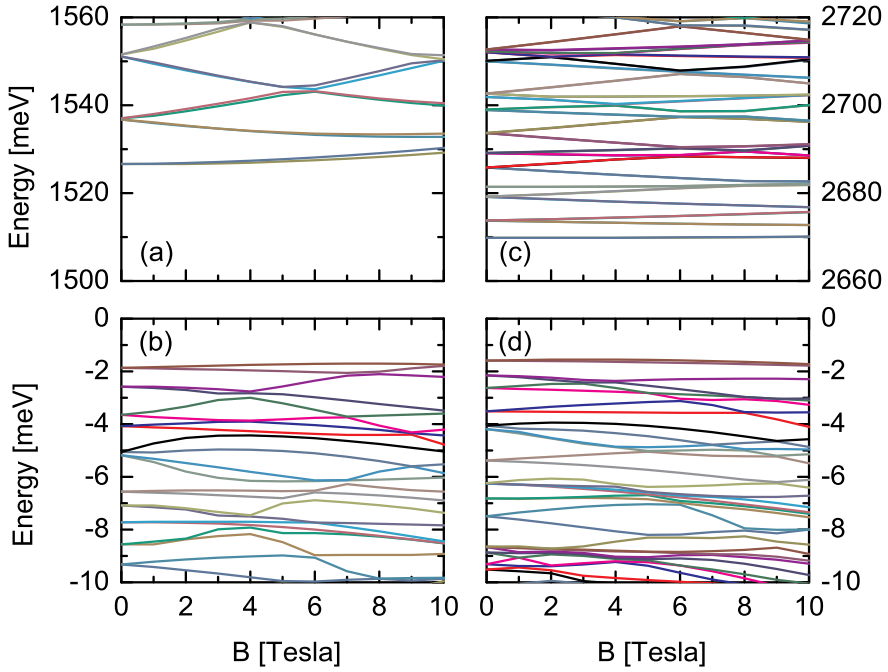

Figure 6.1: The conduction (a and b) and the valence (c and d) band energy at $k_z = 0$ vs the magnetic field B for GaAs (a and c) and $Al_{0.51}In_{0.49}P$ (b and d) nanowires of radius R=20 nm respectively, using the 8-band **k.p** model.

In Fig. 6.1(a) and (b), we show the energy dispersion (at $k_z = 0$) with the increase in the magnetic field for a GaAs nanowire ($E_G = 1.519$ eV and $E_P = 23.81$ eV) of radius $R = 20$ nm. Notice that the degeneracy in the conduction band ground state is lifted even at very small magnetic field values and the energy difference between these degenerate states increases with the increase in the magnetic field strength. But in the case of a $Al_{0.51}In_{0.49}P$ nanowire (Fig. 6.1(c) and (d)), this behavior is not seen for smaller magnetic field values. The reason for this is the larger band gap $E_G = 2.667$ eV and the smaller Kane's energy $E_P = 12.27$ eV values for the $Al_{0.51}In_{0.49}P$ nanowire. This shows that the influence of magnetic field is higher for materials with smaller E_G and larger E_P values. Similar explanation can be given for the valence band (Fig. 6.1(b) and (d)), but due to the band mixing, the valence band results are more complex to explain. Thus we can see that the magnetic field dependence of energy is characteristic of the material.

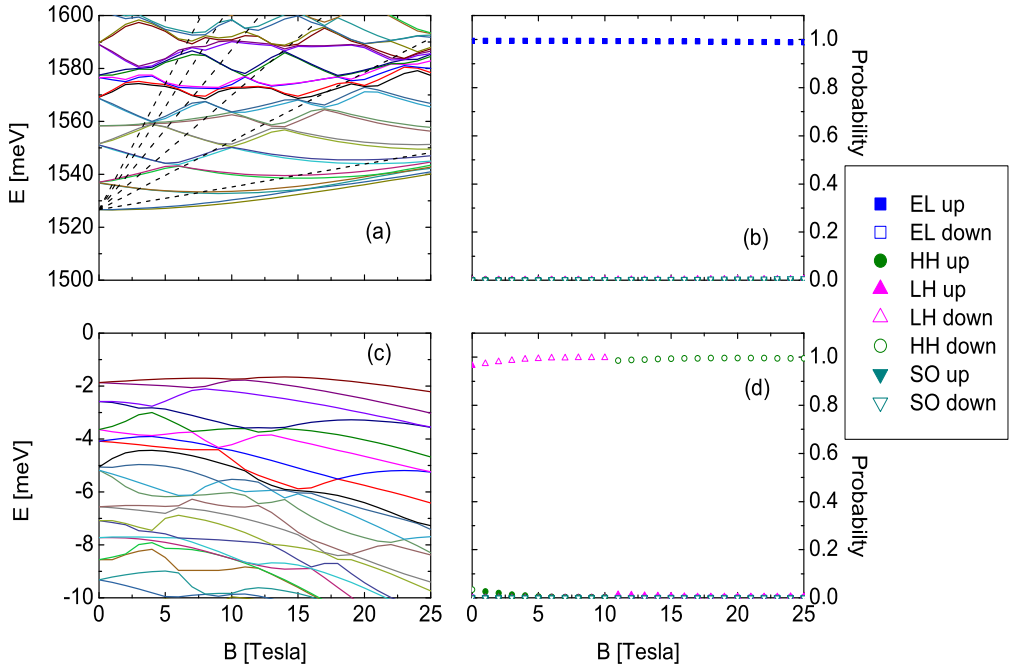

Figure 6.2: The conduction (a) and the valence (d) band energy at $k_z = 0$ vs the magnetic field B for GaAs nanowires of radius R=20 nm respectively, using the 8-band **k.p** model. The dashed lines show Landau levels in a quantum well of the same width as the diameter of the wire. Spinor distribution of both conduction (b and c) and valence band (e and f) ground states.

Let us now look at the energy dependence on the magnetic field in detail. In Fig. 6.2(a) we give the conduction band energy (at $k_z = 0$) as the magnetic field B is increased from 0 to 25 Tesla for a GaAs nanowire of radius $R = 20$ nm. We can see that for a non-zero magnetic field value, the energy levels move up or move down in energy and we note that the conduction band energy dispersion resembles the Fock-Darwin levels in quantum dots. They also form Landau bands for high magnetic fields similar to the quantum dot systems. We know that the energy of a single band quantum dot system with a confinement energy $U(r) = \frac{1}{2}m^*\omega_0 r^2$ is given by [166],

$$E = (2n + |m|+1)\hbar\Omega - \frac{m\hbar\omega_c}{2}, \tag{6.13}$$

where $\Omega^2 = (\frac{\omega_c^2}{4} + \omega_0^2)$ and n, m, $\omega_c = \frac{eB}{m^*}$ and m^* represent the radial quantum number, the azimuthal angular momentum quantum number, the cyclotron frequency and the effective mass respectively. The states with such a behavior are known as Fock-Darwin states and are defined in terms of the angular momentum quantum number m. This kind of description is only valid for single band models. In the present case we use an 8-band **k.p** model which includes band mixing and hence such a description of energy in terms of Fock-Darwin states for the conduction band using the angular momentum quantum number m cannot be made. However, the energy levels of nanowires in a multiband model behave similar to the ones in a single band model as shown in Fig. 6.2(a). Therefore we can call these states Fock-Darwin *like* states and talk about angular momentum *like* transitions for the excited states. This description is only valid for the conduction band states. We can also see that with the increase in the magnetic field values, the energy dependence on magnetic field changes from a quadratic (diamagnetic) to a linear (paramagnetic) behavior (see Eq. 6.12). As stated before the degeneracy of states is lifted with the application of the magnetic field and now each state is split into two different states with slightly different energies. We also show the valence band energy evolution with the increase in the magnetic field in Fig. 6.2 (c) which is more complex to explain.

In Fig. 6.2 we also show the spinor distribution of the conduction (Fig. 6.2 (b)) and the valence band (Fig. 6.2 (d)) ground states at $k_z = 0$ with the increase in the magnetic field. We can see that the crossings observed in the valence band ground state (Fig. 6.2 (c)) are due to the flip in the contributions of heavy holes and light holes (Fig. 6.2 (d)). On the other hand the electron ground state has maximum contribution from the spin up electrons. Thus we can see that with the increase in the magnetic field the contribution of various components to the valence band ground state also changes.

We now look at the spinor distribution of the valence band ground state for different k_z and magnetic field values. In Fig. 6.3 we give the spinor distribution of the valence band ground state of a GaAs nanowire with radius $R = 20$ nm. We can see that for $B = 0$ Tesla (see Fig. 6.3 (a)) the highest contribution is due to LH$\uparrow$ for $k_z \leq 0.1\ nm^{-1}$ and due to both HH$\uparrow$ and HH$\downarrow$ for $k_z > 0.1\ nm^{-1}$. We can also see that for non-zero magnetic field values the highest contribution for small k_z values is due to LH$\downarrow$ and HH$\downarrow$, but for higher k_z values the highest contribution is only due to HH$\uparrow$. The k_z value corresponding to this change of contribution is identified by a dashed line in Figs. 6.3 (b), (c) and (d). This change in the highest contribution will be reflected in the absorption spectra.

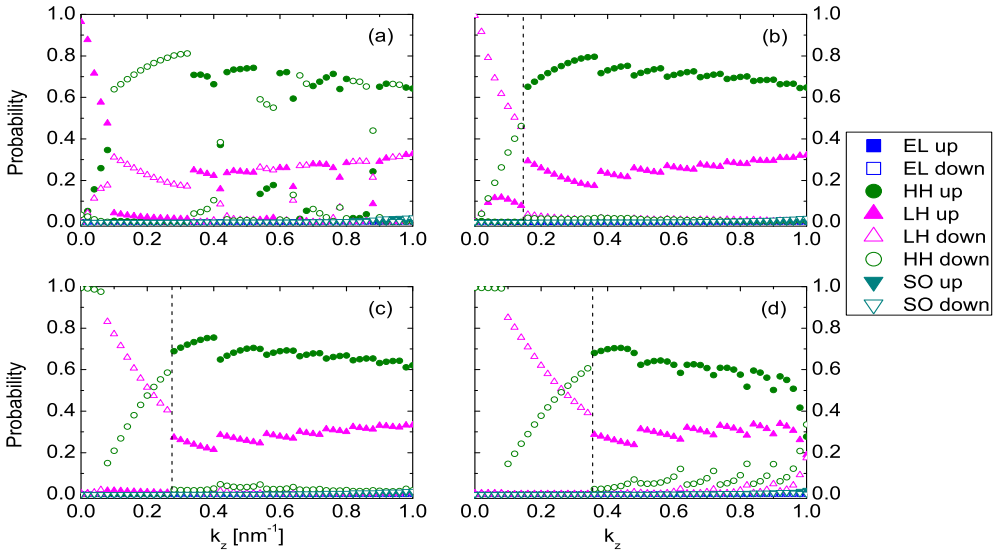

Figure 6.3: Spinor distribution of valence band ground state for a GaAs nanowire of radius R=20 nm for different k_z values with the application of magnetic field B=0 T (a), 5 T (b), 15 T (c) and 25 T (d) respectively.

In Fig. 6.4 we present the absorption spectra due to left and right circular polarized light for different magnetic field values. Note that the absorption results include transitions between different conduction and valence band states for different k_z values. We observe that the effective bandgap of the system increases with the increase of the magnetic field ($E_G(B = 25$ T)-$E_G(B = 0$ T)$\simeq 15$ meV), as can be seen from our energy ($k_z = 0$) vs B results in Fig. 6.2(a). Also, as we move away from the Γ point ($k_z = 0$), the energy of the allowed transitions increases. Fig 6.4(a) shows that at $B = 0$ Tesla, the absorption spectra due to both circular polarized lights are identical which means that the ground state has contributions from electrons of both spins as they have degenerate energies. With the increase in the magnetic field the degeneracy in energy is lifted and we can see that the difference between the absorption due to left and right circular polarized light increases and can be attributed to the change in the various allowed transitions (see Eqs. 3.24 and 3.25 in chapter 3). The change in the absorption spectra for higher energy transitions (for $E_G > 1.65$ eV) for $B \neq 0$ Tesla correspond to the flip in the spinor distribution of the valence band ground state away from the Γ point (see Figs. 6.3 (b), (c) and (d)). Thus we can say that the presence of a magnetic field effects the absorption spectra due to circular polarized light.

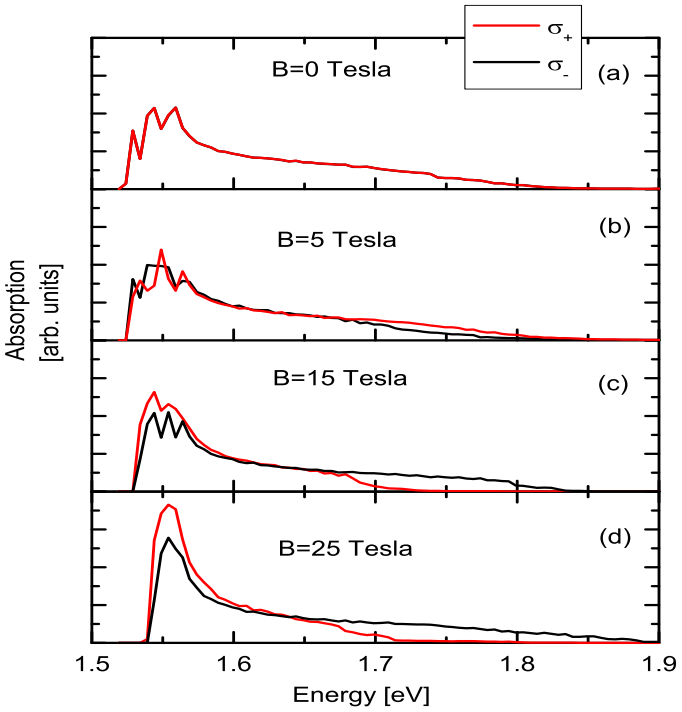

Figure 6.4: The absorption intensity for a GaAs nanowire of radius R=20 nm, due to both left and right circular polarized light, with the application of magnetic field B=0 T (a), 5 T (b), 15 T (c) and 25 T (d) respectively.

So far we have discussed the results for single material nanowires, where the wavefunction of both electrons and holes are confined in the wire as the potential outside the wire is infinite. We can introduce an additional confining potential by choosing core-shell nanowires where the core and the shell are separated by a potential difference (band offset). This potential difference is due to the difference in the relative arrangement of bands in core and shell regions. Thus the study of core-shell nanowires in the presence of a uniform magnetic field can give rise to some new features which may not be observed in the case of single material nanowires. This has motivated us to study the effect of a magnetic field on the properties of core-shell nanowires and will be discussed in the next section.

6.4 Core-shell nanowires in a magnetic field

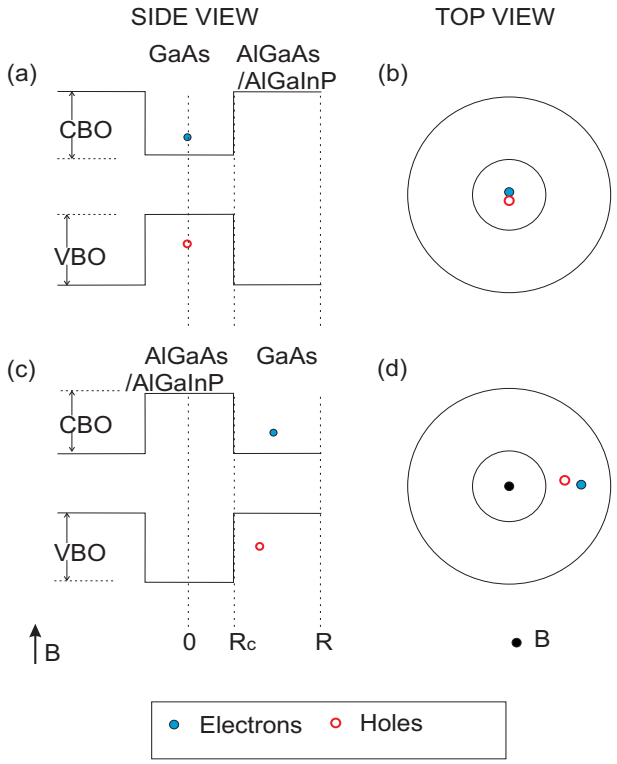

Figure 6.5: The band alignment of GaAs/$Al_xGa_{1-x}As$ and GaAs/$(Al_xGa_{1-x})_{0.51}In_{0.49}P$, and $(Al_xGa_{1-x})_{0.51}In_{0.49}P$/GaAs and $Al_xGa_{1-x}As$/GaAs core-shell nanowires.

In this section we study the electronic properties of GaAs/$Al_xGa_{1-x}As$ and GaAs/$(Al_xGa_{1-x})_{0.51}In_{0.49}P$ core-shell nanowires which have a type-I band alignment. GaAs/$(Al_xGa_{1-x})_{0.51}In_{0.49}P$ includes three systems namely GaAs /$Ga_{0.51}In_{0.49}P$, GaAs/$(Al_{0.5}Ga_{0.5})_{0.51}In_{0.49}P$ and GaAs/$Al_{0.51}In_{0.49}P$ with $x = 0$, $x = 0.5$ and $x = 1$ respectively. Fig. 6.5 shows a schematic diagram of the core-shell nanowires with type-I band alignment with GaAs in the core and in the shell respectively. As the lowest conduction band and highest valence band states are in the GaAs region, both electrons and holes are confined within the GaAs region (see Fig. 3.15 in chapter 3). The approximate position of electrons and holes are schematically indicated in the right panel of Fig. 6.5.

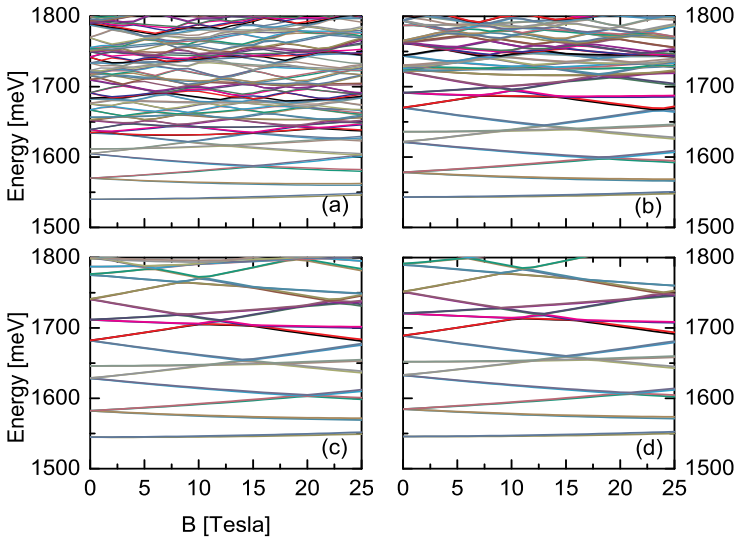

Figure 6.6: The conduction band energy spectrum vs the magnetic field B for a GaAs/$Al_xGa_{1-x}As$ core-shell nanowire with core radius R_c=10 nm and total radius R=20 nm, and with different concentrations of Al, $x = 0.1$ (a), $x = 0.2$ (b), $x = 0.3$ (c) and $x = 0.4$ (d).

In Fig. 6.6, results for the variation of the conduction band energy (at $k_z = 0$) with the magnetic field B for a GaAs/$Al_xGa_{1-x}As$ core-shell nanowire with core radius R_c=10 nm and total radius R=20 nm are given. Here we have a type-I band alignment with lowest conduction band states and highest valence band states in the GaAs core region. We have presented results for different Al concentrations, $x = 0.1$ (a), $x = 0.2$ (b), $x = 0.3$ (c) and $x = 0.4$ (d). By changing the x values we are changing the band offset values at the heterojunction of GaAs/$Al_xGa_{1-x}As$, and thus we introduce an additional confining potential. The height of this potential increases with the increase of Al concentration x and thus the confinement of charge carriers (both electrons and holes in this case) in the core increases with the increase in Al concentration. Hence, the lowest energy states in the conduction band (see Fig. 6.6) are due to the 10 nm core of GaAs, whose contribution increases with the increase in Al concentration x. Thus, by choosing the proper combination of core and shell materials, we can confine the charge carriers (electrons) in smaller regions. We can also observe that the energy dependence on the applied magnetic field is very small when compared to a single-material GaAs nanowire of radius $R = 20$ nm, which is due to the increase in the quantum

confinement effect on the system as the charges are now confined in the smaller core region. Thus, even as we observe Fock-Darwin *like* states as in the case of single-material nanowires, the formation of Landau bands is not observed and can be achieved by choosing a core-shell nanowire with a larger core where the energy dependence on the magnetic field is higher.

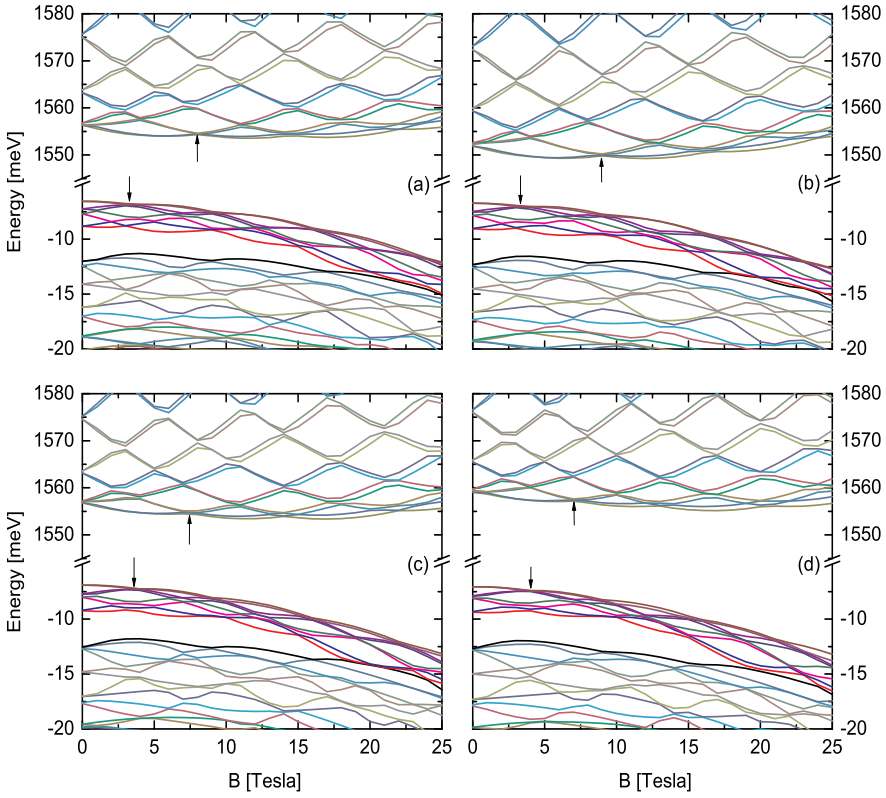

Figure 6.7: The energy spectrum vs the magnetic field B showing Aharonov-Bohm oscillations in ground state for the core-shell nanowires with GaAs in the shell and $Al_{0.4}Ga_{0.6}As$ (a), $Ga_{0.51}In_{0.49}P$ (b), $(Al_{0.5}Ga_{0.5})_{0.51}In_{0.49}P$ (c) and $Al_{0.51}In_{0.49}P$ (d) in the core. Here the core radius is taken as R_c=10 nm and total radius as R=20 nm.

We now look at the conduction and the valence band energy (at $k_z = 0$) evolution with the increase in the magnetic field for core-shell nanowires where the charge carriers are confined in the shell. In Fig. 6.7 we present our results for the core-shell nanowires of $Al_{0.4}Ga_{0.6}As$/GaAs (a), $Ga_{0.51}In_{0.49}P$ /GaAs (b), $(Al_{0.5}Ga_{0.5})_{0.51}In_{0.49}P$/GaAs (c) and $Al_{0.51}In_{0.49}P$/GaAs (d) respectively. These materials are chosen to show the effect of the increase in

the band-offset values VBO and CBO (see Table. 6.2). As the charge carriers are now confined in the shell region, these nanowires behave as ring-like structures with finite inner potential (CBO and VBO) and infinite outer potential.

In Fig. 6.7, we can also see that the ground state energies are oscillating. Just as in the case of single material nanowires, the angular momentum is not a good quantum number in our model as we use an 8-band model which includes band mixing. Nevertheless, such a description would be apt as nanowires with charges confined in the shell are similar to quantum ring systems. Hence, we can interpret the oscillations in the conduction band dispersion in Fig. 6.7 as angular momentum *like* transitions in the presence of a magnetic field. Here we have identified the first crossing with an arrow in each case. We can see that the magnetic field corresponding to the first crossing, decreases as we move from $Al_{0.4}Ga_{0.6}As/GaAs$ to $Al_{0.51}In_{0.49}P/GaAs$ core-shell nanowires. This shows that the magnetic field energy for the first crossing is inversely proportional to the inner potential or the conduction band offset (CBO). Similar behavior is found for hole states in the valence band. Thus, the core-shell nanowires with charged carriers confined in the shell behaves similar to a quantum ring with a finite inner potential.

Let us now understand the energy dependence of a quantum ring on the applied magnetic field and try to interpret our core-shell nanowires results. In case of an ideal quantum ring with radius R_r in a perpendicular magnetic field, the electron energy using a single band model is given as [167]

$$E(m,\Phi) = \frac{\hbar^2}{2m_e R_r^2}(m - \frac{\Phi_B}{\Phi_0})^2, \tag{6.14}$$

where m_e is the effective mass of electron, m is the angular momentum quantum number, $\Phi_B = B\pi R_r^2$ is the flux and $\Phi_0 = \frac{h}{e}$ is the flux quantum. We now apply the same equation in our case by choosing $R_r = \frac{R-R_c}{2} = 15$ nm as the average position of both electrons and holes in these core-shell nanowires with core-radius $R_c = 10$ nm and total radius $R = 20$ nm.

In Fig. 6.8 we have presented the conduction band ground state energy and the $M = -\frac{dE}{d\Phi}$, as a function of the flux $\frac{\Phi_B}{\Phi_0}$. We can see that the oscillations in magnetization results are similar to the results from the ideal ring structures and for higher inner potential values (in our case CBO) we see that the core-shell nanowire structures have the same properties as a quantum ring structure. As stated before, we can change the field at which the first crossing in the conduction band ground state energy is found by changing the inner potential, and this is evident from the magnetization

results in Fig. 6.8 (b). Also, from the magnetization results it is clear that for the lower magnetic flux values ($\frac{\Phi_B}{\Phi_0} < 2$), the magnetization results are dependent on the core material and for higher flux values ($\frac{\Phi_B}{\Phi_0} > 2$) the magnetization results for different systems are very similar. The reason for this is that for lower flux values the effect of quantum confinement is higher than the magnetic field dependence, but for higher flux values the influence of magnetic field dominates.

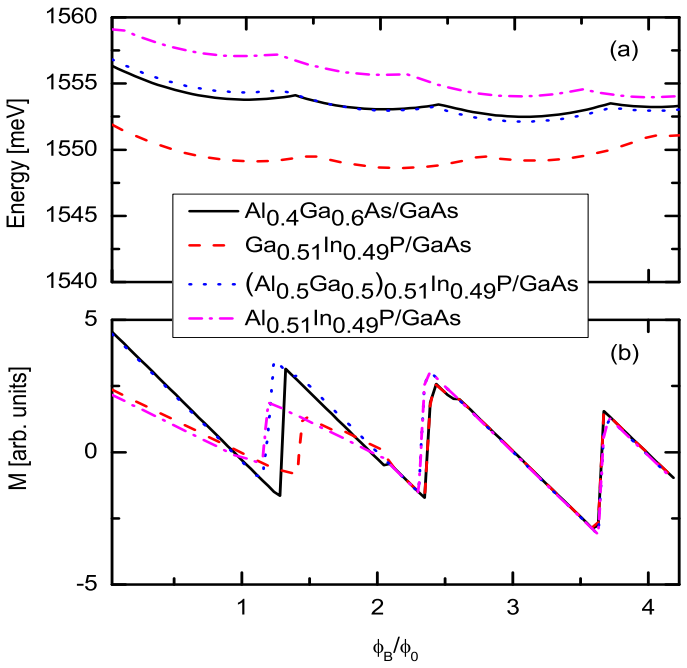

Figure 6.8: The conduction band ground state energy and the magnetization for the core-shell nanowires with GaAs in the shell and $Al_{0.4}Ga_{0.6}As$, $Ga_{0.51}In_{0.49}P$,$(Al_{0.5}Ga_{0.5})_{0.51}In_{0.49}P$ and $Al_{0.51}In_{0.49}P$ in the core as a function of magnetic flux $\frac{\Phi_B}{\Phi_0}$. Here the core radius is taken as R_c=10 nm and total radius as R=20 nm.

Thus in case of the core-shell nanowires we find that the nanowires with GaAs as the core show Fock-Darwin *like* states and in the case of nanowires with GaAs as the shell we see Aharanov-Bohm oscillations in the energy spectrum evolution with magnetic field.

6.5 Summary and conclusions

In the present chapter we have studied the electronic and optical properties of both the single material and the core-shell nanowires under the influence of a uniform magnetic field. Our study of single material GaAs nanowires shows that the energy dependence on magnetic field is dependent on the material parameters such as bandgap E_G and Kane's energy E_P. Although the angular momentum quantum number m is not a good quantum number, we found that such a description is quite apt due to the similarity of our system of nanowires with the quantum dot and quantum ring systems. The energy spectrum of GaAs nanowire shows that for higher magnetic field values, Landau bands are formed. We can also observe the formation of Fock-Darwin *like* states. This was also true in the case of core-shell nanowires with GaAs in the core, i.e. the systems where the charge carriers are confined in the core.

In case of core-shell nanowires with GaAs in the shell, the lowest conduction band and the highest valence band states occur in the shell region and hence the charge carriers are confined in the shell. This results in both electrons and holes moving in a ring-like structure, which has a finite inner potential (given by the band offset values) and an infinite outer potential. As was observed in the case of quantum rings, these core-shell nanowires also show Aharonov-Bohm oscillations with the increase in magnetic field values. Oscillating values for the magnetization are found for the conduction band ground state. The dependence of these oscillations on the magnetic flux can be controlled by the choice of the materials and also on the size of the core and the shell regions. Thus we conclude that the core-shell nanowires can show the properties of both quantum dots and quantum rings depending on the choice of the core and the shell materials.

Summary and outlook

In this thesis I have studied the electronic properties of both single material and core-shell freestanding nanowires. Throughout the thesis I investigated zincblende nanowires grown in the [001] crystallographic direction. In chapter 1, a comprehensive introduction was given for the various growth techniques, the various properties and the possible applications of nanowires. The availability of the latest technologies to obtain nanowires of various sizes and shapes, the extraordinary properties they have to offer and the increase in the realization of various applications of nanowires have motivated me to study their electronic and optical properties.

In chapter 2 the **k.p** method used in this thesis was discussed in detail. A discussion of various Kohn-Luttinger (KL) Hamiltonians used in this thesis were given. The transformation of KL Hamiltonian from the bulk to nanostructures is also given.

In this thesis we studied freestanding zincblende nanowires grown in [001] crystallographic direction. The sizes of these nanowires are chosen in such a way as to include the effects of quantum confinement on these systems. In chapter 3 we studied the electronic structure of GaAs/$Al_xGa_{1-x}As$ and $Al_xGa_{1-x}As$/GaAs core-shell nanowires using the 6×6 Kohn-Luttinger **k.p** Hamiltonian. During our study we found that for single material nanowires the split-off band has a considerable influence on the valence band ground state for very thin nanowires. The camel back structure is removed by the inclusion of the split-off band energy term in the Hamiltonian. This is not the case for thick wires where the presence of the split-off band energy terms do not alter the camel back structure. It is also shown that the camel back structure of the top of the valence band around k_z=0, which is present in pure GaAs nanowires, slowly disappears with increasing Al concentration. I found that the camel back structure is not always present in core-shell structures. When GaAs is the core material, the evolution of the camel back structure as function of the core radius is almost independent of the Al concentration, while for wires with a GaAs shell, the region in which a camel back structure can be observed is larger for smaller Al concentration.

I also calculated the absorption spectra for both circular and linear polarized light. The presence of the camel back structure is reflected as a peak in the absorption spectra. The effect of quantum confinement can be seen in the absorption spectra. For the thick wires this results in broader spectra when compared to the many absorption peaks observed for thin wires. We predict that spin polarized electrons can be obtained in this system using circular polarized light for some specific energies. Finally, we give the electron hole densities which show that both electrons and holes confine in the GaAs region in GaAs/$Al_xGa_{1-x}As$ and $Al_xGa_{1-x}As$/GaAs core-shell nanowires.

In chapter 3 we investigated the electronic and optical properties of core-shell nanowires using a 6×6 Kohn-Luttinger **k.p** Hamiltonian. This Hamiltonian does not include the influence of the conduction band on the valence band states and vice versa. This method is applicable to wide gap semiconductors like GaAs but, for narrow gap semiconductors a more advanced 8×8 Kohn-Luttinger **k.p** Hamiltonian is required. The study of the ground state properties of narrow gap semiconductors using an 8-band KL Hamiltonian formed the basis of our study in chapter 4. The influence of the conduction band on the valence band states and vice versa is taken into consideration using the parameter E_P which is known as Kane's energy. E_P couples the conduction band Γ_6 with the valence bands Γ_7, Γ_8 and is proportional to the square of the matrix element $\langle S|p_x|X\rangle$, which is independent of the band gap E_G. The 8-band KL Hamiltonian involved using Luttinger-like parameters ($\tilde{\gamma}_i$) in the place of Luttinger parameters (γ_i) used in the 6-band KL Hamiltonian. In the literature two methods have been given to obtain the Luttinger-like parameters, one given by Bahder and Pryor [89, 90] ($\tilde{\gamma_i^B}$) and the other by Pidgeon and Brown [88] ($\tilde{\gamma}_i$). I have generated the valence band diagrams of GaAs, InAs and InSb using the Luttinger-like parameters obtained from both approaches. I found that although GaAs is a wide gap semiconductor and its bandgap E_G is larger than the split-off energy Δ, still an 8-band KL Hamiltonian is necessary to obtain the correct valence band structure. We also studied the influence of the E_P value on the camel back structure observed in the top valence band. It is found that the camel back structure is very sensitive to the E_P value.

An 8-band model was found to be necessary to study most of the semiconductor nanowires, which was used in the following chapters of this thesis. In chapter 3 we studied GaAs/$Al_xGa_{1-x}As$ and $Al_xGa_{1-x}As$/GaAs core-shell nanowires which have a type-I band alignment, while InAs/GaSb has a type-III band alignment. In particular, both electrons and holes are confined in different regions of the heterostructure in a type-III band alignment. In the case of InAs/GaSb heterostructure the valence band maximum of GaSb is

above the conduction band minimum of InAs. Thus, the lowest conduction band state is found in InAs and the highest valence band state is found in GaSb regions, respectively. This results in electrons that are confined in InAs and holes confined in GaSb regions respectively. We found that by changing the size of InAs and GaSb regions in the InAs/GaSb core-shell wire, we can change the effective bandgap of the system. This effective bandgap can be reduced to zero and even to a negative value. Negative effective bandgap occurs when the lowest conduction band state is below the highest valence band state and in this case the electron-hole hybridization occurs. Thus, these hybridized systems have a semi-metallic behavior, which could be used in developing novel electronic devices. We have also observed a small minigap Δ_{mg} opening away from the zone center. This minigap can be observed only when a single conduction band overlaps with the valence band states which will influence the conductivity of the system.

So far in this thesis we have not applied any external potential. In the last chapter, we introduce a magnetic field as an external potential in the 8-band KL Hamiltonian. We investigated the electronic structure of single material and core-shell nanowires for GaAs, $Al_{0.4}Ga_{0.6}As$, and $(Al_xGa_{1-x})_{0.51}In_{0.49}P$. Our study of single material nanowires shows that both the bandgap E_G and the Kane's parameter E_P can influence the conduction band energy which depends on the magnetic field. Landau levels are formed at higher magnetic field values. This is also observed for core-shell nanowires where both electrons and holes are confined in the core region. Fock-Darwin states can be observed in systems where charge carriers are confined in the core region.

In the case of nanowires with electrons and holes confined in the shell, the system behaves like a quantum ring with a finite potential in the inner ring. In this case Aharonov-Bohm oscillations are found. The conduction band ground state exhibits crossings that occur at different magnetic field values. This can also be interpreted in terms of the flux (Φ) passing through the quantum wire, where change in flux by one flux quantum ($\frac{h}{e}$) forces the electron in the ground state to change its angular momentum by one. The conduction band ground state depends on the flux that can be modified by changing the core material and keeping the shell material as GaAs. Thus we found that when the charges are confined in the core, Fock-Darwin states are observed and when they are confined in the shell, Aharonov-Bohm oscillations are observed. Thus we have shown that Aharonov-Bohm oscillations can be observed in core-shell nanowires which are very easy to obtain when compared to quantum rings.

In this thesis, I investigated the electronic and optical properties of core-shell nanowires using the **k.p** method. I found that by using core-shell

nanowires instead of single material nanowires, we get the advantage of tuning their properties by changing the size and the materials used. The results observed in this thesis for the wide gap and narrow gap semiconductors and their heterostructures can also be applied to other systems with similar configurations such as HgTe, CdTe etc.. The above study can be further extended to include asymmetric properties such as the bulk inversion asymmetry (BIA) and the structural inversion asymmetry (SIA). Influence of BIA and SIA on the properties of the camel back structure would be quite interesting to study. Also, in the present thesis only the lattice matched systems have been studied. Inclusion of strain in our Hamiltonian will give us an opportunity to extend the present study to type-II systems such as the GaAs/InAs core-shell nanowires. Topological insulating behavior is reported in InAs/GaSb quantum wells [164] and hence a study into the possibility of observing this behavior in the InAs/GaSb core-shell nanowires is very much needed. Also, the application of external potentials such as the magnetic field in these systems to tune their effective bandgap values can be studied.

Samenvatting en vooruitzichten

In dit proefschrift heb ik de elektronische eigenschappen onderzocht van zowel enkelmateriaal als kern-schil vrijstaande nanodraden. Doorheen het gehele proefschrift heb ik zinkblende nanodraden onderzocht, gegroeid in de [001] kristallografische richting. In hoofdstuk 1 werd een uitgebreide inleiding gegeven voor de verschillende groeitechnieken, de verschillende eigenschappen en de mogelijke toepassingen van nanodraden. De beschikbaarheid van de nieuwste technologieën om nanodraden van verschillende maten en vormen te bekomen, de buitengewone eigenschappen die ze te bieden hebben en de toename van de realisatie van verschillende toepassingen van nanodraden hebben mij gemotiveerd om hun elektronische en optische eigenschappen te bestuderen.

In hoofdstuk 2 wordt de **k.p** methode die wordt gebruikt in dit proefschrift in detail besproken. Een bespreking van de verschillende Kohn-Luttinger (KL) Hamiltonianen gebruikt in dit proefschrift werd gegeven. De transformatie van de KL Hamiltoniaan van bulk tot nanostructuren wordt tevens behandeld.

In dit proefschrift onderzochten we vrijstaande zinkblende nanodraden gegroeid in de [001] kristallografische richting. De afmetingen van deze nanodraden zijn gekozen zodanig dat het effect van kwantumopsluiting mee in rekening wordt gebracht. In hoofdstuk 3 onderzochten we de elektro-nische structuur van GaAs/$Al_xGa_{1-x}As$ en $Al_xGa_{1-x}As$/GaAs kern-schil nanodraden met behulp van de 6×6 Kohn-Luttinger **k.p** Hamiltoniaan. Tijdens onze studie vonden we dat voor enkelmateriaal nanodraden de afsplitsingsband een grote invloed op de grondtoestand van de valentieband voor zeer dunne nanodraden heeft. De "camel back"-structuur verdwijnt door het opnemen van de energieterm van de afsplitsingsband in de Hamiltoniaan. Dit is niet het geval voor dikke draden waar de aanwezigheid van de energietermen van de afsplitsingsband niets veranderen aan de "camel back"-structuur. Ook wordt aangetoond dat de "camel back"-structuur van de top van de valentieband rond $k_z = 0$, die in zuivere GaAs nanodraden aanwezig is, langzaam verdwijnt met toenemende Al concentratie. Ik vond dat de "camel back"-

structuur niet altijd aanwezig is in kern-schil-structuren. Wanneer GaAs het kernmateriaal is, is de evolutie van de "camel back"-structuur als functie van de kernstraal vrijwel onafhankelijk van de Al concentratie, terwijl voor draden met een GaAs schil de regio waar een "camel back"-structuur waarneembaar is groter is, bij kleinere Al concentratie.

Ik berekende ook de absorptiespectra voor zowel circulair als lineair gepolariseerd licht. De aanwezigheid van de "camel back"-structuur is zichtbaar als een piek in het absorptiespectrum. Het effect van kwantumopsluiting is te zien in de absorptiespectra. Voor de dikke draden resulteert dit in bredere spectra vergeleken met de vele absorptiepieken waargenomen voor dunne draden. We voorspellen dat spingepolariseerde elektronen kunnen worden verkregen in dit systeem door middel van circulair gepolariseerd licht van bepaalde energieën. Tot slot geven we de elektron-gat dichtheden die laten zien dat zowel de elektronen als gaten worden opgesloten in de GaAs regio in GaAs/$Al_xGa_{1-x}As$ en $Al_xGa_{1-x}As$/GaAs kern-schil nanodraden.

In hoofdstuk 3 onderzochten we de elektronische en optische eigenschappen van kern-schil nanodraden met een 6×6 Kohn-Luttinger **k.p** Hamiltoniaan. Deze Hamiltonian bevat geen invloed van de geleidingsband op de valentiebandtoestanden en vice versa. Deze methode is van toepassing op halfgeleiders met een grote bandkloof zoals GaAs, maar voor halfgeleiders met een kleine is een meer geavanceerde 8×8 Kohn-Luttinger **k.p** Hamiltoniaan vereist. De studie van de grondtoestand eigenschappen van halfgeleiders met een kleine bandkloof met een 8-band KL Hamiltoniaan vormde de basis van ons onderzoek in hoofdstuk 4. De invloed van de geleidingsband op de valentieband toestanden en vice versa wordt in rekening gebracht met de parameter E_P die bekend staat als de Kane energie. E_P koppelt de geleidingsband Γ_6 met de valentie banden Γ_7, Γ_8 en is evenredig met het kwadraat van het matrix element $\langle S|p_x|X\rangle$, dat onafhankelijk is van de bandkloof E_G. De 8-band KL Hamiltoniaan maakt gebruik van Luttinger-achtige parameters ($\tilde{\gamma}_i$) in de plaats van Luttinger parameters (γ_i) van de 6-band KL Hamiltoniaan. In de literatuur zijn twee methoden gegeven om de Luttinger-achtige parameters te bekomen, één gegeven door Bahder en Pryor [89, 90] ($\tilde{\gamma}_i^B$) en de andere door Pidgeon en Brown [88] ($\tilde{\gamma}_i$). Ik heb de valentiebanddispersies berekend voor GaAs, InAs en InSb met behulp van de Luttinger-achtige parameters verkregen uit beide benaderingen. Ik vond dat hoewel GaAs een halfgeleider met een grote bandkloof is en de bandgap E_G groter is dan de afsplitsingsenergie Δ, er nog steeds een 8-band KL Hamiltonian nodig is om de juiste valentiebandstructuur te verkrijgen. We onderzochten ook de invloed van de E_P waarde op de "camel back"-structuur waargenomen in de bovenste valentieband. Het blijkt dat de "camel back"-structuur zeer gevoelig is voor

de E_P waarde.

Een 8-band model bleek noodzakelijk om de meeste van de halfgeleider nanodraden te bestuderen. In de volgende hoofdstukken van dit proefschrift werd dit 8 banden model dan ook gebruikt. In hoofdstuk 3 onderzochten we GaAs/$Al_xGa_{1-x}As$ en $Al_xGa_{1-x}As$/GaAs kern-schil nanodraden met een type-I banduitlijning, terwijl InAs/GaSb een type-III banduitlijning heeft. In het bijzonder zijn zowel elektronen als gaten opgesloten in verschillende gebieden van de heterostructuur in een type-III band uitlijning. Bij een InAs/GaSb heterostructuur ligt het maximum van de valentieband van GaSb boven het minimum van de geleidingsband toestand in de van InAs. Aldus wordt de laagste toestand in de geleidingsband in InAs en de hoogste toestand in de valentieband in GaSb gebieden gevonden. Dit resulteert in elektronen die zijn opgesloten in InAs en gaten opgesloten in GaSb. We vonden dat door de grootte van InAs en GaSb gebieden in de InAs/GaSb kern-schil draad te veranderen, we de effectieve bandkloof van het systeem kunnen veranderen. Deze effectieve bandkloof kan tot nul worden teruggebracht en zelfs tot een negatieve waarde. Een negatieve effectieve bandkloof treedt op wanneer de laagste toestand in de geleidingsband lager ligt dan de hoogste toestand in de valentieband en in dit geval vindt elektron-gat hybridisatie plaats. Dan vertonen deze gehybridiseerde systemen een semi-metallisch gedrag dat kan gebruikt worden in de ontwikkeling van nieuwe elektronische apparaten. We hebben ook gezien dat een kleine minikloof Δ_{mg} zich vormt, weg van het van het zone centrum. Deze minikloof kan enkel worden waargenomen wanneer een enkele geleidingsband overlapt met de valentiebandtoestanden die de geleidbaarheid van het systeem beïnvloeden.

Tot nu toe hebben we in dit proefschrift geen externe potentiaal aangelegd. In het laatste hoofdstuk introduceren we een magneetveld als een externe potentiaal in de 8-band KL Hamiltoniaan. We onderzochten de elektronische structuur van enkelmateriaal en kern-schil nanodraden voor GaAs, $Al_{0.4}Ga_{0.6}As$ en $(Al_xGa_{1-x})_{0.51}In_{0.49}P$. Uit onze studie van enkelmateriaal nanodraden blijkt dat zowel de bandgap E_G en Kane parameter E_P een sterke invloed heeft op de geleidingsband die afhangt van het magneetveld. Landau niveaus worden gevormd bij hoger waarden van het magneetveld. Dit wordt ook waargenomen voor kern-schil nanodraden waarbij zowel elektronen als gaten opgesloten zitten in het kerngebied. Fock-Darwin toestanden worden waargenomen in systemen waar ladingsdragers worden opgesloten in het kerngebied.

Bij nanodraden met elektronen en gaten opgesloten in de schil, gedraagt het systeem zich als een kwantumring met een eindige potentiaal in de binnenring. In dit geval worden Aharonov-Bohm oscillaties gevonden. De geleidingsband grondtoestand vertoont kruisingen die zich voordoen bij verschil-

lende waarden van het magneetveld. Dit kan ook worden geïnterpreteerd in termen van de flux (Φ) die door de kwantum-draad gaat, waar verandering in flux met een flux kwantum ($\frac{h}{e}$) het elektron in de grondtoestand dwingt zijn impulsmoment met één te veranderen. De geleidingsband grondtoestand is afhankelijk van de flux die kan gewijzigd worden door het kernmateriaal te veranderen en het schilmateriaal GaAs te behouden. Zo vonden we dat wanneer de ladingen worden opgesloten in de kern, Fock-Darwin toestanden worden geobserveerd en wanneer ze worden opgesloten in de schil, Aharonov-Bohm oscillaties optreden. Zo hebben wij aangetoond dat Aharonov-Bohm oscillaties worden waargenomen in kern-schil nanodraden die zeer gemakkelijk te verkrijgen zijn in vergelijking met kwantumringen.

In dit proefschrift heb ik de elektronische en optische eigenschappen van kern-schil nanodraden onderzocht met behulp van de **k.p** methode. Ik vond dat door het gebruik van kern-schil nanodraden in plaats van enkelmateriaal nanodraden, we het voordeel hebben dat we hun eigenschappen kunnen afstemmen door het veranderen van de grootte en de gebruikte materialen. De waarnemingen in dit onderzoek over halfgeleiders met een grote en kleine bandkloof en hun heterostructuren kan ook worden toegepast op andere systemen met vergelijkbare configuraties zoals HgTe, CdTe etc. Deze studie kan verder worden uitgebreid met asymmetrische eigenschappen, zoals de bulk inversie asymmetrie (BIA) en de structurele inversie asymmetrie (SIA). De studie van de invloed van BIA en SIA op de eigenschappen van de "camel back"-structuur kan erg interessant zijn. Ook werden in dit proefschrift enkel sytemen bestudeerd zonder strain. Opname van strain in onze Hamiltoniaan geeft ons de kans om het huidige onderzoek uit te breiden tot type-II systemen, zoals de GaAs/InAs kern-schil nanodraden. Topologisch isolerend gedrag wordt gerapporteerd in InAs/GaSb kwantumputten [164] en dus is een onderzoek naar de mogelijkheid van het observeren van dit gedrag in de InAs/GaSb kern-schil nanodraden hard nodig. Ook kan het aanleggen van externe potentialen zoals het magneetveld in deze systemen, om hun effectieve bandgap te tunen, kunnen worden bestudeerd.

Appendix A

Perturbation techniques

A.1 Time independent perturbation theory

Using the perturbation method the total Hamiltonian H can be separated as unperturbed Hamiltonian $H^{(0)}$ with known solutions and the other part consists of a small perturbation $H^{'}$ with λ as the perturbation parameter,

$$H = H^{(0)} + \lambda H^{'}. \tag{A.1}$$

The unperturbed wave function $\phi_n(0)$ and the eigenvalues $E_n(0)$ are satisfy the equation

$$H^{(0)}\phi_n(0) = E_n^{(0)}\phi_n^{(0)}. \tag{A.2}$$

The solutions of the total Hamiltonian $H\psi$=$E\psi$ can be written as

$$E = E^{(0)} + \lambda E^{(1)} + \lambda^2 E^{(2)} + \lambda^3 E^{(3)} + ... \tag{A.3}$$
$$\psi = \psi^{(0)} + \lambda \psi^{(1)} + \lambda^2 \psi^{(2)} + \lambda^3 \psi^{(3)} + ... \tag{A.4}$$

Substituting the above equations for H, E and ψ in the Schrödinger equation we find, to each order in λ,

$$H^{(0)}\psi^{(0)} = E^{(0)}\psi^{(0)}. \tag{A.5}$$
$$H^{(0)}\psi^{(1)} + H^{1}\psi^{(0)} = E^{(0)}\psi^{(1)} + E^{(1)}\psi^{(0)}. \tag{A.6}$$
$$H^{(0)}\psi^{(2)} + H^{1}\psi^{(1)} = E^{(0)}\psi^{(2)} + E^{(1)}\psi^{(1)} + E^{(2)}\psi^{(0)}. \tag{A.7}$$

Zeroth order solutions: From the above solutions it is clear that the zeroth order solutions are the unperturbed solutions:

$$\psi_n^{(0)} = \phi_n^{(0)}. \tag{A.8}$$
$$E_n^{(0)} = E_n^{(0)}. \tag{A.9}$$

The first order wave function $\psi^{(1)}$ can be expressed as a linear combination of the unperturbed solutions

$$\psi_n^{(1)} = \sum_m a_{mn}^{(1)} \phi_m^{(0)}. \tag{A.10}$$

Thus,

$$(H^{(0)} - E^{(0)_n}) = E^{(1)}\phi_n^{(0)} - H^{'}\phi_n^{(0)}. \tag{A.11}$$

Multiplying the above equation by $\phi_m^{(0)*}$ and integrating over space, using the normalization condition

$$\langle \phi_m^{(0)} | \phi_n^{(0)} \rangle = \delta_{mn}, \tag{A.12}$$

we obtain

$$E^{(1)} = H_{nn}^{'}, \tag{A.13}$$

and

$$a_{mn}^{(1)} = \frac{H_{mn}^{'}}{E_n^{(0)} - E_m^{(0)}}, \qquad m \neq n, \tag{A.14}$$

where

$$H_{mn}^{'} = \int \phi_m^{(0)*} H^{'} phi_n^{(0)} d^3r. \tag{A.15}$$

To this first order in perturbation we need to normalize the wave function

$$\int (\phi_n^{(0)} + \sum_m a_{mn}^{(1)} \phi_m^{(0)}))^* (\phi_n^{(0)} + \sum_m a_{mn}^{(1)} \phi_m^{(0)})) d^3r = 1, \tag{A.16}$$

or

$$1 + a_{nn}^{(1)*} + a_{nn}^{(1)} + \sum_m a_{mn}^{(1)} a_{mn}^{(1)*} = 1. \tag{A.17}$$

Thus $a_{nn}^{(1)} = 0$ and the first order perturbation solutions are therefore given as

$$\psi_n = \phi_n^{(0)} + \sum_{m \neq n} \frac{H'_{mn}}{E_n^{(0)} - E_m^{(0)}} \phi_m^{(0)}. \tag{A.18}$$

$$E_n = E_n^{(0)} + H'_{nn}. \tag{A.19}$$

Similarly, the second order perturbation solutions can be given as

$$\begin{aligned}\psi_n =& \phi_n^{(0)} + \sum_{m \neq n} \frac{H'_{mn}}{E_n^{(0)} - E_m^{(0)}} \phi_m^{(0)} \\ &+ \sum_{m \neq n} \{ [\sum_{k \neq n} \frac{H'_{mk} H'_{kn}}{(E_n^{(0)} - E_m^{(0)})(E_n^{(0)} - E_k^{(0)})} - \frac{H'_{mn} H'_{nn}}{(E_n^{(0)} - E_k^{(0)})^2}] \phi_m^{(0)} \\ &- \frac{|H'_{mn}|^2}{2(E_n^{(0)} - E_k^{(0)})^2} \phi_n^{(0)} \}. \end{aligned} \tag{A.20}$$

$$E_n = E_n^{(0)} + H'_{nn} + \sum_{m \neq n} \frac{|H'_{nm}|^2}{E_n^{(0)} - E_m^{(0)}}. \tag{A.21}$$

Matrix Formulation The present eigenvalue problem

$$H\psi = (H^{(0)} + H')\psi = E\psi, \tag{A.22}$$

the solution of which can be written as

$$\psi = \sum_m a_m \phi_m^{(0)}, \tag{A.23}$$

where $\phi_m^{(0)}$ are the eigenfunctions of unperturbed Hamiltonian,

$$H^{(0)}\phi_m^{(0)} = E^{(0)}\phi_m^{(0)}, \tag{A.24}$$

where $\phi_m^{(0)}$, $m = 1, 2, 3..N$ may also be degenerate orthonormalized wave functions, then the eigen function equation can be written as

$$\sum_{n=1}^{N}(H_{mn} - E\delta_{mn})a_n = 0. \tag{A.25}$$

A.2 Löwdin perturbation method

In the Löwdin perturbation method the eigen functions and eigen energies are divided into two classes A and B. Here we are interested in states of class A with the influence of states in B included as a perturbation. We start with Eq.(A.25), which can be rewritten as

$$(E - H_{mm})a_m = \sum_{n\neq m}^{A} H_{mn}a_n + \sum_{\alpha\neq m}^{B} H_{m\alpha}a_\alpha, \tag{A.26}$$

or

$$a_m = \sum_{n\neq m}^{A} \frac{H_{mn}}{(E - H_{mm})}a_n + \sum_{\alpha\neq m}^{B} \frac{H_{m\alpha}}{(E - H_{mm})}a_\alpha, \tag{A.27}$$

where the first sum on the right-hand side is over the states in class A only, while the second sum is over the states in class B. As we are interested only in the coefficients a_m where m is in class A, we can eliminate those in class B through an iterative method and obtain

$$a_m = \sum_{n\neq m}^{A} \frac{U_{mn}^A - H_{mn}\delta_{mn}}{(E - H_{mm})}a_n, \tag{A.28}$$

where

$$U_{mn}^A = H_{mn} + \sum_{\alpha\neq m}^{B} \frac{H_{m\alpha}H_{\alpha n}}{(E - H_{\alpha\alpha})} + \sum_{\alpha\beta\neq m, n\alpha\neq\beta}^{B} \frac{H_{m\alpha}H_{\alpha\beta}H_{\beta n}}{(E - H_{\alpha\alpha})(E - H_{\beta\beta})} + ... \tag{A.29}$$

Therefore when we solve the eigenvalue problems for a_n, $(n \in A)$:

$$\sum_{n}^{A}(U_{mn}^{A} - H_{mn}\delta_{mn})a_n = 0, \qquad m \in A, \tag{A.30}$$

and

$$a_l = \sum_{n}^{A} \frac{U_{ln}^{A} - H_{ln}\delta_{ln}}{(E - H_{ll})}a_n, \qquad l \in B. \tag{A.31}$$

When the coefficients a_n belonging to class A are determined from the eigenequation (A.30), the coefficients a_l in class B can be found from (A.31). A necessary condition for the expansion of (A.29) to be convergent is

$$|H_{\alpha\alpha}| \ll |E - H_{\alpha\alpha}|, \qquad m \in A, \alpha \in B. \tag{A.32}$$

Appendix B

8-band: 3 parameter and 6 parameter models

In Ref. [94] the Luttinger and Luttinger-like parameters for the split-off band Γ_7 ($\gamma_{\Delta i}$ and $\tilde{\gamma}_{\Delta i}$, respectively) are given and have the following form (E_{PX}, E_{GC} and Δ_C are taken from Ref. [86])

$$\begin{aligned}
\gamma_{\Delta 1} =& \gamma_1 - \frac{E_P}{3}\left(\frac{1}{E_G} - \frac{1}{E_G+\Delta}\right) - \frac{E_{PX}}{3}\left(\frac{1}{E_G+E_{GC}}\right. \\
&\left. + \frac{1}{E_G+E_{GC}+\Delta_C} - \frac{2}{E_G+\Delta+E_{GC}+\Delta_C}\right), \\
\gamma_{\Delta j} =& \gamma_j - \frac{E_P}{12}\left(\frac{1}{E_G} - \frac{1}{E_G+\Delta}\right) + \frac{E_{PX}}{12}\left(\frac{2}{E_G+E_{GC}}\right. \\
&\left. - \frac{1}{E_G+E_{GC}+\Delta_C} - \frac{1}{E_G+\Delta+E_{GC}+\Delta_C}\right), \qquad j=2,3 \qquad \text{(B.1)}
\end{aligned}$$

$$\begin{aligned}
\tilde{\gamma}_{\Delta 1} =& \gamma_1 - \frac{E_P}{3E_G} - \frac{E_{PX}}{3}\left(\frac{1}{E_G+E_{GC}}\right. \\
&\left. + \frac{1}{E_G+E_{GC}+\Delta_C} - \frac{2}{E_G+\Delta+E_{GC}+\Delta_C}\right), \\
\tilde{\gamma}_{\Delta j} =& \gamma_j - \frac{E_P}{6E_G} + \frac{E_{PX}}{12}\left(\frac{2}{E_G+E_{GC}}\right. \\
&\left. - \frac{1}{E_G+E_{GC}+\Delta_C} - \frac{1}{E_G+\Delta+E_{GC}+\Delta_C}\right), \qquad j=2,3, \qquad \text{(B.2)}
\end{aligned}$$

where E_{PX}, E_{GC} and Δ_C are related to the higher conduction bands (Γ_{7C} and Γ_{8C}) (see Fig. 1 in Ref. [94]) and they account for the influence of the Γ_{7C} and Γ_{8C} bands on the split-off band Γ_7.

The approximations $\gamma_j \approx \gamma_{\Delta j}$ and $\tilde{\gamma}_j \approx \tilde{\gamma}_{\Delta j}$ give $A_\Delta = A$, $B_\Delta = B$, $C_\Delta = C$ in the 8-band Hamiltonian $\mathbb{H}_8$.

Appendix C

8-band Hamiltonian with magnetic field

The 8-band Hamiltonian with magnetic field is given by [96]

$$H^B_{k_\pm} = H_{LK}(k^0_\pm) + H_{LK}(k^B_\pm) + g\mu_B\kappa B, \tag{C.1}$$

where $H_{KL}(k^0_\pm)$ is the Kohn-Luttinger Hamiltonian without magnetic field (see subsection 2.3.2), $H_{KL}(k^B_\pm)$ is the KL Hamiltonian with magnetic field and $g\mu_B\kappa B$ gives the zeeman splitting term. In the zeeman term, $\kappa = \pm\ 1$ for electrons, $\kappa = \pm\ 3$ for heavy holes, $\kappa = \pm\ 1$ for light holes, $\kappa = \pm\ 2$ for split-off band and $\pm\sqrt{2}$ for A the coupling term between split-off band and light holes (see Eq. (C.6)).

Landé's g factor κ for conduction band [111]:

$$g_{CB} = 2 - \frac{2}{3}\frac{E_G\Delta}{E_G(E_G+\Delta)}, \tag{C.2}$$

and g for valence band [113, 114]:

$$g_{VB} = \gamma_3 + \frac{2}{3}\gamma_2 - \frac{1}{3}\gamma_1 - \frac{2}{3}. \tag{C.3}$$

The matrix elements of the 8-band KL Hamiltonian with magnetic field (B) defined in section 2.4.1 are given as

$$
\begin{aligned}
E^H_{7-} &= E_g + \frac{\hbar^2}{2}\{\frac{1}{2}[k_+\frac{1}{m_0}k_- + k_-\frac{1}{m_0}k_+] + k_z\frac{1}{m_0}k_z\},\\
E^H_{8+} &= 0 - \frac{\hbar^2}{2m_0}\{\frac{1}{2}[k_+(\tilde{\gamma}_1+\tilde{\gamma}_2)k_- + k_-(\tilde{\gamma}_1+\tilde{\gamma}_2)k_+] + k_z(\tilde{\gamma}_1-2\tilde{\gamma}_2)k_z\},\\
E^L_{8+} &= 0 - \frac{\hbar^2}{2m_0}\{\frac{1}{2}[k_+(\tilde{\gamma}_1-\tilde{\gamma}_2)k_- + k_-(\tilde{\gamma}_1-\tilde{\gamma}_2)k_+] + k_z(\tilde{\gamma}_1+2\tilde{\gamma}_2)k_z\},\\
C &= \frac{\hbar^2}{2m_0}\{\sqrt{3}[k_-\bar{\gamma}k_- + k_+\mu k_+]\},\\
B &= \frac{\hbar^2}{2m_0}\{\sqrt{3}[k_-\tilde{\gamma}_3k_z + k_z\tilde{\gamma}_3k_-]\},\\
E^H_{7+} &= \Delta_{SO} - \frac{\hbar^2}{2m_0}\{\frac{1}{2}(k_+\tilde{\gamma}_1k_- + k_-\tilde{\gamma}_1k_+) + k_z^2\},\\
A &= \frac{\hbar^2}{2m_0}[2\tilde{\gamma}_2k_z^2 - (\frac{1}{2}(k_+\tilde{\gamma}_2k_- + k_-\tilde{\gamma}_2k_+))],\\
P^{\pm} &= Pk_{\pm},\\
P^z &= Pk_z,\\
P &= \frac{\hbar}{m_0}\langle S|p_x|iX\rangle,\\
E_P &= (\frac{2m_0}{\hbar^2})P^2.
\end{aligned}
\tag{C.4}
$$

Here $k_\pm = k^0_\pm + k^B_\pm$ with $k^0_\pm = -ie^{\pm i\varphi}(\frac{\partial}{\partial\rho} \pm \frac{i}{\rho}\frac{\partial}{\partial\varphi})$ and $k^B_\pm = \pm i\frac{\rho}{2l_B^2}e^{\pm i\varphi}$.

Diagonal matrix elements:

$$\begin{aligned}\textbf{(1)}\ \langle m_1,l_1|E^H_{7-}|m_2,l_2\rangle =& E_g+\frac{\hbar^2}{2m_0}\{(\frac{\alpha_{m_2l_2}}{R})^2(\langle m_1,l_1|\delta(\rho-R_c)|m_2-1,l_2\rangle\\ &-\langle m_1,l_1|\delta(\rho-R_c)|m_2+1,l_2\rangle)\\ &-m_2\langle m_1,l_1|(\frac{1}{2l_B^2})|m_2,l_2\rangle_{c/s}\\ &+\langle m_1,l_1|(\frac{\rho}{2l_B^2})^2|m_2,l_2\rangle_{c/s}+k_z^2\}. \end{aligned}\tag{C.5}$$

$$\begin{aligned}\textbf{(2)}\ \langle m_1,l_1|A|m_2,l_2\rangle =& \frac{\hbar^2}{2m_0}\{(\frac{\alpha_{m_2l_2}}{R})^2(\tilde{\gamma}_1)_{c/s}+[(\tilde{\gamma}_1)_c-(\tilde{\gamma}_1)_s]\\ &(\langle m_1,l_1|\delta(\rho-R_c)|m_2-1,l_2\rangle\\ &-\langle m_1,l_1|\delta(\rho-R_c)|m_2+1,l_2\rangle)\\ &-m_2\langle m_1,l_1|(\frac{1}{2l_B^2})(\tilde{\gamma}_1)|m_2,l_2\rangle_{c/s}\\ &\langle m_1,l_1|(\frac{\rho}{2l_B^2})^2(\tilde{\gamma}_1)|m_2,l_2\rangle_{c/s}\\ &+k_z^2\langle m_1,l_1|(\tilde{\gamma}_1)|m_2,l_2\rangle_{c/s}\}. \end{aligned}\tag{C.6}$$

$$\begin{aligned}\textbf{(3)}\ \langle m_1,l_1|E^{H/L}_{8+}|m_2,l_2\rangle =& -\frac{\hbar^2}{2m_0}\{(\frac{\alpha_{m_2l_2}}{R})^2(\tilde{\gamma}_1\pm\tilde{\gamma}_2)_{c/s}\\ &+[(\tilde{\gamma}_1\pm\tilde{\gamma}_2)_c-(\tilde{\gamma}_1\pm\tilde{\gamma}_2)_s]\\ &(\langle m_1,l_1|\delta(\rho-R_c)|m_2-1,l_2\rangle\\ &-\langle m_1,l_1|\delta(\rho-R_c)|m_2+1,l_2\rangle)\\ &-m_2\langle m_1,l_1|(\frac{1}{2l_B^2})(\tilde{\gamma}_1\pm\tilde{\gamma}_2)|m_2,l_2\rangle_{c/s}\\ &+\langle m_1,l_1|(\frac{\rho}{2l_B^2})^2(\tilde{\gamma}_1\pm\tilde{\gamma}_2)|m_2,l_2\rangle_{c/s}\\ &+k_z^2\langle m_1,l_1|(\tilde{\gamma}_1\pm\tilde{\gamma}_2)|m_2,l_2\rangle_{c/s}\}. \end{aligned}\tag{C.7}$$

Off-diagonal matrix elements:

$$
\begin{aligned}
\textbf{(1)}\ \langle m_1,l_1|C|m_2,l_2\rangle =& \frac{-\hbar^2}{2m_0}\{\sqrt{3}\{[\langle m_1,l_1|\bar{\gamma}|m_2-2,l_2\rangle \\
&+\langle m_1,l_1|\mu|m_2+2,l_2\rangle]_{c/s} \\
&+\{\langle m_1,l_1|\delta(\rho-R_c)(\bar{\gamma}_c-\bar{\gamma}_s)e^{-i\varphi}|m_2-1,l_2\rangle \\
&-\langle m_1,l_1|\delta(\rho-R_c)(\mu_c-\mu_s)e^{i\varphi}|m_2+1,l_2\rangle\} \\
&+\{\langle m_1,l_1|\delta(\rho-R_c)(\frac{\rho}{2l_B^2})(\bar{\gamma}_c-\bar{\gamma}_s)e^{-2i\varphi}|m_2,l_2\rangle \\
&-\langle m_1,l_1|\delta(\rho-R_c)(\frac{\rho}{2l_B^2})(\mu_c-\mu_s)e^{2i\varphi}|m_2,l_2\rangle\} \\
&+(\frac{\alpha_{m_2l_2}}{R})\{\langle m_1,l_1|(\frac{\rho}{2l_B^2})\mu e^{2i\varphi}|m_2,l_2\rangle_{c/s} \\
&-\langle m_1,l_1|(\frac{\rho}{2l_B^2})\bar{\gamma}e^{-2i\varphi}|m_2,l_2\rangle_{c/s}\} \\
&+m_2\{\langle m_1,l_1|(\frac{1}{2l_B^2})\mu e^{2i\varphi}|m_2,l_2\rangle_{c/s} \\
&+\langle m_1,l_1|(\frac{1}{2l_B^2})\bar{\gamma}e^{-2i\varphi}|m_2,l_2\rangle_{c/s}\} \\
&-\{\langle m_1,l_1|(\frac{\rho}{2l_B^2})^2\mu e^{2i\varphi}|m_2,l_2\rangle_{c/s} \\
&-\langle m_1,l_1|(\frac{\rho}{2l_B^2})^2\bar{\gamma}e^{-2i\varphi}|m_2,l_2\rangle_{c/s}\}\}\}. \qquad \text{(C.8)}
\end{aligned}
$$

$$
\begin{aligned}
\textbf{(2)}\ \langle m_1,l_1|B|m_2,l_2\rangle =& \frac{\hbar^2}{2m_0}\{\sqrt{3}[\langle m_1,l_1|\hat{k_-^0}\tilde{\gamma}_3k_z|m_2,l_2\rangle \\
&+\langle m_1,l_1|k_z\tilde{\gamma}_3\hat{k_-^0}|m_2,l_2\rangle]_{c/s} \\
&-2i\sqrt{3}\langle m_1,l_1|(\frac{\rho}{2l_B^2})\tilde{\gamma}_3k_ze^{-i\varphi}|m_2,l_2\rangle_{c/s}\}. \qquad \text{(C.9)}
\end{aligned}
$$

$$
\begin{aligned}
\textbf{(3)}\ \langle m_1,l_1|P^{\pm}|m_2,l_2\rangle =& [(\pm i)P(\frac{\alpha_{m_2l_2}}{R})\langle m_1,l_1|e^{\pm i\varphi}|m_2\pm1,l_2\rangle \\
&+(\pm i)P\langle m_1,l_1|e^{\pm i\varphi}(\frac{\rho}{2l_B^2})|m_2,l_2\rangle]_{c/s}. \qquad \text{(C.10)}
\end{aligned}
$$

$$
\textbf{(4)}\ \langle m_1,l_1|P^z|m_2,l_2\rangle =[P\langle m_1,l_1|k_z|m_2,l_2\rangle]_{c/s}. \qquad \text{(C.11)}
$$

where $\bar{\gamma}=(\tilde{\gamma}_3+\tilde{\gamma}_2)/2$, $\mu=(\tilde{\gamma}_2-\tilde{\gamma}_3)/2$ and $\frac{m_e^*}{m_0}=\frac{m_e}{m_0}+\frac{E_P(E_g+2\Delta/3)}{E_g(E_g+\Delta)}$. Here $\tilde{\gamma}_i$'s are Luttinger-like parameters, E_P is the Kane energy with P being the Kane parameter and $l_B=(\frac{\hbar}{eB_z})^{\frac{1}{2}}$ is the magnetic length.

Bibliography

[1] D. Li, T. Wu, P. Kim, L. Shi, P. Yang and A. Majumdar, Appl. Phys. Lett. **83**, 2934 (2003).

[2] Z. Wang and N. Mingo, Appl. Phys. Lett. **97**, 101903 (2010).

[3] L. C. L. Y. Voon, Y. Zhang, B. Lassen, M. Willatzen, Q. Xiong and P. C. Eklund, J. Nanosci. Nanotechnol. **8**, 1 (2008).

[4] R. Rurali, Rev. Mod. Phys. **82**, 427 (2010).

[5] C. Soci, A. Zhang, X.-Y. Bao, H. Kim, Y. Lo and D. Wang, J. Nanosci. Nanotechnol. **10**, 1 (2010).

[6] H. J. Fan, P. Werner and M. Zacharias, Small **2**, 700 (2006).

[7] K. Hiruma, K. Tomioka, P. Mohan, L. Yang, J. Noborisaka, B. Hua, A. Hayashida, S. Fujisawa, S. Hara, J. Motohisa and T. Fukui, Journal of Nanotechnology **2012**, 1 (2012).

[8] O. Hayden, R. Agarwal and W. Lu, Nanotoday **3**, 12 (2008).

[9] E. C. Garnett, M. L. Brongersma, Y. Cui and M. D. McGehee, Annu. Rev. Mater. Res. **41**, 269 (2011).

[10] W. Lu and C. M. Lieber, J. Phys. D: Appl. Phys. **39**, 387 (2006).

[11] C. Thelander, P. Agarwal, S. Brongersma, J. Eymery, L. F. Feiner, A. Forchel, M. Scheffler, W. Riess, B. J. Ohlsson, U. Gosele and L. Samuelson, Materialstoday **9**, 28 (2006).

[12] N. F. Zabah, K. S. K. Kwa, L. Bowen, B. Mendis and A. ONeill, J. Appl. Phys. **112**, 024309 (2012).

[13] T. Bhuvana and G. U. Kulkarni, ACS Nano **2**, 457 (2008).

[14] E. S. Park, D. Jang, J. Lee, Y. J. Kim, J. Na, H. Ji, J. W. Choi and G. T. Kim, Rev. Sci. Instrum. **80**, 126101 (2009).

[15] S. Hu, A. Hamidi, S. Altmeyer, T. Kster, B. Spangenberg and H. Kurz, J. Vac. Sci. Technol. B **16**, 2822 (1998).

[16] J. E. Bjorkholm, J. Bokor, L. Eichner, R. R. Freeman, J. Gregus, T. E. Jewell, W. M. Mansfield, A. A. MacDowell, E. L. Raab, W. T. Silfvast, L. H. Szeto, D. M. Tennant, W. K. Waskiewicz, D. L. White, D. L. Windt and O. R. Woodll, J. Vac. Sci. Technol. B **8**, 1509 (1990).

[17] Y. Sun, R. A. Graff, M. S. Strano and J. A. Rogers, small **1**, 1052 (2005).

[18] D. J. Frank, R. H. Dennard, E. Nowak, P. M. Solomon, Y. Taur and H.-S. P. Wong, Proc. IEEE **89**, 259 (2001).

[19] M. De Vittorio , M. T. Todaro, T. Stomeo, R. Cingolani, D. Cojoc and E. Di Fabrizio, Microelectron. Eng. **73**, 388 (2004).

[20] Y. C. Kong, D. P. Yu, B. Zhang, W. Fang and S. Q. Feng, Appl. Phys. Lett. **78**, 407 (2001).

[21] A. Colli, A. Fasoli, P. Beecher, P. Servati, S. Pisana, Y. Fu, A. J. Flewitt, W. I. Milne, J. Robertson, C. Ducati, S. De Franceschi, S. Hofmann and A. C. Ferrari, J. Appl. Phys. **102**, 034302 (2007).

[22] S. K. Lim , M. J. Tambe , M. M. Brewster and S. Gradecak, Nano Lett. **8**, 1386 (2008).

[23] R. Wagner and W. Ellis, Appl. Phys. Lett. **4**, 89 (1964).

[24] Z. H. Wu, X. Y. Mei, D. Kim, M. Blumin and H. E. Ruda, Appl. Phys. Lett. **81**, 5177 (2002).

[25] H. Ibach and H. Lueth. Solid-State Physics (Springer Verlag), 2003.

[26] J. Westwater, D. P. Gosain, S. Tomiya, S. Usui and H. Ruda, J. Vac. Sci. Technol. B **15**, 554 (1997).

[27] J. Hu, M. Ouyang, P. Yang and C. M. Lieber, Nature (London) **399**, 48 (1999).

[28] A. M. Morales and C. M. Lieber, Science **279**, 208 (1998).

[29] H. Y. Li, O. Wunnicke, M. T. Borgstrom, W. G. G. Immink, M. H. M. van Weert, M. A. Verheijen and E. P. A. M. Bakkers, Nano Lett. **7**, 1144 (2007).

[30] K. Haraguchi, T. Katsuyama, K. Hiruma and K. Ogawa, Appl. Phys. Lett. **60**, 745 (1992).

[31] X. Duan, J. Wang and C. M. Lieber, Appl. Phys. Lett. **76**, 1116 (2000).

[32] A. Shabaev and A. L. Efros, Nano Lett. **4**, 1821 (2004).

[33] L. J. Lauhon, M. S. Gudiksen, D. Wang and C. M. Lieber, Nature (London) **420**, 57 (2002).

[34] D. Lucot, F. Jabeen, J.-C. Harmand, G. Patriarche, R. Giraud, G. Faini and D. Mailly, Appl. Phys. Lett. **98**, 142114 (2011).

[35] Y. N. Guo, J. Zou, M. Paladugu, H. Wang, Q. Gao, H. H. Tan and C. Jagadish, Appl. Phys. Lett. **89**, 231917 (2006).

[36] M. S. Dresselhaus, Y. M. Lin, O. Rabin, M. R. Black and G. Dresselhaus, Springer handbook of nanotechnology 2nd ed. **113-153**, (2004).

[37] M. J. Tambe, L. F. Allard and S Gradecak, Journal of Physics: Conference Series **209**, 012033 (2010).

[38] M. E. Pistol and C. E. Pryor, Phys Rev B **78**, 115319 (2008).

[39] A. Ivanov and H. Haug, Phys Rev Lett. **71**, 3182 (1993).

[40] D. L. Dheeraj, G. Patriarche, H. Zhou, T. B. Hoang, A. F. Moses, S. Grnsberg, A. T. J. van Helvoort, B. O. Fimland and H. Weman, Nano Lett. **8**, 4459 (2008).

[41] M. Zheng, L. Zhang and G. H. Li, Chem. Phys. Lett. **363**, 128 (2002).

[42] D. M. Lyons, K. M. Ryan, M. A. Morris and J. D. Holmes, Nano. Lett. **2**, 811 (2002).

[43] J. Wang, M. S. Gudiksen, X. Duan, Y. Cui and C. M. Lieber, Science **293**, 1455 (2001).

[44] G. Zhang, K. Tateno, H. Sanada, T. Tawara, H. Gotoh and H. Nakano, Appl. Phys. Lett. **95**, 123104 (2009).

[45] S. Blom, L. Y. Gorelik, M. Jonson, R. I. Shekhter, A. G. Scherbakov, E. N. Bogachek and U. Landman, Phys. Rev. B **58**, 16305 (1998).

[46] J. C. Johnson, H. Yan, R. D. Schaller, P. B. Petersen, P. Yang and R. J. Saykally, Nano Lett. **2**, 279 (2002).

[47] M. S. Gudiksen, L. J. Lauhon, J. Wang, D. Smith and C. M. Lieber, Nature (London) **415**, 617 (2002).

[48] M. F. Crommie, C. P. Lutz and D. M. Eigler, Science **262**, 218 (1993).

[49] K. Storm, G. Nylund, L. Samuelson and A. P. Micolich, Nano Lett. **12**, 1 (2012).

[50] C. P. T. Svensson, T. Martensson, J. Tragardh, C. Larsson, M. Rask, D. Hessman, L. Samuelson and J. Ohlsson, Nanotechnology **19**, 305201 (2008).

[51] X. Duan, Y. Huang, Y. Cui, J. Wang and C. M. Lieber, Nature (London) **409**, 66 (2001).

[52] M. H. Huang, S. Mao, H. Feick, H. H. Yan, Y. Wu, H. Kind, E. Weber, R. Russo and P. Yang, Science, **292** 1897 (2001).

[53] J. C. Johnson, H. J. Choi, K. P. Knutsen, R. D. Schaller, P. Yang and R. J. Saykally Nature Mat. **1**, 106 (2002).

[54] B. Hua, J. Motohisa, Y. Kobayashi, S. Hara and T. Fukui, Nano Lett. **9** 112 (2009).

[55] E. M. Gallo, G. Chen, M. Currie, T. McGuckin, P. Prete, N. Lovergine, B. Nabet and J. E. Spanier, Appl. Phys. Lett. **98**, 241113 (2011).

[56] O. L. Muskens, J. G. Rivas, R. E. Algra, E. P. A. M. Bakkers and Ad. Lagendijk, Nano Lett. **8**, 2638 (2008).

[57] L. Cao, J. S. White, J.-S. Park, J. A. Schuller, B. M. Clemens and M. L. Brongersma, Nat. Mater. **8**, 643 (2009).

[58] E. Garnett and P. Yang, Nano Lett. **10**, 1082 (2010).

[59] A. Gu, Y. Huo, S. Hu, T. Sarmiento, E. Pickett, D. Liang, S. Li, A. Lin, S. Thombare, Z. Yu, S. Fan, P. Mclntyre, Y. Cui and J. Harris, 35th IEEE Photovoltaics Specialists Conf., 2010 002034 (2010).

[60] B. M. Kayes, H. A. Atwater and N. S. Lewis, J. Appl. Phys. **97**, 114302 (2005).

[61] K. Tomioka, J. Motohisa, S. Hara, K. Hiruma and T. Fukui, Nano Lett. **10**, 1639 (2010).

[62] L. C. Chuang, F. G. Sedgwick, R. Chen, W. S. Ko, M. Moewe, K. W. Ng, T.-T. D. Tran and C. Chang-Hasnain, Nano Lett. **11**, 385 (2011).

[63] C. Colombo, M. Hei, M. Grtzel and A. Fontcuberta i Morral, Appl. Phys. Lett. **94**, 173108 (2009).

[64] J. A. Czaban, D. A. Thompson and R. R. LaPierre, Nano Lett. **9**, 148 (2009).

[65] G. Mariani, P.-S. Wong, A. M. Katzenmeyer, F. Leonard, J. Shapiro and D. L. Huffaker, Nano Lett. **11**, 2490 (2011).

[66] C. Gutsche, A. Lysov, D. Braam, I. Regolin, G. Keller, Z.-A Li, M. Geller, M. Spasova, W. Prost, and F.-J. Tegude Adv. Funct. Mater. **22**, 929 (2012).

[67] A. O. Niskanen, A. Colli, R. White, H. W. Li, E. Spigone and J. M. Kivioja, Nanotechnology **22**, 295502 (2011).

[68] Y. Cui, Q. Wei, H. Park and C. M. Lieber, Science **293**, 1289 (2001).

[69] H. Peelaers, B. Partoens and F. M. Peeters, Phys. Rev. B **82**, 113411 (2010).

[70] Y. Arakawa, T. Yamauchi and J. N. Schulman, Phys. Rev. B **43**, 4732 (1991).

[71] G. D. Sanders and Y. -C. Chang, Phys. Rev. B **45**, 9202 (1992).

[72] H. Yorikawa, H. Uchida and S. Muramatsu, J. Appl. Phys. **79**, 3619 (1996).

[73] M. P. Persson and H. Q. Xu, Appl. Phys. Lett. **81**, 1309 (2002).

[74] M. P. Persson and H. Q. Xu, Nano Lett. **4**, 2409 (2004).

[75] Y. Zheng, C. Rivas, R. Lake, K. Alam, T. Boykin and G. Klimeck, IEEE Trans. Electron Devices **52**, 1097 (2005).

[76] X. Guan and Z. Yu, IEEE Conference on Electron Devices and Solid-State Circuits, IEEE, 19 (2005).

[77] C. Harris and E. P. OReilly, Physica E **32**, 341 (2006).

[78] J. M. Luttinger and W. Kohn, Phys. Rev. **97**, 869 (1955).

[79] J. M. Luttinger, Phys. Rev. **102**, 1030 (1956).

[80] M. Cardona and F. H. Pollak, Phys. Rev. **142**, 530 (1966).

[81] W.-Ho Seo and J. F. Donegan, Phys. Rev. B **68**, 075318 (2003).

[82] T. Dietl, H. Ohno and F. Matsukura, Phys. Rev. B **63**, 195205 (2001).

[83] G. E. Pikus and G. L. Bir, Fiz. tverd. Tela (Leningrad) **1**, 1642 (1959) [Sov. Phys. Solid State, **1**, 1502 (1960)].

[84] G. L. Bir and G. E. Pikus, Symmetry and Strain-Induced Effects in Semiconductors (Wiley, New York, 1974).

[85] S. Ben Radhia, K. Boujdaria, S. Ridene, H. Bouchriha and G. Fishman. *J. Appl. Phys.* **94**, 5726 (2001).

[86] I. Saidi, S. B. Radhia and K. Boujdaria, J. Appl. Phys. **107**, 043701 (2010).

[87] M. Tchernycheva, C. Sartel, G. Cirlin, L Travers, G. Patriarche, J. C. Harmand, L. S. Dang, J. Renard, B. Gayral, L. Nevou and F. Julien, Nanotechnology **18**, 385306 (2007).

[88] C. R. Pidgeon and R. N. Brown, Phys. Rev. **100**, 575 (1966).

[89] T. B. Bahder, Phys. Rev. B **41**, 11992 (1990).

[90] C. Pryor, Phys. Rev. B **57** 7190 (1998).

[91] S. L. Chuang and C. C. Chang, Phys. Rev. B **54**, 2491 (1996).

[92] G. Fishman, Phys. Rev. B **52**, 11132 (1995).

[93] J. B. Xia, Phys. Rev. B **43**, 9856 (1991).

[94] K. Boujdaria, S. Ridene and G. Fishman, Phys. Rev. B **63**, 235302 (2001).

[95] G. Bastard, Wave Mechanics Applied to Semiconductor Heterostructures (Les Editions de Physique, Les Ulis, 1988).

[96] R. Winkler, Spin-Orbit Coupling Effects in Two-Dimensional Electron and Hole Systems, (Springer-Verlag Berlin Heidelberg, 2003), p.207.

[97] M. G. Burt, J. Phys.: Condens. Matter **4**, 6651 (1992).

[98] B. A. Foreman, Phys. Rev. B **48**, 4964 (1993).

[99] B. A. Foreman, Phys. Rev. B **49**, 1757 (1994).

[100] U. Ekenberg, Phys. Rev. B **40**, 7714 (1989).

[101] M. J. Godfrey and A. M. Malik, Phys. Rev. B **53**, 16504 (1995).

[102] G. T. Einevoll and L. J. Sham, Phys. Rev. B **49**, 10533 (1993).

[103] R. Eppenga, M. F. H. Schuurmans and S. Colak, Phys. Rev. B **36**, 1554 (1987).

[104] B. Laikhtman, ISSP **46**, 4769 (1992).

[105] S. R. White and L. J. Sham, Phys. Rev. B **47**, 879 (1981).

[106] R. A. Morrow and K. R. Brownstein, Phys. Rev. B **30**, 678 (1984).

[107] R. A. Morrow, Phys. Rev. B **35**, 8074 (1987).

[108] G. Paasch, P. H. Nguyen and G. Gobsch, Phys. Status. Solidi B **167**, 581 (1990).

[109] S. Nojima, Jpn. J. Appl. Phys. **31**, 1401 (1992).

[110] W. Pötz, W. Porod and D. K. Ferry, Phys. Rev. B **32**, 3868 (1985).

[111] H. Kosaka, A. A. Kislev, F. A. Baron, K. W. Kim and E. Yablonovitch, Electron. Lett. **37**, 464 (2001).

[112] A. Copple, N. Ralston and X. Peng, Appl. Phys. Lett. **100**, 193108 (2012).

[113] G. Dresselhaus, A. F. Kip and C. Kittel, Phys. Rev. **98**, 368 (1955).

[114] G. Dresselhaus, Phys. Rev. **100**, 580 (1955).

[115] A. Baldereschi and N. O. Lipari, Phys. Rev. B **8**, 2697 (1973).

[116] I. Vurgaftman, J. R. Meyer and L. R. Ram Mohan, J. Appl. Phys. **89**, 5815 (2001).

[117] W. Yi, V. Narayanamurti, H. Lu, M. A. Scarpulla, A. C. Gossard, Y. Huang, J.-H. Ryou and R. D. Dupuis, Appl. Lett. **95**, 112102 (2009).

[118] P. Y. Yu and M. Cardona, Fundamentals of Semiconductors, 3rd ed. (Springer, New York, 2003), p. 260.

[119] P. Redliński and F. M. Peeters, Phys. Rev. B **77**, 075329 (2008).

[120] V. V. Ravi Kishore, B. Partoens and F. M. Peeters, Phys. Rev. B **82**, 235425 (2010).

[121] A. Kimura, M. Nido and A. Suzuki, Photonics Technology Lett. **6**, 1101 (1994).

[122] P. Lawaetz, Phys. Rev. B **4**, 3460 (1971).

[123] K. A. Kaduki and W. Batty, Physica Scripta. **61**, 213 (2000).

[124] A. Hoffmann, H. Siegle, L. Eckey, B. Lummer, Thurian, R. Heitz, B. K. Meyer, C. Wetzel, D. Hoffmann, V. Harle, F. Schulz and A. Kohl, Superlattices Microstruct. **15** 303 (1994).

[125] M. Inoue, K. Yoh, and A. Nishida, Semicond. Sci. Technol. **9**, 966 (1994).

[126] J. B. Boos, B. R. Bennett, N. A. Papanicolaou, M. G. Ancona, J. G. Champlain, R. Bass and B. V. Shanabrook, Electron. Lett. **43**, 834 (2007).

[127] W. Xu, X. F. Wei and J. Zhang, Appl. Phys. Lett. **92**, 162108 (2008).

[128] R. Ascazubi, I. Wilke, K. J. Kim and P. Dutta, Phys. Rev. B **74**, 075323 (2006).

[129] A. J. L. Poulter, M. Lakrimi, R. J. Nicholas, N. J. Mason and P. J. Walker, Phys. Rev. B **59**, 10785 (1999).

[130] H. Ohno, L. Esaki, and E. E. Mendez, Appl. Phys. Lett. **60**, 3153 (1992).

[131] H. Mohseni, E. Michel, J. Sandoen, M. Razeghi, W. Mitchel and G. Brown, Appl. Phys. Lett. **71**, 1403 (1997).

[132] G. Liu and S. L. Chuang, Phys. Rev. B **65**, 165220 (2002).

[133] G. A. Sai-Halasz, L. Esaki and W. A. Harrison Phys. Rev. B **18**, 2812 (1978).

[134] M. Altarelli, Phys. Rev. B **28**, 842 (1983).

[135] Y. C. Chang and J. N. Schulman, Phys. Rev. B **31**, 2069 (1985).

[136] T. Andlauer and P. Vogl, Phys. Rev. B **80**, 035304 (2009).

[137] F. Wang, Y. Jia, S. F. Li and Q. Sun, J. Appl. Phys. **105**, 043101 (2009).

[138] S. B. Rejeb, M. Debbichi, M. Sai, A. Gassenq, E. Tournie and P. Christol, J. Phys. D: Appl. Phys. **43**, 325102 (2010).

[139] B. Montanari, M. Peressi, S. Baroni and E. Molinari, Appl. Phys. Lett. **69**, 3218 (1996).

[140] H. Kroemer, Physica E **20**, 196 (2004).

[141] H. Mohseni, M. Razeghi, G. J. Brown and Y. S. Park, Appl. Phys. Lett. **78**, 2107 (2001).

[142] A. Gin, Y. Wei, A. Hood, A. Bajowala, V. Yazdanpanah, M. Razeghi and Tidrow,Appl. Phys. Lett. **84**, 2037 (2004).

[143] Y. Wei, A. Hood, A. Bajowala, V. Yazdanpanah, M. Razeghi, Tidrow and V. Nathan, Appl. Phys. Lett. **86**, 091109 (2005).

[144] S. Mallick, K. Banerjee, S. Ghosh, E. Plis, J. B. Rodriguez, S. Krishna and C. Grein, Appl. Phys. Lett. **91**, 241111 (2007).

[145] A. Zakharova, S. T. Yen and K. A. Chao, Phy. Rev. B **64**, 235332 (2001).

[146] E. Halvorsen, Y. Galperin and K. A. Chao, Phy. Rev. B **61**, 16743 (2000).

[147] A. Zakharova, I. Lapushkin, K. Nilsson, S. T. Yen and K. A. Chao, Phy. Rev. B **73**, 125337 (2006).

[148] A. Zakharova, S. T. Yen and K. A. Chao, Phy. Rev. B **69**, 115319 (2004).

[149] K. Nilsson, A. Zakharova, I. Lapushkin, S. T. Yen and K. A. Chao, Phy. Rev. B **74**, 075308 (2006).

[150] M. J. Yang, C. H. Yang, B. R. Bennett and B. V. Shanabrook, Phys. Rev. Lett. **78**, 4613 (1997).

[151] M. Lakrimi, S. Khym, R. J. Nicholas, D. M. Symons, F. M. Peeters, N. J. Mason and P. J. Walker, Phys. Rev. Lett. **79**, 3034 (1997).

[152] B. M. Borg, K. A. Dick, B. Ganjipour, M. E. Pistol, L. E. Wernersson, C. Thelander and L. Esaki, Nano Lett. **10**, 4080 (2010).

[153] M. Ek, B. M. Borg, A. W. Dey, B. Ganjipour, C. Thelander, L. E. Wernersson and K. A. Dick, Cryst. Growth Des. **11**, 4588 (2011).

[154] B. Ganjipour, A. W. Dey, B. M. Borg, M. Ek, M. E. Pistol, K. A. Dick, L. E. Wernersson and C. Thelander, Nano Lett. **11**, 4222 (2011).

[155] B. Ganjipour, M. Ek, B. M. Borg, K. A. Dick, M. E. Pistol, L. E. Wernersson and C. Thelander, Appl. Phys. Lett. **101**, 103501 (2012).

[156] V. V. Ravi Kishore, N Čukarić, B. Partoens, M Tadić and F. M. Peeters, J. Phys.: Condens. Matter **24**, 135302 (2012).

[157] A. J. Ekpunobi, Mat. Sci. Sem. Proc. **8**, 463 (2005).

[158] A. Sai-Halasz, L L. Chang, J. -M. Welter, C. -A. Chang and L. Esaki, Solid State Commun. **27**, 935 (1978).

[159] L. M. Claessen, J. C. Maan, M. Altarelli, P. Wyder, L. L. Chang and L. Esaki, Phys. Rev. Lett. **57**, 2556 (1986).

[160] L. L. Chang and L. Esaki, Surf. Sci. **98**, 70 (1980).

[161] B. A. Bernevig, T. L. Hughes and S. C. Zhang, Science **314**, 1757 (2006).

[162] M. Konig, S. Wiedmann, C. Brune, A. Roth, H. Buhmann, L. W. Molenkamp, X. L. Qi and S. C. Zhang, Science **318**, 766 (2007).

[163] C. Liu, T. L. Hughes, X. L. Qi, K. Wang and S. C. Zhang, Phy. Rev. Lett. **100**, 236601 (2008).

[164] I. Knez, R. R. Du and G. Sullivan, Phy. Rev. B **81**, 201301 (2010).

[165] C. Schuller, Physica E **3**, 121 (1998).

[166] T. Chakraborty, Quantum Dots: A Survey of the Properties of Artificial Atoms (North-Holland, Amsterdam, 1999).

[167] T. Chakraborty and P. Pietilinen Phys. Rev. B **50**, 8460 (1994).

Curriculum Vitae

Name:	Vepakomma Venkata Ravi Kishore
Born:	24/10/1982, Nellore, INDIA
Contact:	U 206, Groenenborgerlaan 171
	2020, Antwerp, BELGIUM
Email:	ravi.vepakomma@ua.ac.be

Education

2009-2012:	**PhD** University Of Antwerp, BELGIUM
2008-2009:	**Pre-Doc** University Of Antwerp, BELGIUM
2006-2008:	**MSc** Indian Institute of Technology Madras, INDIA
2001-2004:	**BSc** Osmania University, INDIA

List of publications

- V. V. Ravi Kishore, B. Partoens, and F. M. Peeters: Electronic structure and optical absorption of GaAs/$Al_xGa_{1-x}As$ and $A_xGa_{1-x}As$/GaAs core-shell nanowires, Phys. Rev. B 82, 235425 (2010). Also selected for the December 20, 2010 issue of Virtual Journal of Nanoscale Science and Technology.

- V. V. Ravi Kishore, N. Cukaric, B. Partoens, M. Tadic and F. M. Peeters: Hole subbands in freestanding nanowires: 6-band versus 8-band k.p modelling, J. Phys.: Condens. Matter 24, 135302 (2012).

- V. V. Ravi Kishore, B. Partoens, and F. M. Peeters : Electronic structure of InAs/GaSb core-shell nanowires, Phys. Rev. B 86, 165439 (2012).

Computer Skills

Operating systems:	Windows, Linux
Office:	Word, Excel, PowerPoint
Programming languages:	C/C++, Fortran, Java, bash scripting
Mathematical software:	Mathematica, MATLAB with prarallel computing, Maple
Plotting Software:	Gnuplot, Origin, CorelDraw

Managerial Skills

2006-2007:	Served as Councilor for the first year masters students of mathematics, physics and chemistry departments at the Indian Institute of Technology Madras, INDIA
2006-2007:	Served as Class Representative for my masters class at the Indian Institute of Technology Madras, INDIA

Language Proficiency

Telugu (Native), Hindi (Fluent), English (Fluent)